DISCOVERY OF NEW REGULATORY PROTEINS AND MECHANISMS IN MUSCLE BIOLOGY AND DISEASE

APPROVED BY SUPERVISORY COMMITTEE

Joseph A. Hill, M.D., Ph.D.

Raymond J. MacDonald, Ph.D.

Eric N. Olson, Ph.D.

James T. Stull, Ph.D.

Dedicated to my parents for tolerating my constantly expanding education and my avoidance of getting a real job. I could not have done it without their support.

ACKNOWLEDGMENTS

I would like to thank my mentor, Dr. Eric Olson, for taking a chance on me despite my meager molecular biology training. I hope that I have returned his investment several fold. Without Eric's constant vigilance, my project would never have reached a satisfactory conclusion.

I would also like to thank my dissertation committee, Drs. James Stull, Joseph Hill, and Raymond MacDonald for their support and guidance over the past several years. Their insights were vital to understanding my project from different perspectives that helped me to pursue more meaningful directions

I am especially thankful for the help from Dr. Rhonda Bassel-Duby. I had much to learn for my development into a professional scientist, but Rhonda greatly catalyzed this process. Not only did Rhonda tirelessly help me with scientific writing and analysis and establishing incredibly fruitful collaborations, she was a source of constant enthusiasm.

I would also like to thank my post-doctoral mentor, Jason O' Rourke. Despite our vast differences in personality and thinking, Jason was dedicated to my initial training and generously gave me the *Klhl40* gene to study that proved to be of great importance.

In addition, I would also like to extend my gratitude towards John McAnally and Xiaoxia Qi who showed extreme dedication their works and helped me to generate many new lines of mice. Without their efforts, I, nor our lab, would be where it is today.

I would also like to thank Svetlanna Bezprozvannaya for her assistance with performing an immensely comprehensive protein binding screen for Klhl40. Svetlanna's findings were key toward establishing a completely novel mechanism for our proteins of interest, and we could not have accomplished this work on our own.

In addition, I am very grateful for the efforts of Cheryl Nolen, Evelyn and Dylan Tennison, Lillian Sutherland, and Alex Mireault for their technical assistance and in keeping our lab running very smoothly. Also, I would like to thank Jennifer Brown for her generous assistance with administrative tasks as well as for organizing social events that were the envy of every other lab on campus.

I would like to also thank the remainder of the Olson lab for providing me with a home for the past four years. It was wonderful working with such a dedicated and social group of scientists. Their warm attitudes helped to mitigate some of the hardships that we all inevitably encounter in science.

To my collaborators, I offer my sincerest gratitude for elevating our studies to new levels and making connections that were impossible to understand with our resources.

Finally, I would like to thank my parents and brother for their unconditional support and love. They shared in all my joys, but their greatest contribution was lifting me from crushing failures and disappointments. It has been a long journey that is almost to its conclusion, but I would not have proceeded even a step in to this adventure without the help of my family.

DISCOVERY OF NEW REGULATORY PROTEINS AND MECHANISMS IN MUSCLE BIOLOGY AND DISEASE

by

Ankit Garg

DISSERTATION

Presented to the Faculty of the Graduate School of Biomedical Sciences

The University of Texas Southwestern Medical Center at Dallas

In Partial Fulfillment of the Requirements

For the Degree of

DOCTOR OF PHILOSOPHY

The University of Texas Southwestern Medical Center at Dallas

Dallas, Texas

May, 2016

DISCOVERY OF NEW REGULATORY PROTEINS AND MECHANISMS IN MUSCLE BIOLOGY AND DISEASE

Ankit Garg

The University of Texas Southwestern Medical Center at Dallas, 2014

Supervising Professor: Eric N. Olson, PhD

In an effort to discover new regulators of muscle function, we identified a novel muscle-specific protein, Klhl40. Genetic deletion of Klhl40 in mice results in a nemaline myopathy-like phenotype with disruption of sarcomere function causing neonatal lethality. Nemaline myopathy (NM) typically results from sarcomere thin filament dysfunction, but the molecular function of Klhl40 is not known. We found that Klhl40 binds to two proteins: (1) nebulin (Neb), a sarcomere thin filament protein that is frequently mutated in NM; and (2) leiomodin 3 (Lmod3), a novel muscle-specific protein with putative thin filament actin polymerization activity. Klhl40 belongs to the BTB-BACK-Kelch (BBK) protein family, which typically promote protein ubiquitination and degradation, but we find that Klhl40 stabilizes its substrates. Thus, Neb and Lmod3 protein levels are diminished in Klhl40 deficient mice independent of any changes in their respective mRNA transcripts. Loss of KLHL40 in humans was recently reported to cause NM, and we find that NEB and LMOD3 are decreased in some KLHL40 mutant patients. However, the function of LMOD3 is also not known. To establish the role of LMOD3 in NM, we generated Lmod3 knockout mice by TALEN-mediated mutagenesis. Preliminary data shows that loss of Lmod3 results in a degenerative skeletal muscle myopathy. Thus, we propose that loss of Klhl40 directly results in decreased Neb and Lmod3 causing thin filament disruption and subsequent NM. In addition, we uncover the first BBK

protein with a pro-stability function which has broad implications for future study of this protein family.

In conjunction to our studies with Klh40, we found a closely neighboring gene in the antisense direction, *Hhatl*. Similar to *Klhl40*, we found that *Hhatl* expression is highly enriched in the heart and skeletal muscle although with notable expression in the central nervous system. *Hhatl* encodes for a putative membrane bound *O*-acyltransferase protein. Global deletion, but not heart or skeletal muscle-specific deletion, of *Hhatl* results in a failure to thrive phenotype with mid to late neonatal lethality. We outline future experiments to determine the nature and mechanism of the Hhatl knockout phenotype as well as possible means to delineate its function in striated muscles.

Table of Contents

Prior Publications

Ankit Garg, Jason O' Rourke, Chengzu Long, Svetlana Bezprozvannaya, Jonathan Doering, Nadine Beetz, Benjamin R. Nelson, Lin Li, She Chen, Nigel G. Laing, Robert W. Grange, Rhonda Bassel-Duby, and Eric N. Olson. 2014. KLHL40 deficiency destabilizes thin filament proteins and promotes nemaline myopathy. *J Clin Invest*, in press.

Traver Hart, Alice Zhao, **Ankit Garg**, Swetha Bolusani, and Edward M. Marcotte. 2009. Human cell chips: adapting DNA microarray spotting technology to cell-based imaging assays. *PLoS ONE 4*(10): e7088.

Scott Yockel, **Ankit Garg**, and Angela K. Wilson. 2005. The Existence of FKrCF3, FKrSiF3, and FKrGeF3: A Theoretical Study. *Chem. Phys. Lett.* 411, 91-97.

List of Figures

List of Abbreviations

aMHC – α-myosin heavy chain

ANP – atrial natriuretic peptide

BACK – BTB and c-terminal kelch

BBK – BTB BACK kelch

bMHC – β-myosin heavy chain

BNP – brain natriuretic peptide

BTB – broad-complex, tramtrack and bric á brac

CAPN3 – calpain 3

CDS – coding sequence

Co-IP – co-immunoprecipitation

Cullin 3 – Cul3

emPAI – exponentially modified protein abundance

F-actin – filamentous actin

G-actin – globular actin

Hhatl – hedgehog acyltransferase-like

Kbtbd – kelch-BTB domain

Klhl – kelch-like

KR – kelch repeat

Lmod – leiomodin

MBOAT – membrane bound *O*-acyltransferase

MCK – muscle creatine kinase

MRTF – myocardin-related transcription factor

Mybp – myosin binding protein

Neb – nebulin

PCR – polymerase chain reaction

Px – “x” day old mice

qPCR – quantitative PCR

SRF – serum response factor

TAP – tandem affinity purification

TALEN - transcription activator-like effector nuclease

TCAP – telethonin or titin cap protein

TTN –titin

Tmod – tropomodulin protein

Y2H – yeast two-hybrid

CHAPTER ONE

THE SARCOMERE AND MUSCLE DISEASE

Introduction

Muscle is comprised of cells that impart movement to surrounding structures allowing for locomotion. Central to this movement is the dynamic interaction between sliding actin and myosin filaments. The organization of these filaments stratifies muscle into two groups: smooth muscle and striated muscle. Smooth muscle lacks regular arrangement of actin and myosin filaments giving them a “smooth” appearance. Striated muscles, which include cardiac and skeletal muscles, contain actin/myosin filaments organized into tandem arrays that lend to a “striated” appearance. The fundamental unit of these arrays is the sarcomere which is present in all striated muscles. The sarcomere is vital to striated muscle contraction, and dysfunction of any one of its many components can result in a variety of myopathies (1). Understanding the complexities of the sarcomere is vital to innovating new therapies to treat the broad array of striated muscle diseases.

Overview of the sarcomere

Sarcomeres are arranged in tandem arrays such that the end of one sarcomere serves as the beginning of another sarcomere. The outer boundaries of a single sarcomere subunit are demarcated by a structure called the Z-line (or Z-disc) (Figure 1.1). The Z-line is composed mainly of α-actinin which serves as an anchor for other sarcomere proteins. Between two Z-lines, a single sarcomere can be broadly divided into an I-band, which is bisected by the Z-

line, and an A-band. These bands are so named based on their refractive properties. The I-band overlays the Z-line and as well as the thin filament which is largely composed of an actin polymer chain. Adjacent to the I-band is the A-band which contains mostly myosin and is referred to as the thick filament. Dynamic cross-linking of myosin to actin, in conjunction with conformational changes to myosin, generate the force underlying muscle contraction (1).

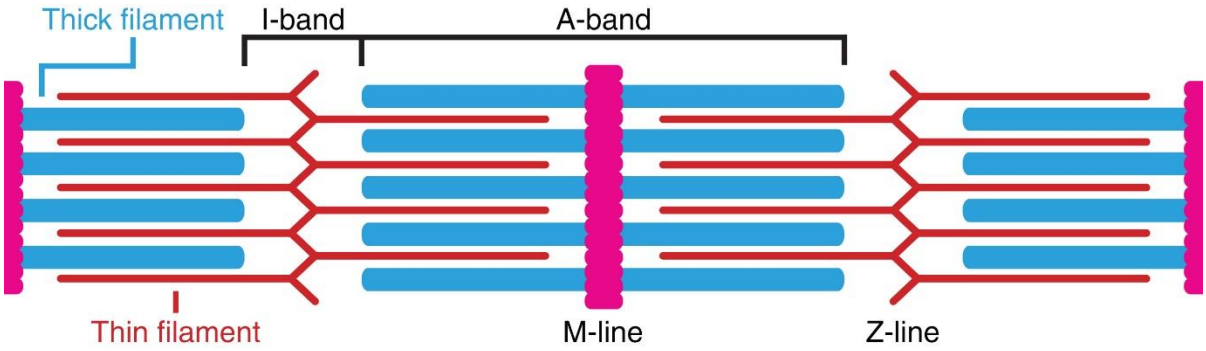

Figure 1.1. Striated muscle sarcomere. Schematic view of a sarcomere in striated muscles showing its basic components.

Muscle contraction and the sliding filament theory

With the advent of electron microscopy (EM) in the mid-20th century, muscle biologists were able to see a detailed view of the sarcomere for the first time. Much of what biologists gleaned about the individual sarcomere bands from light microscopy and x-ray diffraction held true at the EM level, but new insights were made into the molecular mechanisms of muscle contraction. Preceding electron microscopy, there were many theories on muscle contraction, but Hall, Jakus, and Schmitt brought the filament contraction theory to center stage with EM analysis of myofibers (2). As what was seen by using light microscopy, the authors observed that the sarcomere bands shortened during muscle contraction, but with the added power of EM, they saw that these fibers remained straight during contraction. These observations

refuted the belief that muscle fibers formed a spiraling pattern during contraction. Instead the authors suggested, though not uniquely, that the filaments themselves must shorten, but this idea was short lived in the face of the work of Huxley, *et. al.* and his sliding filament theory (3, 4).

Huxley and Hanson observed that during muscle contraction, the myosin containing A-band did not change length while the I-band shortened (3, 4). However, after removing myosin at different sarcomere lengths, leaving just the actin containing I-band, the authors observed that the I-band also does not change length. These observations directly refuted the filament contraction theory. From their work, Huxley and Hanson derived a more eloquent model of contraction: the sliding filament model (Figure 1.2). In this model, the authors proposed that during muscle contraction, actin thin filaments slide towards myosin thick filaments and the two proteins form cross-bridges in an ATP-dependent manner. Future studies built upon this model and described the generation of contractile force in more molecular detail by structural and biochemical characterization. The eloquent work of Huxley, *et. al.*, remains a testament to how carefully constructed experiments along with creative thinking can lead to scientific theories that surpass the resolution of technology and generate ideas that can stand the test of time (3, 4).

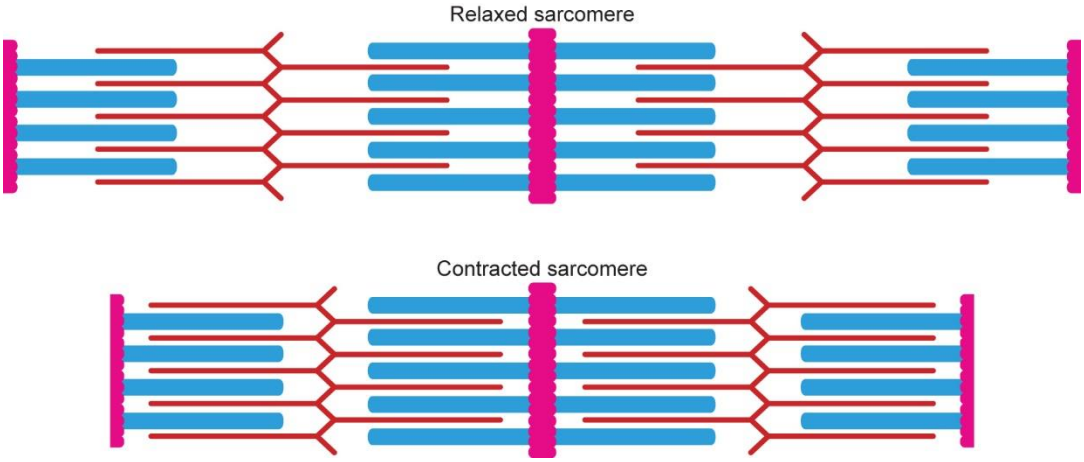

Figure 1.2. Sliding filament theory. Schematic representation of a sarcomere undergoing muscle contraction according to the sliding filament theory. Note that no filament changes in length and only the degree of overlap between the thin and thick filaments changes.

Molecular composition of the sarcomere and sarcomere centric myopathies

Beyond actin and myosin, there are a plethora of proteins that support the sarcomere and regulate muscle contraction (Figure 1.3).

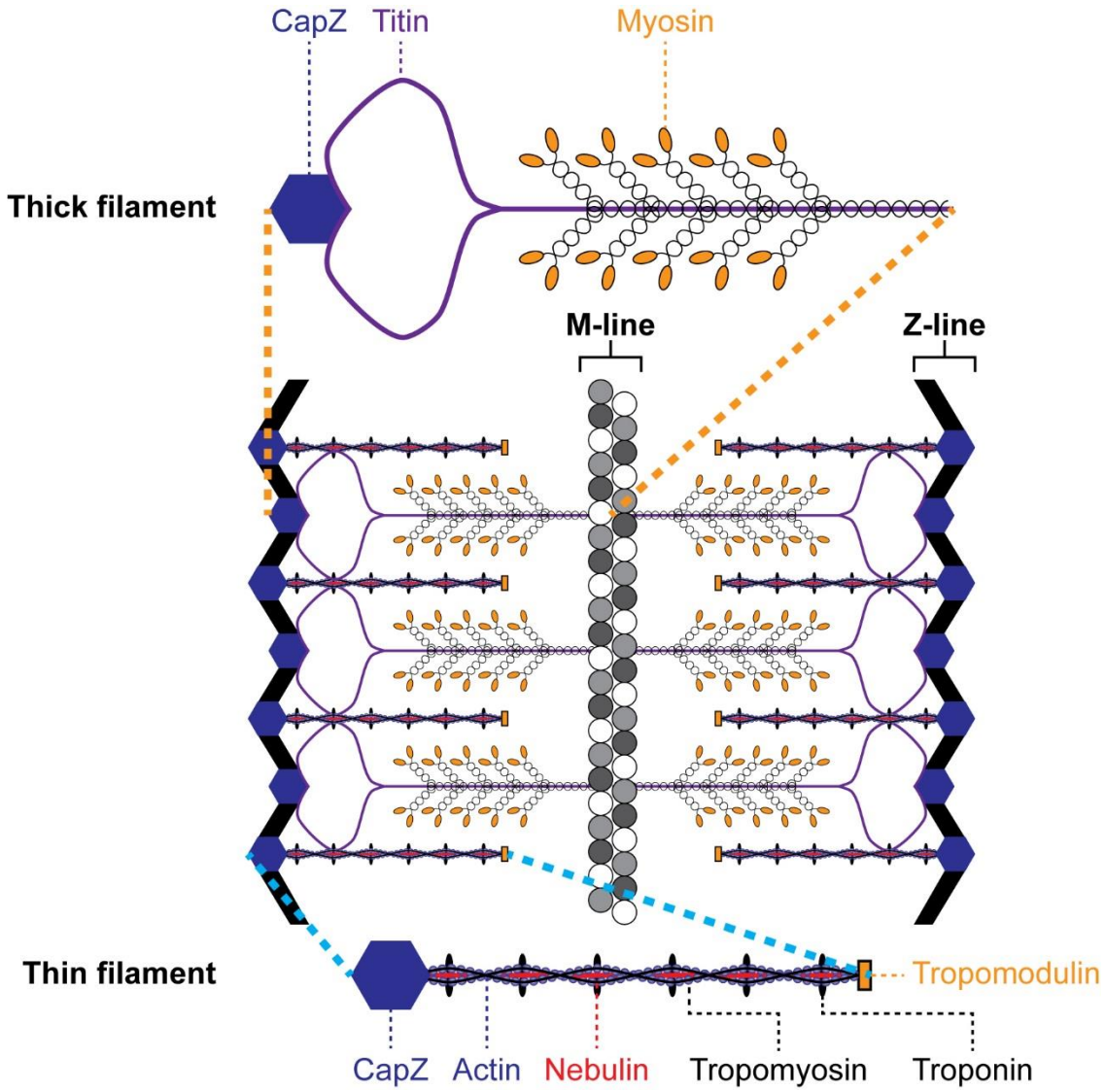

Figure 1.3. Molecular composition of the sarcomere. More detailed view of the molecules that make up the sarcomere. The thick and thin filaments are enlarged to delineate additional proteins.

The largest of these proteins is, aptly named, titin which is approximately 3MDa in size with a length of 1μm. To date, titin is the largest protein known in nature. Befitting its enormous length, each molecule of titin spans half a sarcomere with its N-terminus embedded in the Z-line and its C-terminus into the M-line. Titin is best known to maintain integrity of stretched

sarcomeres with its elastic properties and maintenance of thick filament length, but more recent data suggests that it plays a vital role in myofibrillogenesis (reviewed in (5)). *TTN*, the gene encoding the titin protein, undergoes alternative splicing lending to different isoforms that are more enriched in either cardiac or skeletal muscles. Accordingly, mutations in different regions of *TTN* lead to a variety of primary cardiomyopathies or skeletal muscle myopathies. Mutations in genes encoding other titin associated proteins, *CAPN3* (calpain 3) and *TCAP* (telethonin or titin cap protein), have also been shown to result in primary myopathies (6).

Towards the center of the sarcomere is the M-line which consists of its own unique proteins. The M-line serves as an anchor point for titin as well as forming connections to adjactent sarcomeres. However, no primary myopathies originating from M-line disruption have been reported so the M-line will not be discussed further (5).

Spanning from the M-line towards the Z-disc are the thick filaments. The most abundant protein in the thick filament is myosin, but also present are the myosin binding proteins Mybp-C, Mybp-H, and Mybp-X. Mutations in a variety of genes encoding proteins making up myosin as well as mutations in *MYBP-C*, the gene encoding for Mybp-c protein, have been shown to result in familial hypetrophic cardiomyopathy (reviewed in (5)).

Finally, the thin filament is made up of many accessory proteins that bind to actin and regulate actin-myosin cross-linking. Thin filament actin polymers are coated with the tropomyosin-troponin complex. Under conditions of low intracellular calcium, i.e. inactive muscle, the tropomyosin-troponin complex serves to sterically hinder actin-myosin interactions. Upon stimulation of muscle to contract, increased intracellular contraction releases the tropomyosin-troponin complex from actin allowing for it to interact with myosin and undergo muscle contraction. In addition to regulators of actin-myosin interaction, there are proteins that regulate the length of the thin filament. The CapZ and tropomodulin (Tmod)

proteins bind the barbed (fast growing) and pointed (slow growing) ends of the actin polymer, respectively. In addition, nebulin (Neb), a giant 800kDa protein spanning from the Z-line to the end of the thin filament, also serves a possible role in regulating the length of the thin filament (reviewed in (7)). Mutations in thin filament proteins cause a very particular disease referred to as nemaline myopathy. Not all mutations in thin filament proteins cause nemaline myopathy, but nearly all mutations causing nemaline myopathy localize to the thin filament.

The focus of this dissertation is how loss of a novel muscle protein, Klhl40, causes nemaline myopathy by destabilizing nebulin and another novel muscle protein, leiomodin 3 (Lmod3). I find that Lmod3 is the most down regulated protein in the proteome of Klhl40 deficient mice, and in another chapter, we show that deletion of Lmod3 alone is sufficient to cause a skeletal muscle myopathy. Finally, I close with a chapter on the genomic neighbor of *Klhl40*: *Hhatl*, which we originally pursued due to issues with our *Klhl40* knockout that resulted in a reduced expression of *Hhatl*. I find that *Hhatl* is also highly enriched in striated muscle tissues however, deletion of this gene from skeletal muscle or heart does not result in lethality whereas a global deletion of *Hhatl* results in a failure to thrive with death in the mid to late neonatal period of mice. I discuss possible directions for studying this interesting phenotype as well as future experiments to delineate whether Hhatl has any role in striated muscle biology.

CHAPTER TWO

LOSS OF KLHL40 DESTABILIZES NEBULIN AND LMOD3 CAUSING NEMALINE MYOPATHY

INTRODUCTION

Congenital skeletal muscle dysfunction leading to infantile hypotonia, colloquially referred to as “floppy infants”, can occur due to a broad range of defects. In 1958, Greenfield, *et. al.*, organized the known syndromes of floppy infants into three groups: (a) progressive cases which worsened over, (b) stationary cases which did not progress, and, finally, (c) cases which showed improvement (8). During this time, Shy, *et. al.* found a “stationary” floppy infant case that uniquely displayed rod-like aggregates in her myofibers. Based on their appearance, Shy, *et. al.*, labeled these structures as “nemaline bodies” and classified the disease as “nemaline myopathy” (9). However, three decades passed before the first causative mutation of nemaline myopathy in tropomyosin 3 (*TPM3*) was found by Laing, *et. al.* in 1995 (10). Following this pioneering work, mutations in eight additional causative genes were found to cause nemaline myopathy: nebulin (*NEB*), alpha 1 actin (*ACTA1*), tropomyosin 2 (*TPM2*), troponin T type 1 (*TNNT1*), cofilin 2 (*CFL2*), *KBTBD13*, *KLHL40*, and, most recently, *KLHL41* (11-18).

Clinically, presentation of nemaline myopathy can vary substantially from mild muscle dysfunction to complete akinesia but without any correlation to the number of nemaline bodies, suggesting that these structures are not a primary cause of the muscle dysfunction (19). The underlying pathogenesis of nemaline myopathy remains unresolved, however six of nine causative genes for nemaline myopathy, tropomyosin 3 (*TPM3*), nebulin (*NEB*), alpha 1 actin

(*ACTA1*), tropomyosin 2 (*TPM2*), troponin T type 1 (*TNNT1*), and cofilin 2 (*CFL2*), encode components of the sarcomere thin filament, leading to the current hypothesis that nemaline myopathy is a thin filament disease (10-15).

As described in the previous chapter, the sarcomere thin filament is a helical strand of polymerized actin that anchors directly to the Z-line and spans toward the M-line (7). During muscle contraction, thick filament myosin forms cross-bridges with thin filament actin and physically pulls the Z-line toward the M-line to generate force. Tropomyosin and the troponin complex regulate myosin-actin crosslinking in a calcium-dependent manner. In nemaline myopathy, it is believed that mutations disrupting thin filament proteins result in reduced force generation and subsequent myopathy (20). However, mutations in three proteins with no established association with the sarcomere thin filament, KBTBD13, KLHL40 and KLHL41, have recently been shown to cause nemaline myopathy in patients by an unknown mechanism (16-18). Notably, *KLHL40* mutations frequently occur in severe forms of autosomal-recessive nemaline myopathy (17).

KBTBD13, KLHL40, and KLHL41 belong to the BTB-BACK-Kelch (BBK) protein family, named for the presence of BTB, BACK, and kelch repeat (KR) domains in all family members (KBTBD13 lacks an annotated BACK domain but is still very closely related to other BBK family members) (21). Taken individually, the BTB and kelch domains have a broad variety of protein functions. However, when these domains occur together, BBK proteins are thought to serve as substrate-specific adaptors for the cullin 3 (Cul3) E3 ligase complex, where the BBK proteins mediate the ubiquitination and, in some cases, degradation of their respective substrates (Figure 2.1) (22-29).

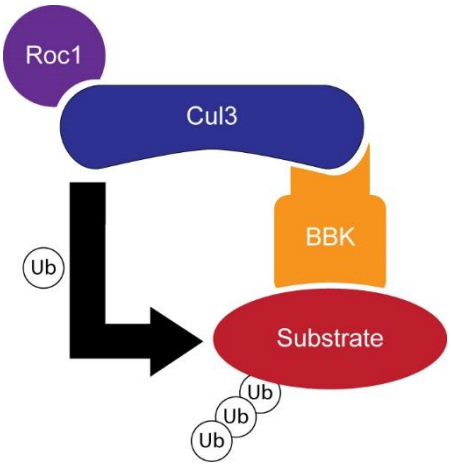

Figure 2.1. Typical function of BBK proteins. Generic overview of the function of BBK proteins. The BBK protein serves a substrate specific adaptor for the Cul3 E3 ligase complex to mediate ubiquitination of its substrate. Roc1 is an E2 ligase that brings the ubiquitin, "Ub", moieties to the Cul3 E3 ligase.

Because nemaline myopathy is so tightly associated with thin filament proteins, it can be hypothesized that these three BBK proteins also regulate the thin filament in some manner, though this has not been demonstrated. Additionally, since other BBK proteins act through the ubiquitin-proteasome system, defining the function of these proteins may facilitate therapeutic manipulation, given the availability of proteasome inhibitors for patient use (30).

While searching for new potential regulators of muscle function, we uncovered a novel muscle-specific transcript, *Klhl40*, that encodes for a protein localizing to the sarcomere I-band and A-band. Deletion of the *Klhl40* locus in mice results in sarcomere defects with subsequent muscle dysfunction and early postnatal lethality which closely phenocopy the muscle abnormalities observed in humans with *KLHL40* mutations (17). I show that Klhl40 binds to Neb, a thin filament protein frequently associated with nemaline myopathy (31), as well as leiomodin 3 (Lmod3), a novel muscle protein highly homologous to leiomodin 2 (Lmod2) which regulates actin at the pointed end of thin filaments (32, 33). Similar to Lmod2, I find that Lmod3 also localizes to the pointed end of sarcomere thin filaments. Unlike most

other BBK proteins that mediate degradation of their substrates, Klhl40 uniquely promotes stability of Neb and Lmod3 and inhibits ubiquitination of Lmod3. Accordingly, loss of Klhl40 reduces Neb and Lmod3 protein in mice as well as in nemaline myopathy patients. By establishing a novel pro-stability function of Klhl40 for the thin filament proteins Neb and Lmod3, my data reveals a molecular basis for nemaline myopathy in patients deficient for KLHL40 and suggests a previously unrecognized unknown role of Lmod3 in maintenance of sarcomere function and nemaline myopathy.

RESULTS

Discovery and characterization of Klhl40

To find new regulators of striated muscle biology, we searched an *in situ* hybridization database for novel transcripts that were enriched in developing muscle structures (34). Within this database, we found that *Klhl40* appeared to have muscle-specific expression which we validated by *in situ* hybridization in mouse embryos (Figure 2.2A). This skeletal muscle-specific expression of *Klhl40* is preserved into adulthood with additional low level expression in the heart that was not apparent in embryos (Figure 2.2B). However, quantitative PCR (qPCR) analysis revealed modest, but reproducible, expression of *Klhl40* in the brain which became an important consideration when analyzing the phenotype of *Klhl40* deficient mice (Figure 2.2C).

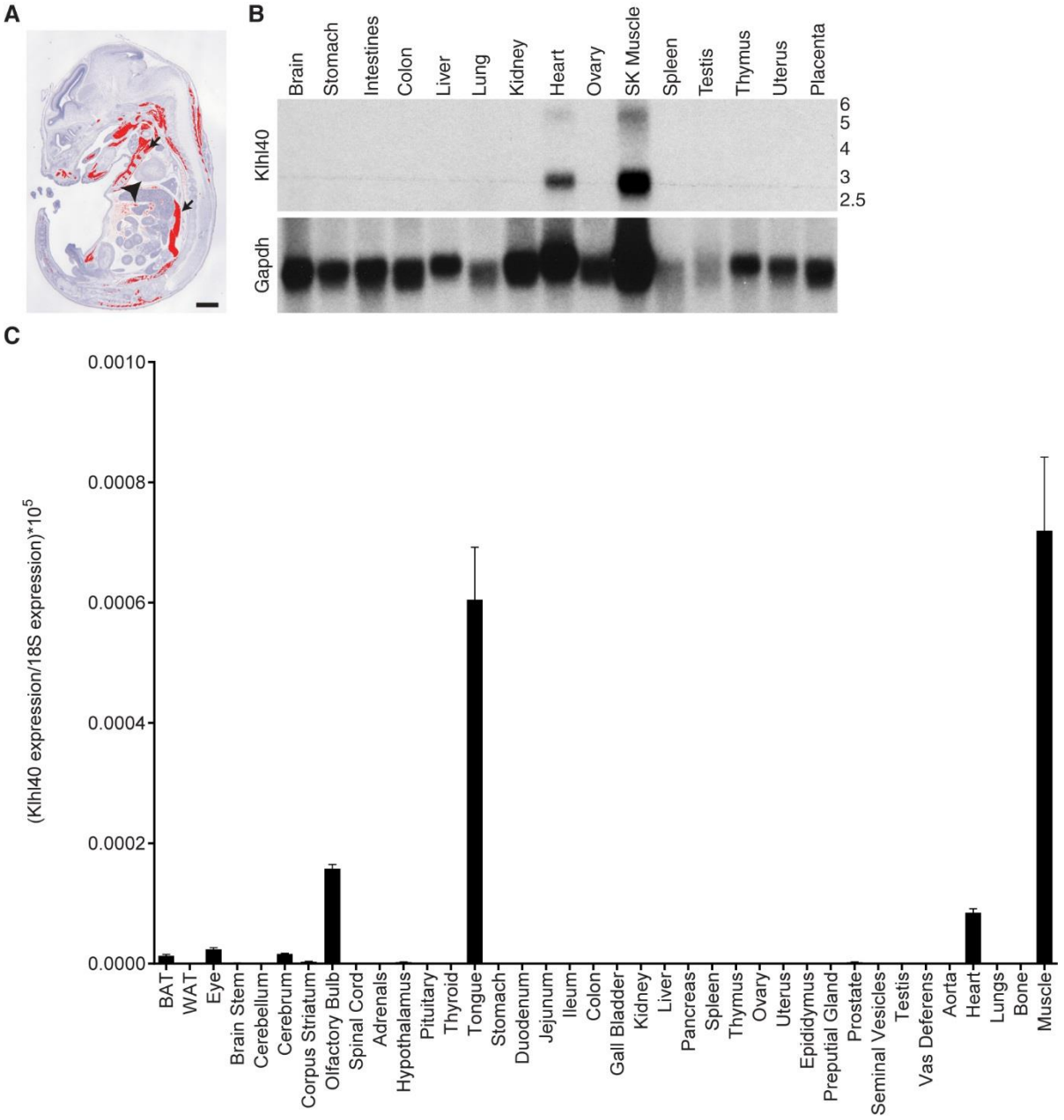

Figure 2.2. *Klhl40* is expressed specifically in skeletal muscle. (**A**) Sagittal sections of E15 embryos were probed for Klhl40 mRNA using antisense radioisotopic probes. Signal for Klhl40 (pseudo-colored red) only appears in developing muscle. Black arrows point to representative developing intercostal and back muscles from rostral to caudal, respectively. Black arrowhead denotes heart. Scale bar: 1mm. (**B)** Northern blot on adult mouse tissues for Klhl40 and Gapdh (loading control) shows expression in skeletal muscle and heart. SK muscle denotes skeletal muscle. (**C**) qPCR analysis of *Klhl40* expression in multiple C57BL/6 adult tissues shows high enrichment for tongue (largely composed of skeletal muscle) and skeletal muscle. There is a lesser degree of expression in the heart and olfactory bulb (brain). “BAT” and “WAT” are brown adipose tissue and white adipose tissue, respectively. Values are normalized to 18S ribosomal RNA. Data are presented as mean ± SEM.

In addition to analyzing *Klhl40*'s tissue specificity, I analyzed the expression of *Klhl40* during heart and skeletal muscle development and found it to be modestly up-regulated (Figure 2.3, A and B). However, because *Klhl40* was not detectable by *in situ* in the heart, the cardiac developmental regulation is likely not biologically significant. *Klhl40* also showed increased expression during C2C12 differentiation (Figure 2.3C) but was not significantly regulated during mechanical overload hypertrophy, denervation atrophy, or muscle regeneration following cardiotoxin injury (data not shown). Overall, our expression data largely confirmed the muscle specificity of *Klhl40*, but did not provide any obvious insights into Klhl40's potential function.

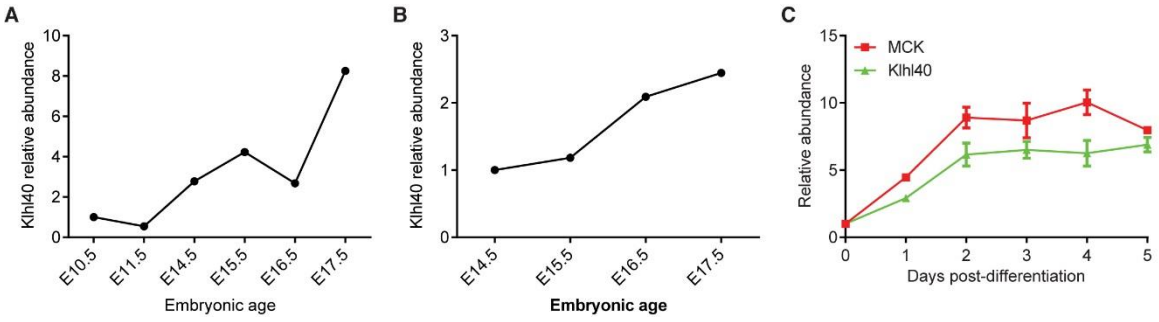

Figure 2.3. Klhl40 regulation during heart and skeletal muscle development and in differentiating C2C12 cells. (**A, B, C**) qPCR analysis of *Klhl40* expression in (**A**) developing heart, (**B**) developing skeletal muscle, and (**C**) differentiating C2C12 cells. (**C**) Muscle creatine kinase (MCK), is known to be up-regulated during muscle development and is shown as a positive control (35). Values are normalized to 18S ribosomal RNA. (**C**) Data are presented as mean ± SEM.

Generation of a loss of function Klhl40 mouse model

At the time, it was unclear to us how to extrapolate the function of Klhl40 from expression analysis and basic molecular characterization (i.e. cellular localization). Thus, to determine the function of Klhl40, we took a genetic loss-of-function approach to delete Klhl40 and assess the outcome of muscle function in the absence Klhl40. Mutant Klhl40 mice were

generated by replacing the *Klhl40* coding sequence (CDS) with the *β-galactosidase* (*lacZ*) gene (Figure 2.4). Mice heterozygous and homozygous for this knockout (KO) allele are referred to as *Klhl40*$^{+/-}$ or HET and *Klhl40*$^{-/-}$ or KO, respectively, within this chapter. Replacing the *Klhl40* coding sequence with *lacZ* generated a null allele for *Klhl40* and provided an additional tool to analyze *Klhl40* expression by utilizing the lacZ protein expressed under the control of the endogenous *Klhl40* promoter.

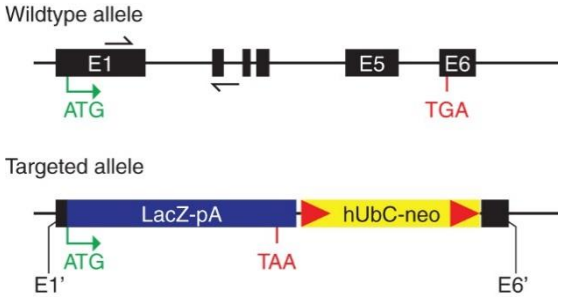

Figure 2.4. Targeting strategy for *Klhl40* knockout allele. The coding sequence of *Klhl40* (not including the start codon) as well as 23 nucleotides past the stop codon (nucleotides 172-5816 of NCBI reference sequence NC_000075.6) were replaced with a *β-galactosidase* (LacZ-pA) and neomycin (hUbC-neo) expression cassette. The promoter and the 5' (E1') and 3' (E6') untranslated regions of *Klhl40* were left intact allowing for *LacZ* expression to be driven by the endogenous promoter. Neomycin expression was driven by the human ubiquitin C (hUbC) promoter. Black boxes represent exons and half arrows indicate location of qPCR primers that were used to analyze Klhl40 mRNA. Red triangles denote loxP sites and ATG and TGA/TAA represent translational start and stop sites, respectively.

Tissues expressing lacZ were visualized by incubation with a colorimetric reporter, X-gal, which, upon cleavage by lacZ, generates an insoluble blue precipitate. By lacZ staining *Klhl40*$^{+/-}$ mouse tissues, we verified that *Klhl40* is exclusively expressed in embryonic, neonatal, and adult skeletal muscle (Figure 2.5, A-C).

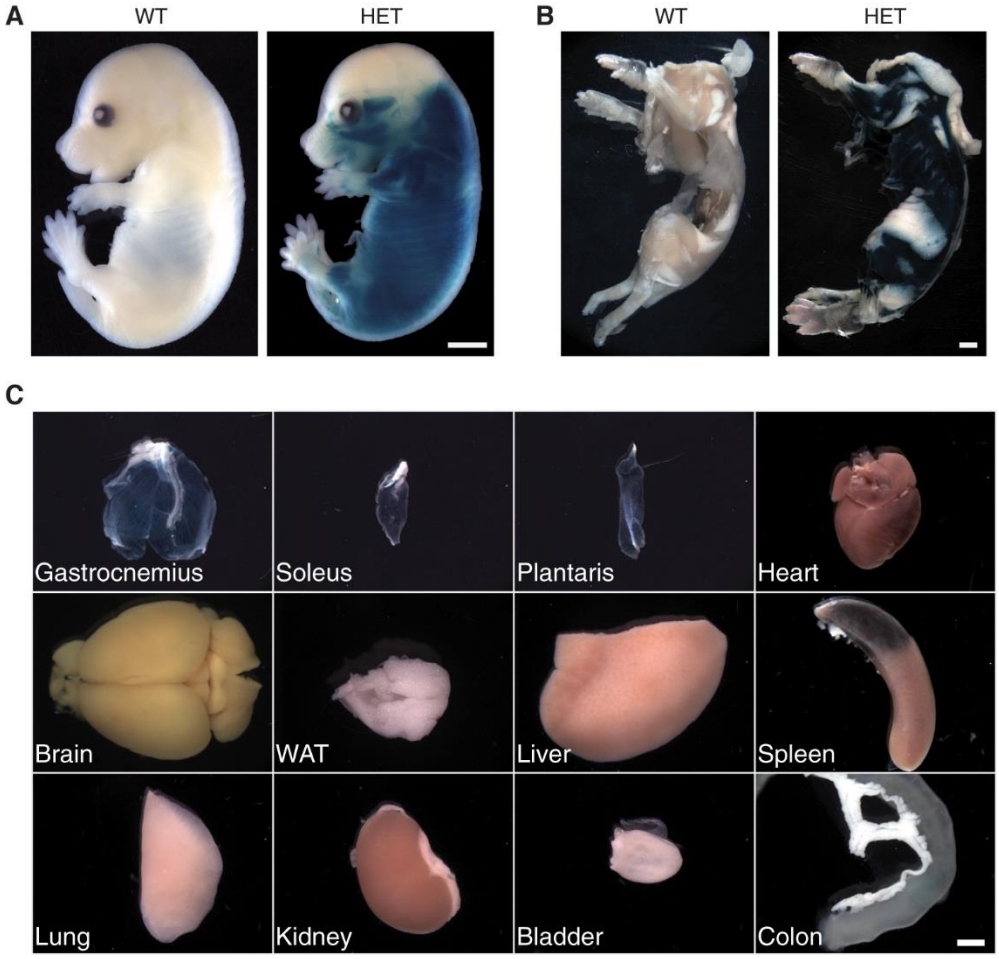

Figure 2.5. *LacZ* knock-in into *Klhl40* locus shows muscle specific lacZ staining. (**A**, **B**) X-gal staining of *Klhl40* promoter driven lacZ reporter shows signal (blue stain) only in skeletal muscle of (**A**) HET E15 and (**B**) P8 mice, respectively. HET mice contain the knocked-in allele while WT mice lack the allele. (**A**, **B**) Scale bar: 1mm. (**C**) X-gal staining HET adult tissues also show muscle specific staining. Note that the black lesion on the spleen is due to a hemorrhage and not lacZ activity. Scale bar: 2mm.

Histological sectioning of muscle confirmed that lacZ was only expressed in myofibers and not connective tissues (Figure 2.6A). *Klhl40*$^{+/-}$ hearts showed only punctate lacZ staining which is consistent with low expression of *Klhl40* in the heart (Figure 2.6B).

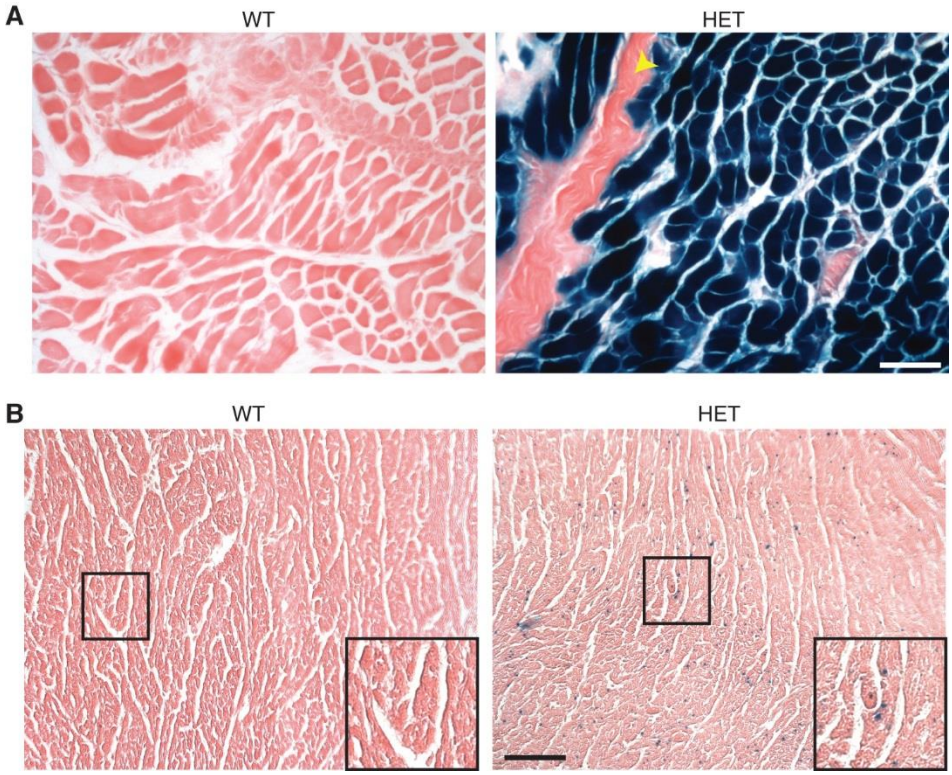

Figure 2.6. *LacZ* knock-in into *Klhl40* locus shows staining only in myofibers and punctate staining in myocardium. (**A**, **B**) X-gal stained sections of P8 (**A**) skeletal muscle and (**B**) heart. (**A**) Staining only occurs in HET myofibers and not connective tissue (yellow arrow). (**B**) In myocardium, only punctate staining occurs in HET hearts that is absent from WT hearts. Punctate staining possibly indicative of low lacZ reporter expression. Boxed area is enlarged in inset. (**A**, **B**) Scale bar: 50μm.

Loss of Klhl40 results in neonatal lethality.

Klhl40$^{-/-}$ mice were born at Mendelian ratios. Using qPCR *Klhl40* transcript was not detected in *Klhl40*$^{-/-}$ mice (Figure 2.7). Within several days after birth, it was obvious that *Klhl40*$^{-/-}$ mice were substantially smaller compared to their control littermates, (Figure 2.7, B and C). Furthermore, 50% of the *Klhl40*$^{-/-}$ mice died by 7 days of age and none survived past 3 weeks on a pure C57BL/6 background (Figure 2.7D). Interestingly, on a mixed background, there was a single mouse that survived to adulthood. Although this mutant mouse was smaller in size compared to its littermates it was healthy and capable of breeding (data not shown). Thus, it is possible that some unknown gene or genes can compensate for the loss of *Klhl40*.

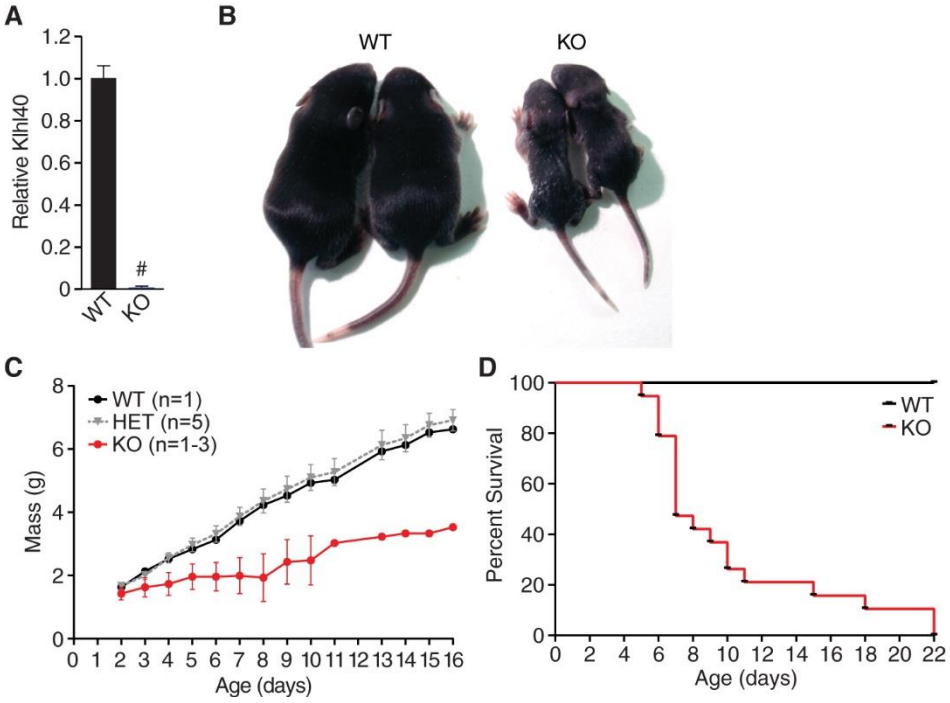

Figure 2.7. Loss of Klhl40 causes stunted growth and early lethality. (**A**) qPCR analysis of *Klhl40* transcript in P8 quadriceps in mice of the indicated genotypes. Values are normalized to 18S ribosomal RNA. N=3 for all genotypes. # $p<0.05$. (**B**) Representative image of surviving P8 *Klhl40* KO pups with WT littermates. (**C**) Growth curve of *Klhl40* WT, HET, and KO mice from 2-16 days of age. KO mice show blunted growth within several days of age. Number of animals for each genotype is indicated. KO mice numbers vary from 1-3 due to death of mice as time progressed. (**D**) Survival curve of WT versus KO *Klhl40* mice shows early neonatal lethality in KO mice. WT n=21 and KO n=17.

A shortcoming of the targeting strategy used to generate *Klhl40*$^{-/-}$ mice is that the *Klhl40* gene was deleted globally and not in a specific tissue. Although we showed that *Klhl40* expression is largely restricted to skeletal muscle and heart, there was modest expression in the brain. To prove that our phenotype was due to loss of *Klhl40* in striated muscle, we generated transgenic mice expressing *Klhl40* under the control of the muscle-specific promoter, muscle creatine kinase (*MCK*), and bred the allele into the KO background (35, 36). The *MCK* promoter fragment used has been shown to be essentially specific to skeletal muscle compared to non-muscle tissues although, it does slightly overexpress in the heart but at orders of magnitude less than skeletal muscle (>10^4 expression in skeletal muscle

compared to 2-3 fold expression in heart relative to non-muscle tissues) (36). WT and KO mice with the *MCK-Klhl40* transgene are referred to as “WT Tg” and “KO Tg”, respectively. At 10 days of age (P10), the *MCK-Klhl40* transgene overexpressed approximately 3-fold in WT Tg skeletal muscle, but for KO Tg mice, it restored *Klhl40* expression to WT levels (Figure 2.8A). The *MCK-Klhl40* transgene was sufficient to completely rescue the KO phenotype such that KO Tg mice were indistinguishable from control littermates with normal growth into adulthood (Figure 2.8, B and C; data not shown for adults), confirming that loss of *Klhl40* from striated muscle was responsible for the neonatal lethal phenotype.

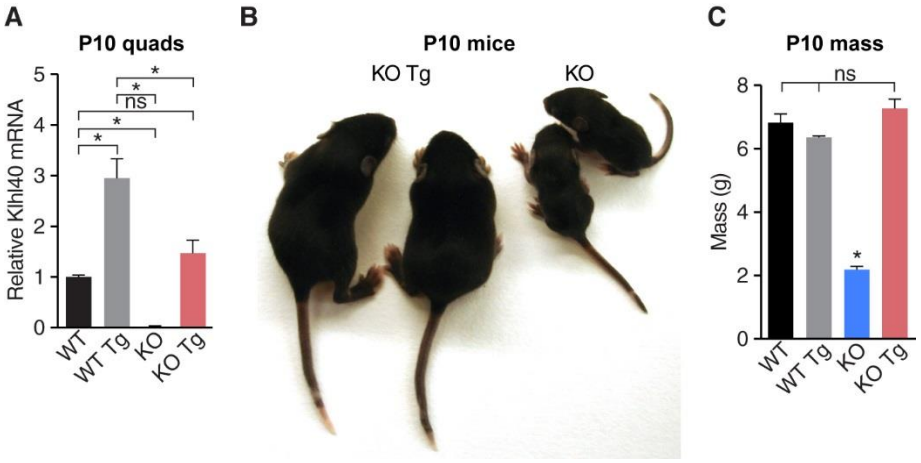

Figure 2.8. Muscle-specific over-expression of *Klhl40* rescues Klhl40 KO lethality. (**A**) qPCR analysis of *Klhl40* mRNA in P10 quadriceps of *Klhl40*$^{+/+}$ (WT), *Klhl40*$^{+/+}$*;MCK-Klhl40* (WT Tg), *Klhl40*$^{-/-}$ (KO), and *Klhl40*$^{-/-}$*;MCK-Klhl40* (KO Tg) mice shows approximately 3-fold overexpression of *Klhl40* in WT Tg mice. *Klhl40* transcript is restored to near-normal levels in KO Tg mice. N=3 for all genotypes. (**B**) Representative image of KO Tg and KO mice shows complete rescue of KO phenotype with muscle-specific overexpression of *Klhl40*. (**C**) Masses of KO Tg mice are indistinguishable from WT and WT Tg mice. WT n=5, WT Tg n=3, KO n=5, and KO Tg n=4. * statistically significant difference with a false discovery rate (FDR) of 0.05. Data are presented as mean ± SEM.

A comprehensive analysis of *Klhl40* in 5 day old (P5) heart, quadriceps muscle, and diaphragm muscle from WT, WT Tg, KO, and KO Tg mice showed that the *MCK-Klhl40* transgene expressed less *Klhl40 mRNA* in KO Tg mice compared to WT (Figure 2.9; protein

levels unknown). This is different compared to P10 KO Tg and WT mice that express equal levels of *Klhl40*. Thus, this transgene may be regulated postnatally, which has not been previously reported for the 4.8kb promoter region used to generate these *MCK-Klhl40* mice. In addition, despite previous publications of minimal over-expression of the *MCK* promoter in heart, at P5, over-expression of Klhl40 in the heart exceeded skeletal muscle over-expression. Mice with the *MCK-Klhl40* transgene at much older ages (greater than 3 weeks) were noted to have dilated hearts, although this has not affected their survival beyond one year of age (data not shown).

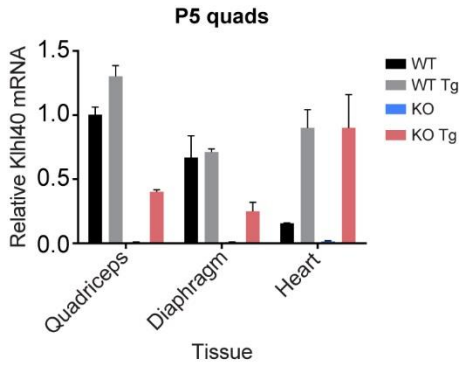

Figure 2.9. Expression of *Klhl40 from MCK-Klhl40* transgene in P5 mice. qPCR analysis of *Klhl40* expression in quadriceps, diaphragm, and heart from P5 *Klhl40*$^{+/+}$ (WT), *Klhl40*$^{+/+}$*;MCK-Klhl40* (WT Tg), *Klhl40*$^{-/-}$ (KO), and *Klhl40*$^{-/-}$*;MCK-Klhl40* (KO Tg) mice. Values are normalized to 18S and set relative to WT quadriceps. Data are presented as mean ± SEM.

Klhl40 localizes to the sarcomere I-band and A-band.

To better understand how loss of Klhl40 from skeletal muscle causes lethality, we analyzed the subcellular localization of Klhl40 in mature myofibers. To visualize Klhl40 localization, we electroporated the flexor digitorum brevis (FDB) of adult mice with Klhl40 C-terminally fused with EGFP (Klhl40-EGFP). We utilized second harmonic generation (2HG) as previously described to localize Klhl40-EGFP relative to myosin (37). In a modified EDTA-

Ringer's solution that normally serves to relax skinned myofibers (38), Klhl40-EGFP signal concentrated at the I-band (Figure 2.10A). However, muscle bathed in a rigor solution that normally results in a sustained muscle contraction showed localization of Klhl40-EGFP to the A-band with fainter localization to the I-band (Figure 2.10B) (38).

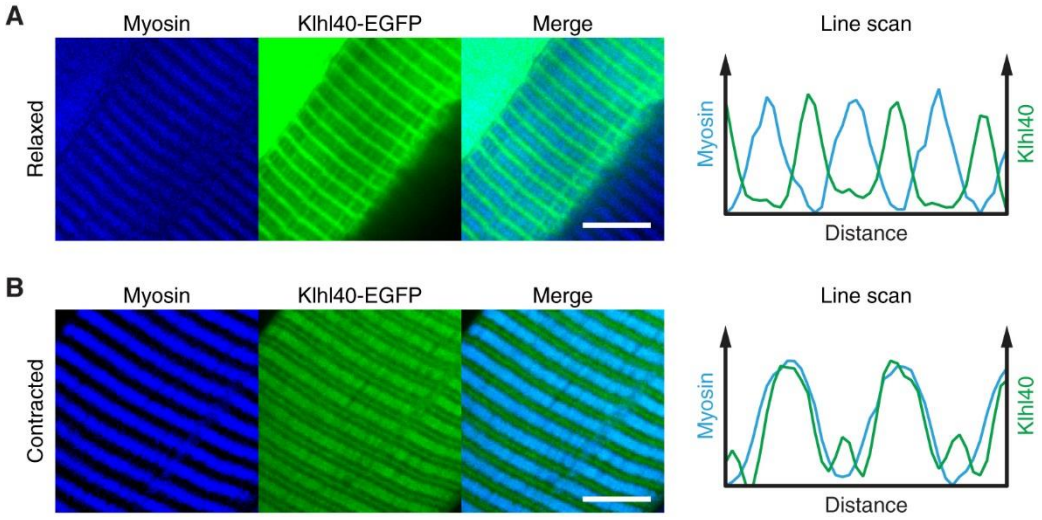

Figure 2.10. Klhl40 localizes to sarcomere I-band and A-band. (**A**, **B**) Klhl40-EGFP localization relative to myosin in (**A**) relaxed muscles and (**B**) contracted muscles shows that Klhl40 dynamically localizes to the I-band and A-band, respectively. Scale bar: 5μm.

α-actinin (Actn1a) and tropomodulin (Tmod4), which are known I-band and A-band proteins, respectively, did not change localization in relaxed and contracted muscles (Figure 2.11, A-D) (39). However, it should be noted that the fibers in these analyses were not skinned and thus penetration of these solutions to elicit muscle relaxation or contraction is dubious. On the other hand, muscle contraction could be seen grossly for dissected feet bathed in rigor solution. In addition, Tmod4 showed clear doublets which is a known phenomenon for hypercontracted muscles (the muscles were not relaxed based on the gross appearance of the foot) (40). Yet, because this experiment was not performed in a manner that has been described before, we can only conclude that Klhl40 is capable of localizing to both the I-band

and A-band. Whether this occurs due to muscle relaxation or contraction must be shown under proper physiologic conditions.

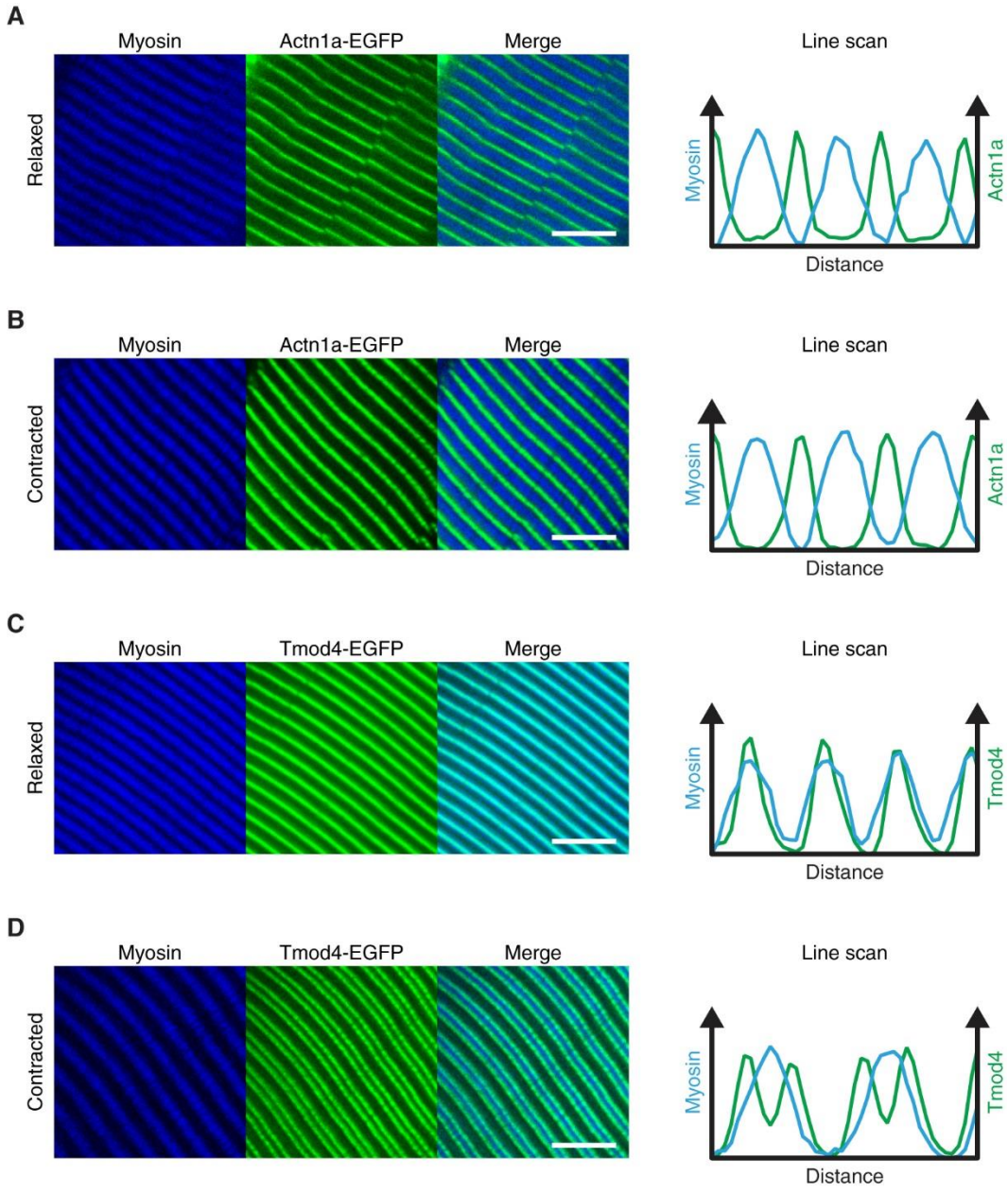

Figure 2.11. Actn1a-EGFP and Tmod4-EGFP do not change localization in relaxed or contracted muscles. (**A**, **B**) Actn1a-EGFP and (**C**, **D**) Tmod4-EGFP localization relative to myosin visualized by second harmonic generation in (**A**, **C**) relaxed and (**B**, **D**) contracted muscles. (**A**, **B**) Actn1a-EGFP remains in the I-band while (**B**, **D**) Tmod4-EGFP remains in the A-band regardless of the contractile state of muscle. Note that Tmod4-EGFP appears as a doublet in contracted muscle likely due to hyper-contraction of sarcomeres that causes pointed ends of actin to run past each other over the M-line (40). Scale bar: 5μm.

Klhl40 deficient skeletal muscles have abnormal sarcomere structure and function.

To find the defect in skeletal muscle responsible for the observed lethality, we performed histologic analysis of limb and diaphragm muscles from neonatal *Klhl40*$^{-/-}$ mice. In stark contrast to the lethal phenotype, basic histologic analysis of muscles showed no obvious defects (fiber size heterogeneity, fibrosis, centralization of nuclei, etc.) aside from a reduction in fiber size, which can be expected in a muscle that is grossly smaller (Figure 2.12, A and B).

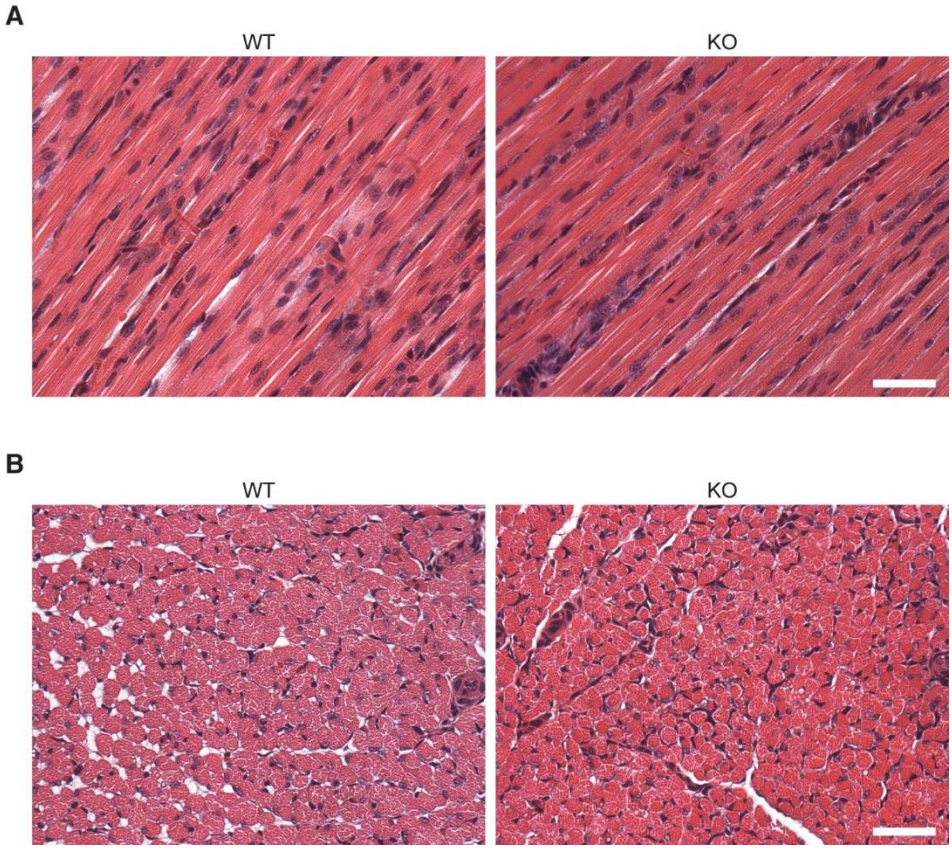

Figure 2.12. *Klhl40* KO skeletal muscles are smaller, but show no overt pathology. (**A**, **B**) P5 quadriceps (**A**) longitudinal and (**B**) transverse sections stained with H&E. (**A**, **B**) No gross defects are obvious aside from the smaller size of KO fibers. Scale bar: 40μm.

Similarly, the hearts of *Klhl40*$^{-/-}$ mice also lacked any obvious pathology aside from a difference in size (Figure 2.13).

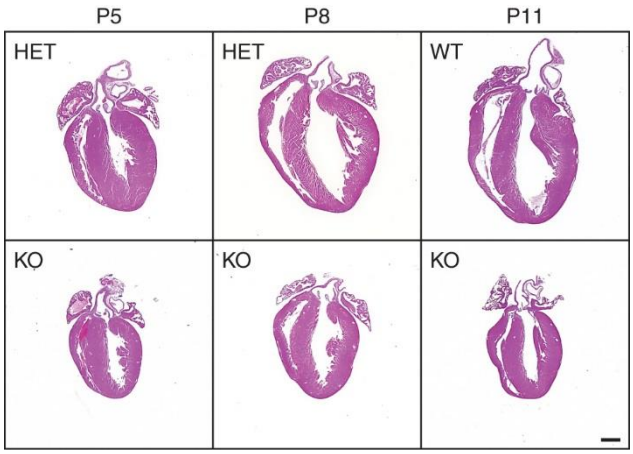

Figure 2.13. *Klhl40* KO hearts are grossly normal. P5, P8, and P11 hearts from HET, WT, or KO mice. KO hearts, though smaller, show no obvious signs of cardiac defects. Scale bar: 5mm.

Because we were unable to find any obvious defects by routine histology, we performed microarray analysis on skeletal muscle from day 0 (P0) pups from WT and KO mice to see whether transcriptional changes may reveal an explanation for the phenotype. We chose P0, as opposed to a later age, to minimize any secondary changes due to malnourishment. Surprisingly, we found a general trend of increased expression in sarcomere genes (Figure 2.14) which led us to suspect that there may be ultrastructural defects in the sarcomere not visible by light microscopy.

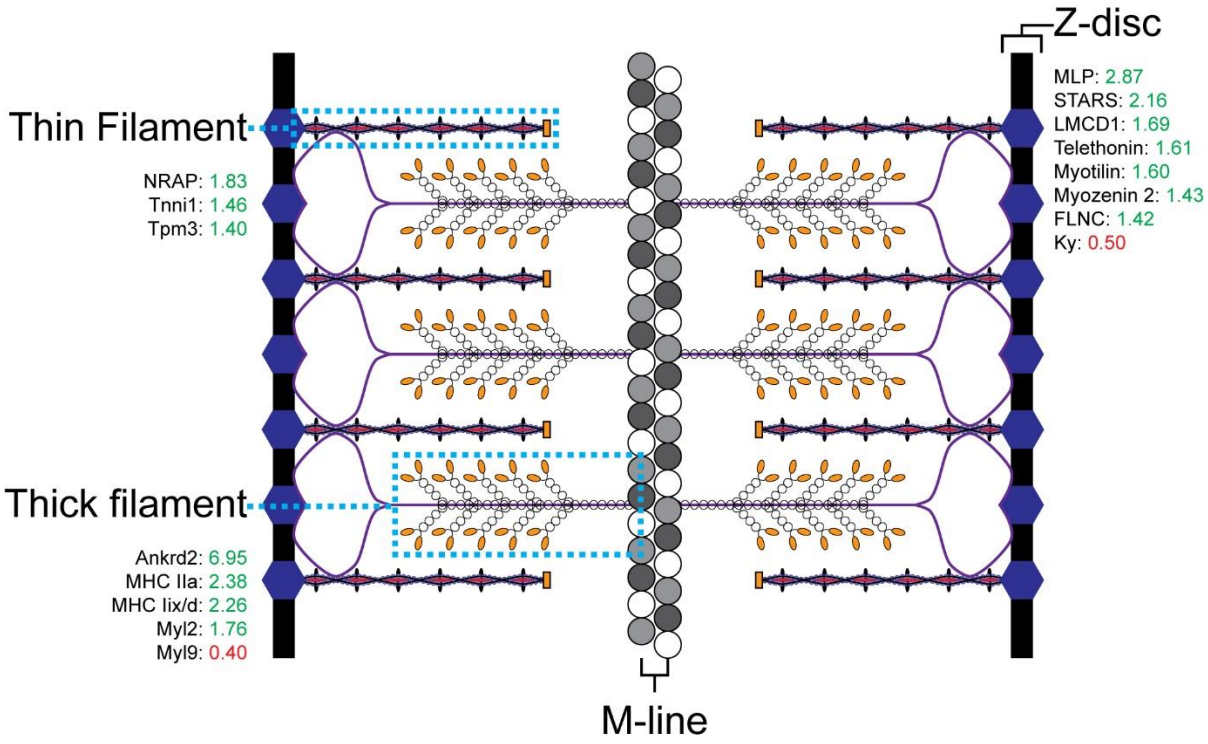

Figure 2.14. Sarcomere genes regulated in P0 *Klhl40* KO skeletal muscle. Schematic of sarcomere showing fold changes (determined by Illumina microarray) of genes in *Klhl40* KO compared to *Klhl40* WT skeletal muscle. General localization of protein products of regulated genes are shown next to major sarcomere structures. Raw data is available the NCBI Gene Expression Omnibus accession number GSE56570.

Thus, we examined WT and KO quadriceps and diaphragm muscles from day 10 (P10) and day 8 (P8) mice using electron microscopy performed by the UT Southwestern Electron Microscopy Core Facility. Examining skeletal muscle at P8 and P10 was chosen to ensure that the phenotype would be sufficiently severe to capture defects by electron microscopy. The sarcomere structure was observed in both genotypes, but there was a distinct presence of Z-line streaming in *Klhl40*$^{-/-}$ muscle, a phenomenon which occurs in several muscle disorders and is indicative of sarcomere damage (Figure 2.15, A and B) (7). Some myofibers had a complete loss of sarcomere structure with widened Z-discs that resembled nemaline bodies present in NM (Figure 2.15C) (31).

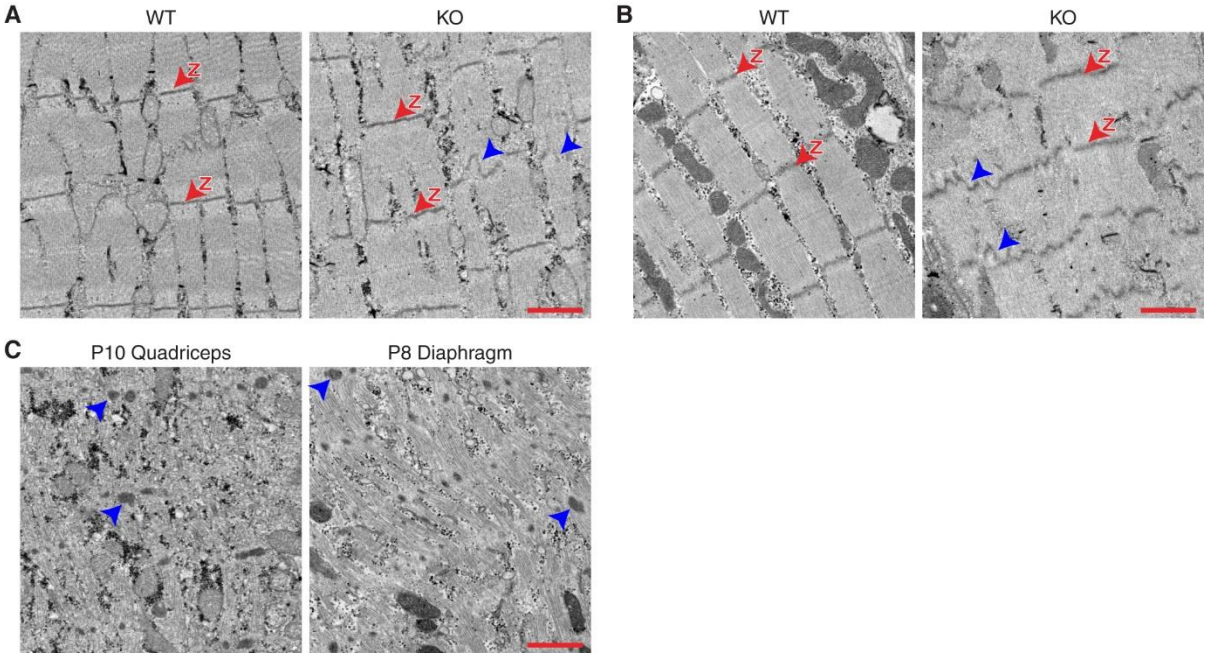

Figure 2.15. Klhl40 KO mice skeletal muscle display Z-line streaming and nemaline-like bodies. (**A**, **B**) EM analysis of longitudinal sections of (**A**) P10 quadriceps and (**B**) P8 diaphragms from WT and KO mice. Red "Z"s with red arrowheads indicate representative Z-lines in each section. Blue arrowheads denote representative abnormal Z-line morphologies. (**C**) Representative images of severely affected myofibers in P10 quadriceps and P8 diaphragm KO muscles. Blue arrow heads denote nemaline rod-like Z-discs. (**A**, **B**, **C**) Scale bar: 1μm.

Because a small subset of fibers had dramatic disorganization of sarcomeres, we reasoned that some of these fibers may be visible at the light microscopy level. Accordingly we found several fibers in quadriceps and diaphragm muscles that resembled the highly disorganized fiber seen by electron microscopy (Figure 2.16). These fibers were rare and only observable by confocal microscopy. It should be noted for future studies that conventional microscopy could not resolve Z-lines to the extent we required due to obscuration by structures out of the plane of focus.

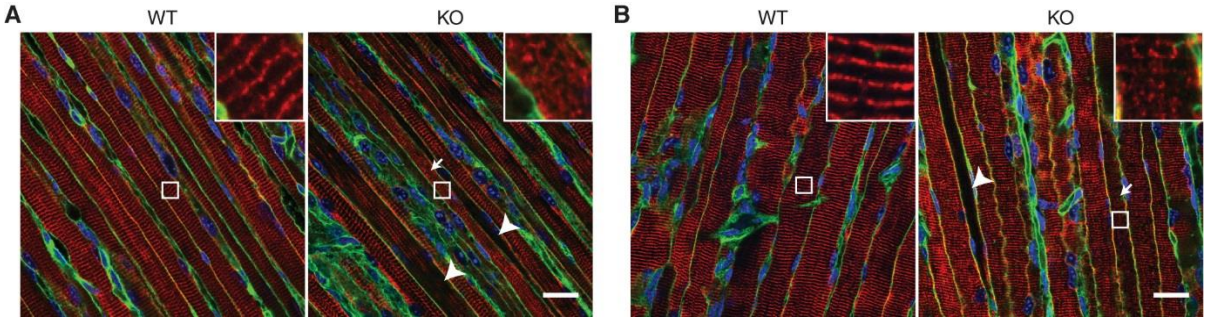

Figure 2.16. Some sarcomere defects are visible in *Klhl40* KO skeletal muscles. (**A**, **B**) Longitudinal sections of (**A**) P5 quadriceps and (**B**) P8 diaphragm muscles from WT and KO mice stained with desmin (red), DAPI (blue), and wheat-germ agglutinin (WGA; green). White arrows indicate disrupted myofibers. White arrow heads denote fibers staining abnormally for desmin that are more frequent in, but not specific to, KO muscles. Insets show normal striated pattern of Z-lines in WT muscles, but some KO fibers have complete loss sarcomere organization. Scale bars: 20μm.

A question that remained was whether sarcomere defects were as severe in younger KO mice. We analyzed diaphragms of one day old (P1) WT and KO mice and were surprised to find that the sarcomeres were comparable between the two genotypes (Figure 2.17). Thus, the sarcomere defects we see at older ages may be due to progressive muscle damage, although the inciting factor was not clear.

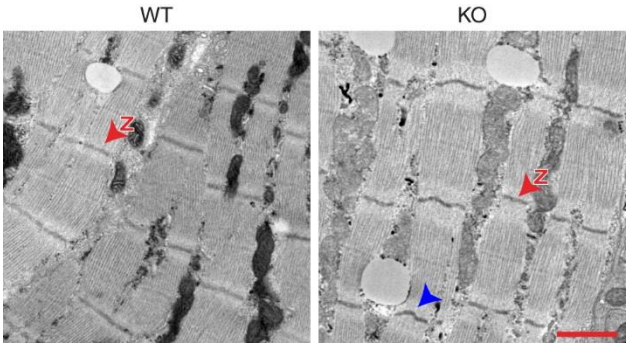

Figure 2.17. P1 *Klhl40* KO muscles are similar to *Klhl40* WT. EM analysis of longitudinal sections of P1 diaphragms from *Klhl40* WT and KO mice. Red "Z"s with red arrowheads indicate representative Z-lines in each section. WT and KO muscles are comparable at P1 although subtle Z-line defects may be present (blue arrowhead). Scale bar: 1μm.

Despite the structural defects that we found in one week old mice, they still paled in comparison to the actual phenotype. It was unclear whether these sparse and subtle structural defects could actually amount to any reduction in muscle function. Thus, we decided to test muscle contraction in KO mice, but there were two significant obstacles. First, the failure to thrive phenotype had a very early onset. Testing muscle function after the mouse became severely malnourished would likely produce spurious conclusions. Therefore, we had to test muscle function well before the onset of severe malnourishment which growth data suggested to P1 mice or younger. But, this presented the second obstacle: the technical limitation of testing muscle contraction on neonatal muscles due to their fragility and size. To overcome this limitation, we tested muscle contraction of intact P1 hindlimb, similar to a previously published protocol (41), foregoing the need to dissect out individual muscles. These experiments were done by our collaborators, Jonathan Doering and Rob Grange at Virginia Tech. The maximum force generated during tetanic of the intact hindlimb showed over a 50% reduction in normalized force when comparing KO muscle to control littermates (Figure 2.18). This result was especially incredible considering the lack of defects seen in P1 KO mice, and indicated that functional defects preceded dramatic structural defects.

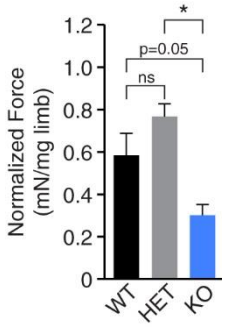

Figure 2.18. P1 *Klhl40* KO muscles show decreased contractile force. Maximum contractile force of P1 WT, HET, and KO hind limb following 150Hz of stimulation and normalized to limb mass. KO muscle shows greater than 50% loss of force compared to both WT and HET mice. WT n=6, HET n=17, and KO n=8. * statistically significant with FDR of 0.05. Data are presented as mean ± SEM.

Because Klhl40 is also present in the heart, we analyzed KO mice for cardiac defects. We showed that despite the expected smaller heart size, KO hearts of various ages displayed no signs of hypertrophy or dilation, which are typical indicators of impending or present heart failure, respectively (Figure 2.13) (42). Additionally, echocardiography of P5 mice showed no decrease in cardiac contractility based on fractional shortening, although there was approximately a 15% reduction in heart rate (Figure 2.19, A and B).

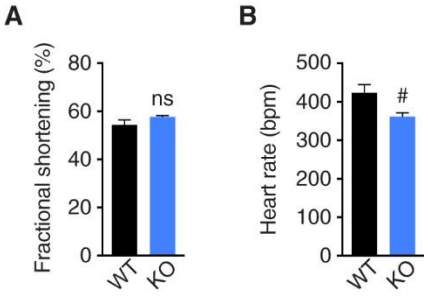

Figure 2.19. *Klhl40* KO hearts display no contractile defects. (**A**, **B**) P5 WT (n=3) and KO (n=6) (**A**) fractional shortening and (**B**) heart rate as determined by echocardiography. Fractional shortening is comparable between WT and KO, but heart rate is decreased 15% in KO mice. # $p<0.05$. Data are presented as mean ± SEM.

Despite no loss of cardiac contractility, we found that *Myh7* (β-myosin heavy chain; bMHC), a sensitive marker of cardiac stress, was increased approximately 24 fold in KO hearts, but in the absence of decreased *Myh6* (α-myosin heavy chain; aMHC), as would be expected during pathologic remodeling (Figure 2.20) (42). It is possible that *Klhl40* KO hearts may inevitably develop a functional defect based on the increased expression bMHC, but a cardiac-specific deletion of *Klhl40* was needed to test this hypothesis.

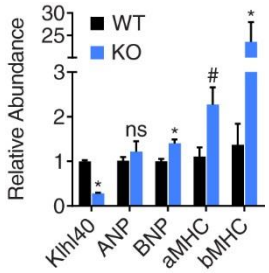

Figure 2.20. *Klhl40* KO heart have altered expression of heart failure markers. qPCR analysis of *Klhl40*, *ANP* (atrial natriuretic peptide), *BNP* (brain natriuretic peptide), *Myh7* (aMHC), and *Myh6* (bMHC) in hearts of P6 WT and KO mice shows elevated expression of bMHC in KO hearts. Note that apparent expression of Klhl40 in KO hearts is background primer dimerization (data not shown). N=5 for both groups. * statistically significant difference with a false discovery rate (FDR) of 0.05. # statistically significant with $p<0.05$ before correcting for multiple comparisons. Data are presented as mean ± SEM.

We attempted to make a conditional deletion of Klhl40 using the targeting strategy outlined in Figure 2.21.

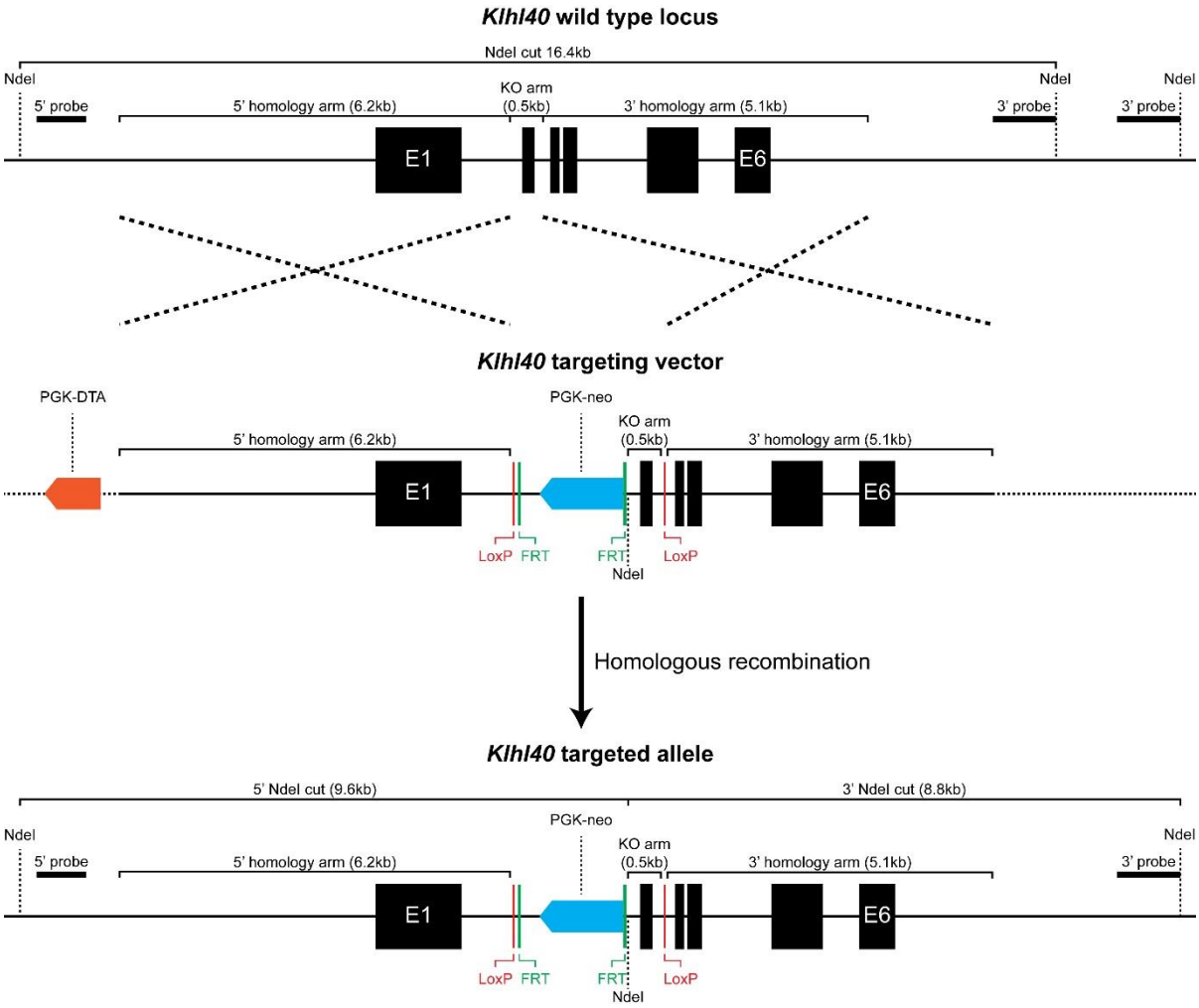

Figure 2.21. Conditional targeting strategy for the *Klhl40* locus. Targeting strategy used to attempt to generate conditionally targeted *Klhl40* mice. Black boxes represent exons. Smaller rectangles with tapered triangle ends represent coding sequences for DTA (orange) and neo (cyan) driven by the PGK promoter. NdeI restriction site was used for Southern screening strategy and the expected cut sizes are shown.

The individual steps to make the targeting vector are outlined in the Methods. ES cells were electroporated and approximately 10% of colonies showed targeting by Southern blot analysis (Figure 2.22). Function of the loxP sites was confirmed by electroporation of cre recombinase into targeted clones and testing for the presence of deletion by PCR analysis (data not shown). Two clones, 1A2 and 1C1, were injected into blastocysts as outlined in the Methods. Coat

color transmitted to the first generation, but there was no evidence of transmission of the targeted allele which was highly unusual. It remains unclear why transmission of the allele failed despite several independent confirmations of targeting preceding blastocyst injection. Because we were unable to generate conditionally generated mice, we could not specifically test the function of *Klhl40* in the heart by a heart-specific deletion.

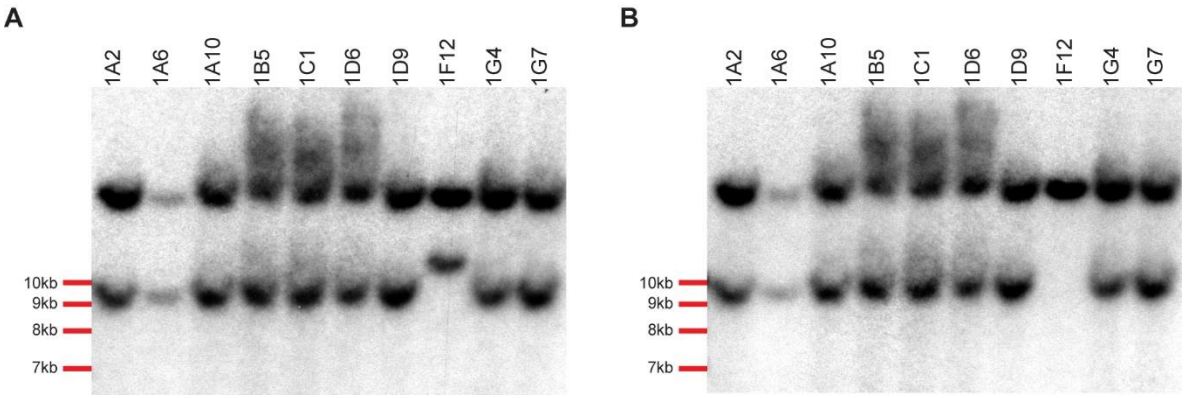

Figure 2.22. Confirmation of *Klhl40* conditionally targeted ES cell clones. (**A**, **B**) Southern blot analysis DNA extracted from expanded ES cell clones initially found to have targeting from a single 96 well plate. DNA was digested with NdeI. Clone names are indicated at top. (**A**) 5' probe and (**B**) 3' probe. Note that 1F12 is mistargeted. 1A2 and 1C1 were chosen for injection into blastocysts.

Klhl40 binds and promotes Neb and Lmod3 protein levels.

Since nemaline is a disease of the thin filament and the Klhl40 KO mice had a nemaline myopathy-like phenotype, we wanted to know whether Klhl40 bound any thin filament proteins. We performed a yeast two-hybrid (Y2H) screen of a human skeletal muscle cDNA prey library using full-length Klhl40 protein as bait. We obtained five unique proteins from the screen (Figure 2.23A). In addition, we performed an independent binding screen by tandem affinity purifying (TAP) Klhl40 tagged at both N-terminus and C-terminus with a 3XFLAG-HA or HA-3XFLAG epitope, respectively (Figure 2.23B). The advantage of performing two separate binding screens was that we were able to more confidently choose which interactions

to analyze further if candidate proteins were present in both assays. Only two proteins met this criterion: Lmod3 and Neb. We validated Klhl40 binding for both Lmod3 and Neb by a separate co-immunoprecipitation (co-IP) experiment in the non-muscle COS7 cell line (43, 44) (Figure 2.23C). Because of Neb's large size (800kDa), we cloned only a fragment of Neb from amino acids 5737-5934 (referred to as Neb_{frag}) (45).

A

Protein	Description	Positive Clones
VDAC1	Mitochondrial voltage dependent anion channel	5
LMOD3	Putative actin nucleating factor	5
CC2D1B	Putative transcriptional repressor	1
AHNAK	Giant scaffold protein	1
NEB	Sarcomere protein	1

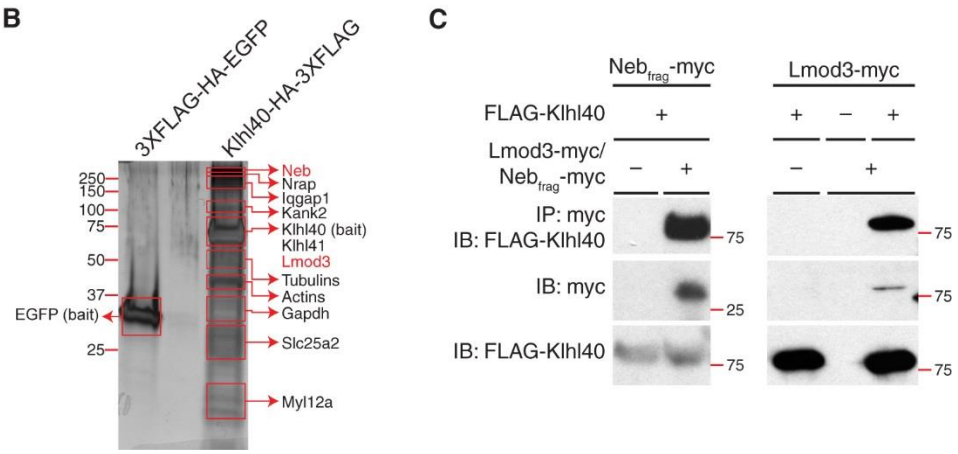

Figure 2.23. Klhl40 binds two thin-filament proteins, Neb and Lmod3. (**A**) Summary of Klhl40 binding partners found by Y2H using Klhl40 bait protein screened against a human skeletal muscle cDNA prey library. "Positive clones" indicates the number of yeast colonies surviving selection that encode for the indicated protein. (B) Top Klhl40 binding partners identified following TAP of Klhl40 from cultured C2C12 myotubes. Shown is a representative silver stained gel with TAP protein from myotubes infected with 3XFLAG-HA-EGFP (negative control) or Klhl40-HA-3XFLAG. Proteins listed next to each box indicate the most abundant protein(s) of the correct molecular weight identified in each corresponding area. Abundance is based on estimated enrichment using exponentially modified protein abundance index (emPAI). TAP of 3XFLAG-HA-Klhl40 protein was also analyzed, but the same top-binding partners were identified (Figure 2.23). (**A**, **B**) Proteins bolded in red (Neb and Lmod3) indicate Klhl40 binding partners mutually identified in both binding screens. (**C**) Co-IP of FLAG-Klhl40 with Lmod3-myc and Neb_{frag}-myc from COS7 cells. The negative control designated "– " refers to empty FLAG vector for FLAG-Klhl40 and empty myc vector for either Lmod3-myc or Neb_{frag}-myc, respectively.

Analysis of additional gel slices as well as 3XFLAG-HA-Klhl40 can be found in Figure 2.24.

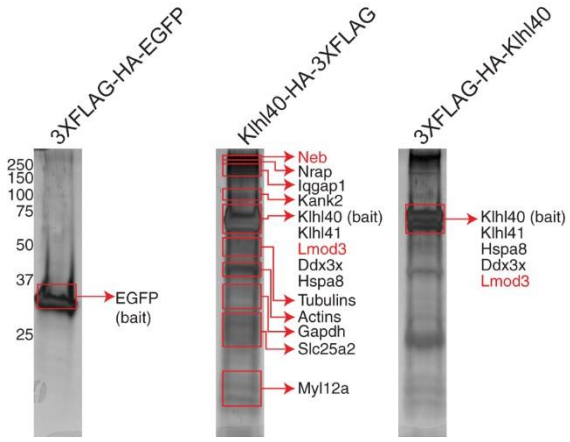

Figure 2.24. Additional gel slices analyzed by mass spectrometry to identify Klhl40 binding partners. Representative silver stained gel of TAP protein from myotubes infected with 3XFLAG-HA-EGFP, Klhl40-HA-3XFLAG, or 3XFLAG-HA-Klhl40. Proteins listed next to each box indicate the most abundant protein(s) of the correct molecular weight identified in each corresponding area (data reproduced from Figure 2.23). Abundance is based on estimated enrichment using exponentially modified protein abundance index (emPAI). All samples were ran on the same gel and are only separated to allow for labeling. Molecular weights for all three lanes are indicated on the left. Only a single region of the 3XFLAG-HA-Klhl40 lane differed from Klhl40-HA-3XFLAG, but mass spectrometric analysis identified the same proteins between both regions. The additional band in 3XFLAG-HA-Klhl40 could be a cleavage product of one of the identified proteins which will require additional analysis to determine. An electronic file listing all identified proteins with their corresponding mass spectrometric information is available upon request.

Despite not identifying Vdac1 by the TAP experiment, it was selected five times in the Y2H analysis, so we performed co-IP of Klhl40 and Vdac1 in COS7 cells, but could not find any evidence of binding between the two proteins (data not shown). This highlights one of the shortcomings of Y2H in obtaining false positive (in addition to false negative) results.

After confirming binding of Klhl40 to Neb and Lmod3, we tested whether Klhl40 influenced Neb or Lmod3 protein levels. A curious observation that we made while performing co-IP experiments with Klhl40 and Lmod3 was that it was difficult to detect Lmod3 protein in the absence of Klhl40. We knew that Klhl40 belongs to the BBK protein family which serves as substrate-specific adaptors for the Cul3 E3 ligase complex and mediate ubiquitination of target proteins (24-29). However, our observations with our co-IP experiments contradicted

this putative function for Klhl40. Thus, we performed an experiment to directly test whether Klhl40 overexpression mediates degradation of Neb_{frag} and Lmod3 or whether Klhl40 increases the levels of both proteins. To our surprise, we found that Klhl40, in COS7 cells, dramatically increases levels of Neb_{frag} and Lmod3 protein levels without a respective change in transcription (Figure 2.25, A and B, Group 1 versus Group 2 and Group 5 versus Group 6 for both protein and mRNA).

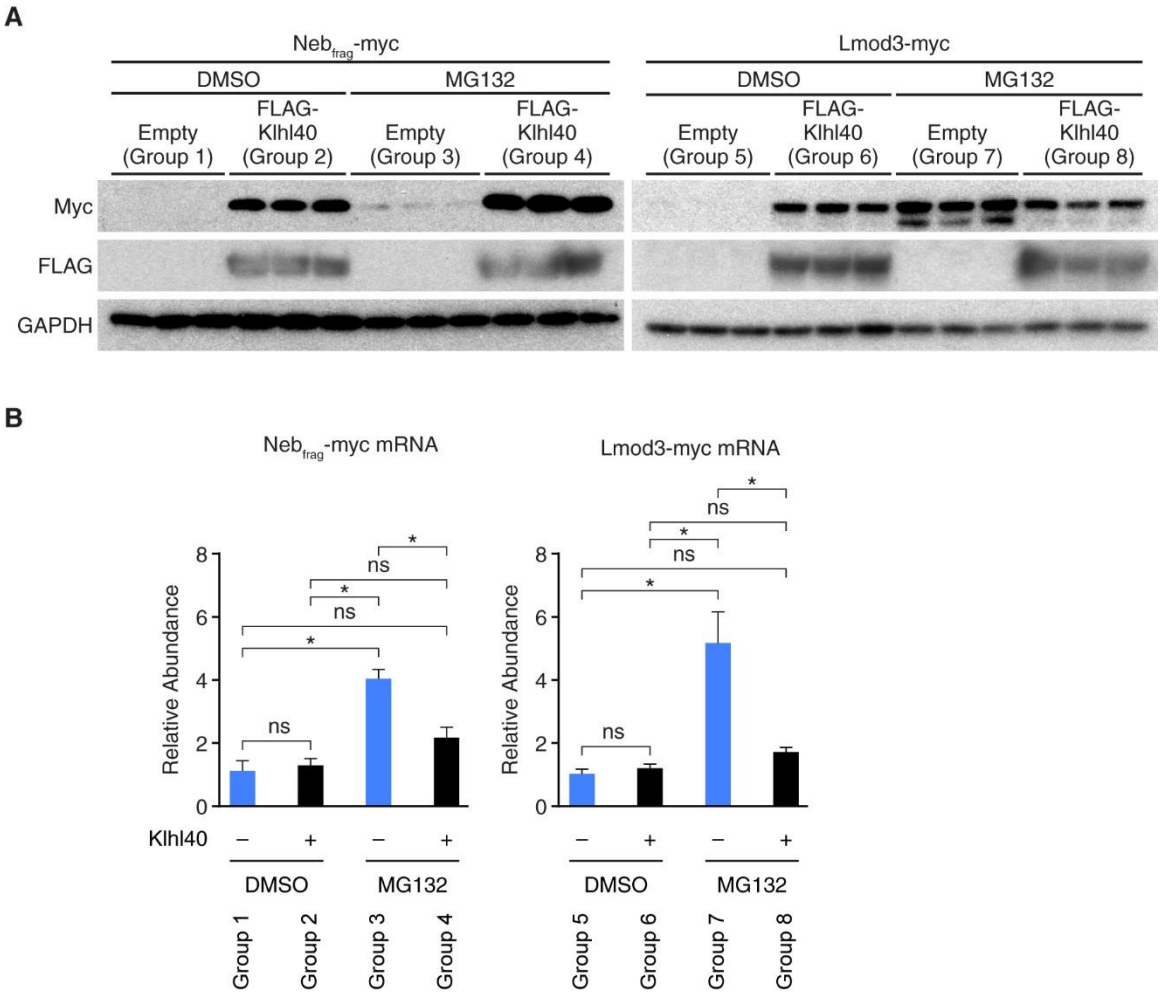

Figure 2.25. Klhl40 increases Neb$_{frag}$ and Lmod3 proteins without a corresponding change in mRNA, and regulates Lmod3 in a proteasome-dependent manner. (**A**) Western blot analysis showing that co-expression of Neb$_{frag}$-myc or Lmod3-myc with Klhl40 in COS7 cells dramatically increases Neb$_{frag}$ (Group 1 versus Group 2) and Lmod3 protein (Group 5 versus Group 6). Addition of proteasome inhibitor, MG132, does not substantially increase Neb$_{frag}$ levels (Group 1 versus Group 3) in the absence of Klhl40. Addition of MG132 dramatically increases Lmod3 levels (Group 5 versus Group 7). (**B**) Corresponding *Neb$_{frag}$-myc* and *Lmod3-myc* mRNA from the experiment performed in (**A**). All values are normalized to 18S and N=3 for all groups. * statistically significant difference with a false discovery rate (FDR) of 0.05. Data are presented as mean ± SEM.

Because previous studies suggested that BBK proteins work through the proteasome, we tested whether the Klhl40-mediated increase of Neb$_{frag}$ and Lmod3 was proteasome dependent. Proteasome inhibition increased Lmod3 protein levels similar to that of Lmod3 co-

expressed with Klhl40, but did not increase Neb_{frag} levels to that of Neb_{frag} co-expressed with Klhl40 (Figure 2.25A, Group 5 versus Group 7 and Group 1 versus Group 3, respectively). In the presence of proteasome inhibitor, Lmod3 protein level was not increased further by addition of Klhl40 (Figure 2.25A, Group 7 versus Group 8). We observed that *Lmod3* transcript was increased in the presence of proteasome inhibitor by approximately five-fold when comparing cells expressing Lmod3 alone in the absence or presence of proteasome inhibitor (Figure 2.25B, Group 5 versus Group 7). However, this small transcriptional change could not possibly account for the dramatic increase in Lmod3 protein upon proteasome inhibition. When comparing Lmod3 protein levels in cells co-expressing Lmod3 and Klhl40 in the absence of proteasome inhibitor to cells expressing Lmod3 alone with proteasome inhibitor, a small increase in protein is noticeable in the latter condition (Figure 2.25A, Group 6 versus Group 7). The 5-fold increase in transcription for cells expressing Lmod3 alone with proteasome inhibitor may account for this small increase in Lmod3 protein (Figure 2.25B, Group 6 versus Group 7). Neb_{frag} mRNA is also increased with proteasome inhibition (Figure 2.25B, Groups 1 and 2 versus Groups 3 and 4) and this may account for the slightly increased Neb_{frag} levels in cells expressing Neb_{frag} alone with proteasome inhibitor compared to cells without proteasome inhibitor (Figure 2.25A, Group 1 versus Group 3).

Based on our findings with the proteasome-dependent stabilization of Lmod3 by Klhl40, we tested whether Klhl40 altered Lmod3 ubiquitination. We found that Klhl40 decreased K48 polyubiquitination of Lmod3, which specifically marks a protein for proteasome-mediated degradation (Figure 2.26) (46). These data suggest that Klhl40 serves to increase Neb and Lmod3 levels and prevents degradation of Lmod3 by blocking ubiquitination and targeting of Lmod3 to the proteasome.

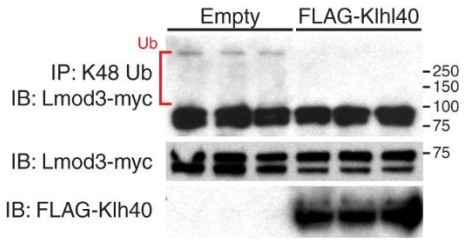

Figure 2.26. Klhl40 decreases Lmod3 ubiquitination. Ubiquitination of Lmod3 protein in COS7 cells in the absence or presence of Klhl40 shows decreased Lmod3-myc ubiquitination in the presence of Klhl40. Ubiquitinated Lmod3-myc is denoted with a red bracket and a "Ub" label.

Mapping the functional domains of Klhl40.

Klhl40 contains three annotated domains: BTB/POZ, BACK, and kelch repeat (KR) domains (Figure 2.27A). To determine which domains are important for regulation of Lmod3 and Neb_{frag}, we generated various Klhl40 mutants lacking combinations of all annotated Klhl40 domains and co-expressed them with Lmod3-myc or Neb_{frag}-myc (Figure 2.27B). Deletion of the KR domain abolished the stabilizing effect of Klhl40 on both Lmod3 and Neb_{frag} levels. On the other hand, deletion of the BTB and/or BACK domains selectively diminished the stabilization of Neb_{frag}. These data suggest that the Klhl40 KR domain plays an essential role in Klhl40-mediated stabilization of both Lmod3 and Neb_{frag} while the Klhl40 BTB and BACK domain are only essential for Neb_{frag}.

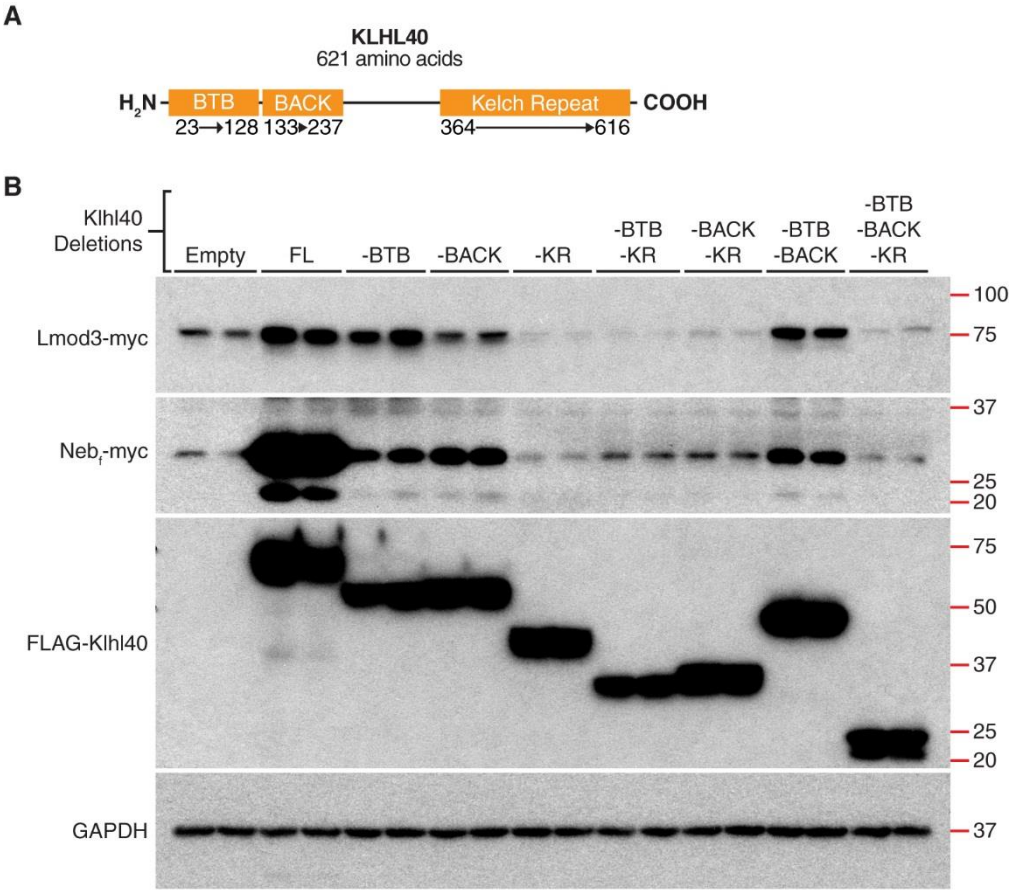

Figure 2.27. Analysis of Klhl40 domains required for Neb$_{frag}$-myc and Lmod3-myc stabilization. (**A**) Schematic representation of Klhl40 protein. Numbers listed below domains indicate amino acid numbers that bound the respective domain. (**B**) Stabilization of Neb$_{frag}$-myc and Lmod3-myc in COS7 cells following co-expression with various domain deleted FLAG-Klhl40 constructs. FL indicates full-length Klhl40, while –BTB, –BACK, –KR, or any combination thereof indicate Klhl40 lacking the specified domain(s).

None of these effects were due to changes in *Neb$_{frag}$* or *Lmod3* transcription (Figure 2.28).

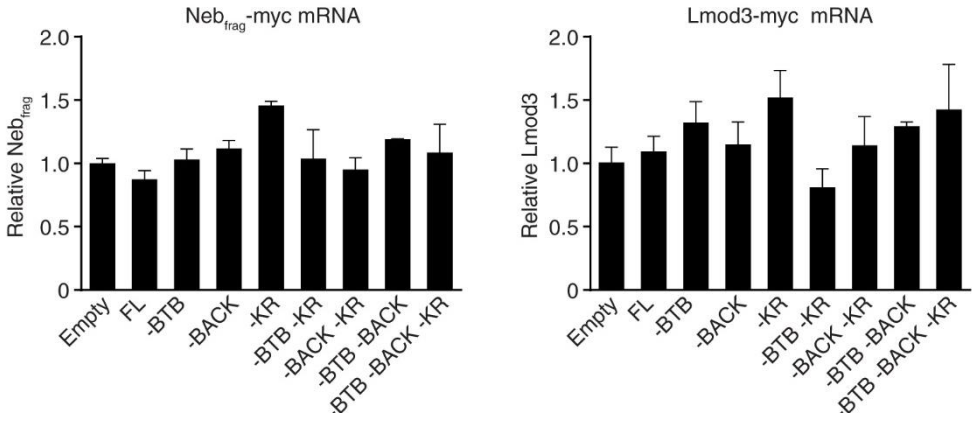

Figure 2.28. Deletion of any Klhl40 domain does not affect transcription of Neb$_{frag}$-myc or Lmod3-myc. Corresponding qPCR analysis for Figure 2.27B shows that expression of *Neb$_{frag}$-myc* and *Lmod3-myc* expression does not change substantially between each of the indicated test groups. Co-transfection of the Klhl40 mutant is indicated below each graph. All values are normalized to 18S and N=2 for all groups. Data are presented as mean ± SEM.

Loss of Klhl40 results in decreased Neb and Lmod3 in mice.

We analyzed protein levels in skeletal muscles from P1 and P8 mice of different *Klhl40* genotypes and found that Neb was decreased by ~50% while Lmod3 was nearly eliminated in Klhl40 KO mice (Figure 2.29, A-D). Notably, *Klhl40*$^{+/-}$ mice also had reduced Lmod3 compared to Klhl40 WT without growth defects or early lethality (Figure 2.29, C and D). Validation of the dot blot technique used to analyze Neb can be found in Figure 2.30.

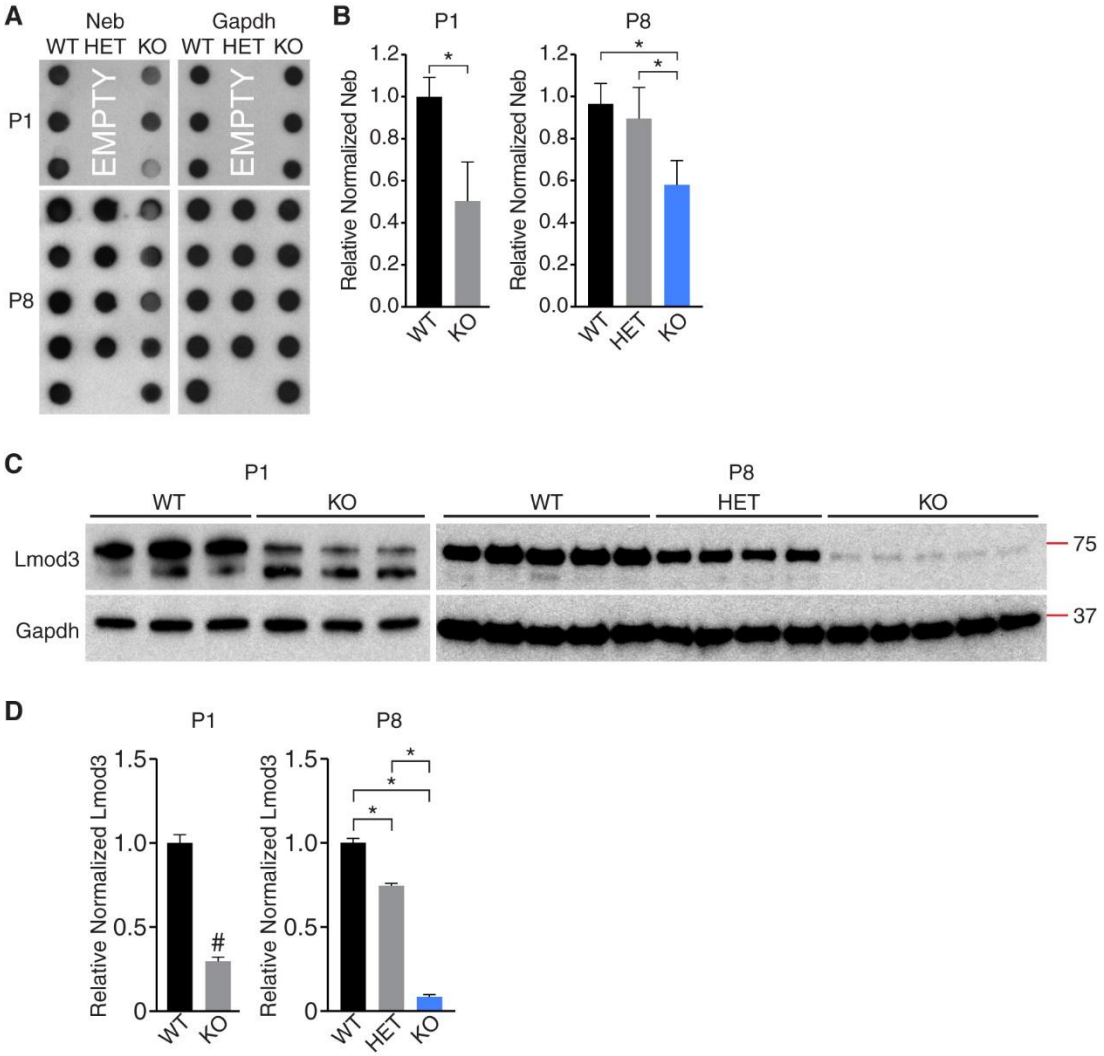

Figure 2.29. Reduced Neb and Lmod3 in Klhl40 deficient muscles. (**A**) Dot blot analysis of Neb in P1 and P8 quadriceps muscle and (**B**) corresponding densitometry. Validation of Neb dot blot can be found in Figure 2.30. (**C**) Western blot analysis of Lmod3 in P1 and P8 quadriceps muscle and (**D**) corresponding densitometry. (**A-D**) Both Neb and Lmod3 are decreased in Klhl40 KO mice compared to WT. P1: WT n=3 and KO n=3; P8: WT n=5, HET n=4, and KO n=5. * statistically significant with FDR of 0.05. # $p<0.05$. Data are presented as mean ± SEM.

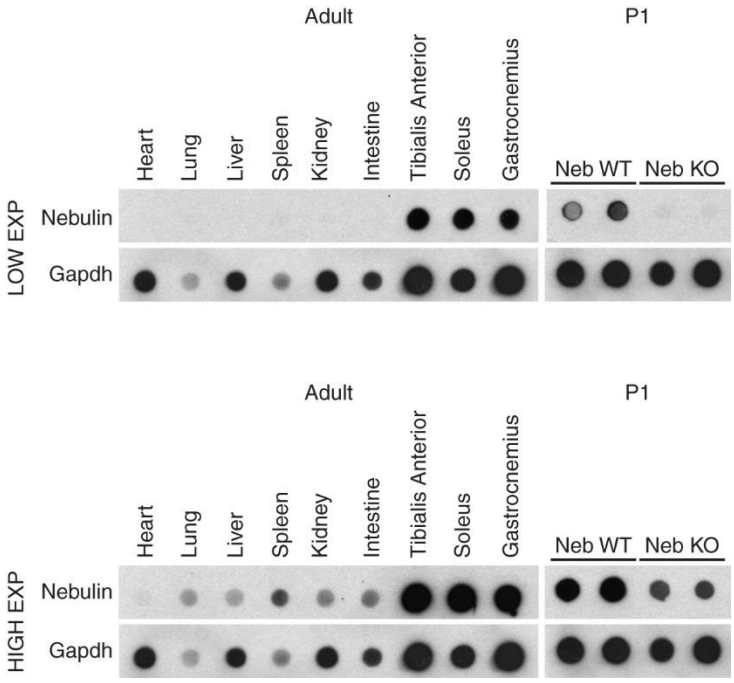

Figure 2.30. Validation of nebulin antibody by dot blotting. Analysis of nebulin (Neb) signal in multiple adult tissues and skeletal muscle from P1 *Neb*$^{+/+}$ and *Neb*$^{-/-}$ mice [from (41)] shows that signal is specific to Neb in skeletal muscle. However, upon high exposure, some non-specific signal is apparent. Gapdh serves as a loading control.

Notably, the changes in Neb and Lmod3 protein do not correlate with *Neb* and *Lmod3* mRNA transcripts (Figure 2.31, A-C).

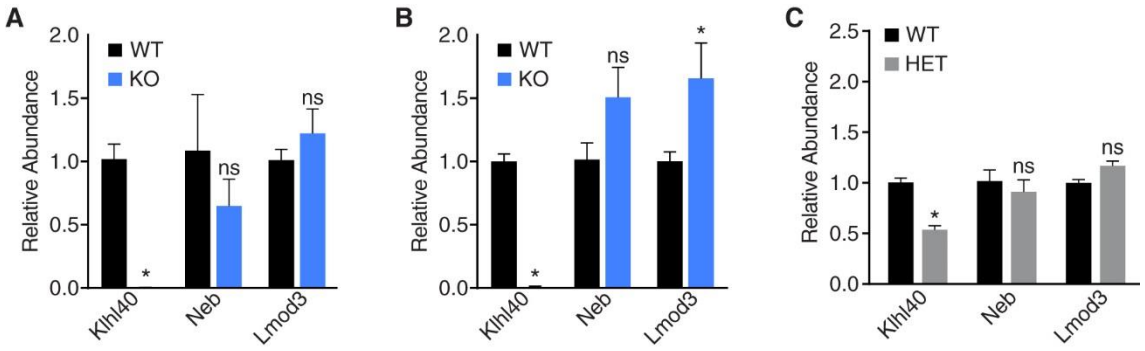

Figure 2.31. *Neb* and *Lmod3* are not decreased in Klhl40 KO quadriceps. (**A-C**) qPCR analysis of *Klhl40*, nebulin (*Neb)*, and *Lmod3* in quadriceps of (**A**) P1 and (**B**) and (**C**) P8 Klhl40 WT, HET, and KO mice as indicated. *Klhl40* is undetectable in KO mice and decreased by 50% in HET mice. *Neb* and *Lmod3* are not decreased for any genotype at any of the indicated ages. For (**A**) n=4, for (**B**), n=3, and for (**C**) n=4 for each indicated genotype in each panel. All values are normalized to 18S. * statistically significant difference with a false discovery rate (FDR) of 0.05. Data are presented as mean ± SEM.

Loss of Neb has been shown to result in shorter thin filament lengths, but Klhl40 KO mice did not have shortened thin filaments like *Neb*$^{-/-}$ mice (Figure 2.32) (41, 47, 48). Therefore, the underlying mechanical defects in muscle contraction may be occurring due to another reason than shortened thin filament lengths which is expounded upon further in the "Discussion" section of this chapter.

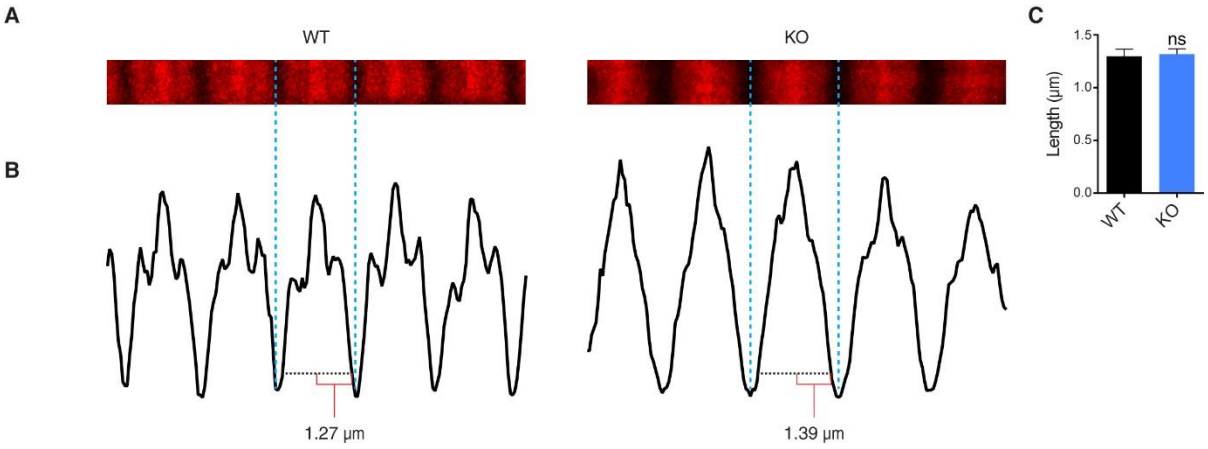

Figure 2.32. Sarcomere thin filament lengths are not decreased in Klhl40 KO mice. (**A**) Representative image of thin filament arrays labeled with phalloidin from stretched tibialis anterior muscles from P5 WT and KO mice. (**B**) Corresponding line scan analysis of previous thin filament arrays showing measurement of thin filament lengths. It is unknown why WT muscles had increased intensities near the pointed end of actin filaments. (**C**) Summary of thin filament length measurements show no difference between WT and KO muscles. N=32 sarcomeres for WT arrays and N=26 sarcomeres for KO arrays. Sarcomere measurements were done from 6 independent arrays (each from a different myofiber) combined from two separate mice for each genotype (3 arrays per mouse). Data are presented as mean ± SEM.

Using quantitative mass spectrometry, we found that Neb and Lmod3 were amongst the most decreased proteins with Lmod3 being the most down-regulated in the entire muscle proteome (Figure 2.33A). Mass spectrometric analysis of the quantitative proteomics were performed by our collaborators Lin Li and She Chen at the National Institute of Biological Sciences in Beijing, China. Of all proteins down-regulated by greater than 1.5 fold, only Lmod3 and Neb were found to be binding partners by either of our non-biased Klhl40 binding assays

(data not shown; electronic table available upon request). Notably, no decrease was seen in *Neb* or *Lmod3* mRNA transcript (Figure 2.33B).

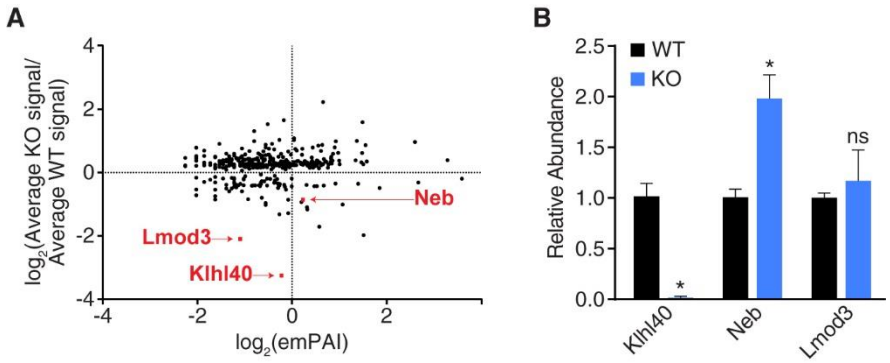

Figure 2.33. Neb and Lmod3 are of the most down-regulated proteins in the Klhl40 KO muscle proteome. (**A**) Quantitative proteomic analysis of relative protein changes between P6 WT (n=3) and KO (n=3) whole skeletal muscle shows that Lmod3 and Neb are two of the most down-regulated proteins. Data are arbitrarily stratified by the exponentially modified protein abundance index (emPAI) to allow for better resolution of individual data points. Only proteins with significant (P<0.05) changes between WT and KO mice are shown. Values for each point are shown as well as raw mass spectrometry data are available electronically upon request. (**B**) qPCR analysis of P6 quadriceps for *Klhl40*, *Neb*, and *Lmod3*, shows no decrease in *Neb* and *Lmod3* transcripts. All values are normalized to 18S rRNA. * statistically significant difference with a false discovery rate (FDR) of 0.05. Data are presented as mean ± SEM.

Lmod3 is enriched in skeletal muscle and localizes to the sarcomere A-band.

Neb is a thin filament protein frequently associated with nemaline myopathy (31), but Lmod3 is a novel protein of unknown function. Lmod3 is highly homologous to Lmod2, an essential regulator of thin filament actin organization in cardiomyocytes, suggesting that both proteins share similar function (32). We found that Lmod3, like Lmod2, localizes to the A-band (Figure 2.34, A and B). Klhl40 also localizes to the A-band (Figure 2.10B), suggesting that Lmod3 and Klhl40 co-localize.

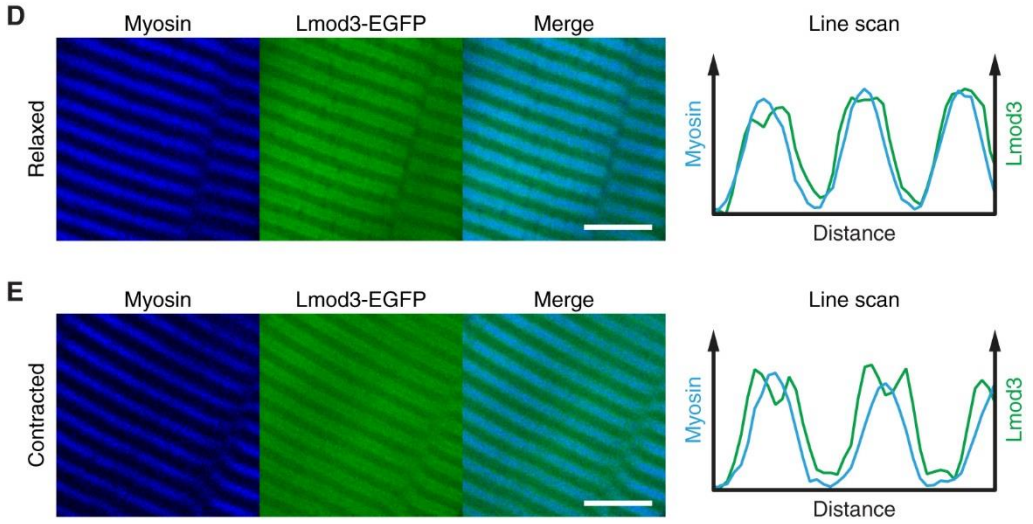

Figure 2.34. Lmod3 localizes to the sarcomere A-band. (**A**, **B**) Lmod3-EGFP localization relative to myosin in (**A**) relaxed muscles and (**B**) contracted muscles shows that Lmod3 resides in the sarcomere A-band. Scale bar: 5μm.

Interestingly, both *Lmod2* and *Lmod3* expression are restricted to striated muscle. *Lmod2* is relatively more enriched in the heart compared to skeletal muscle while *Lmod3* is expressed higher in skeletal muscle compared to heart (Figure 2.35). The expression and localization data suggest that Lmod3 could function similarly to Lmod2, but perhaps specifically for skeletal muscle.

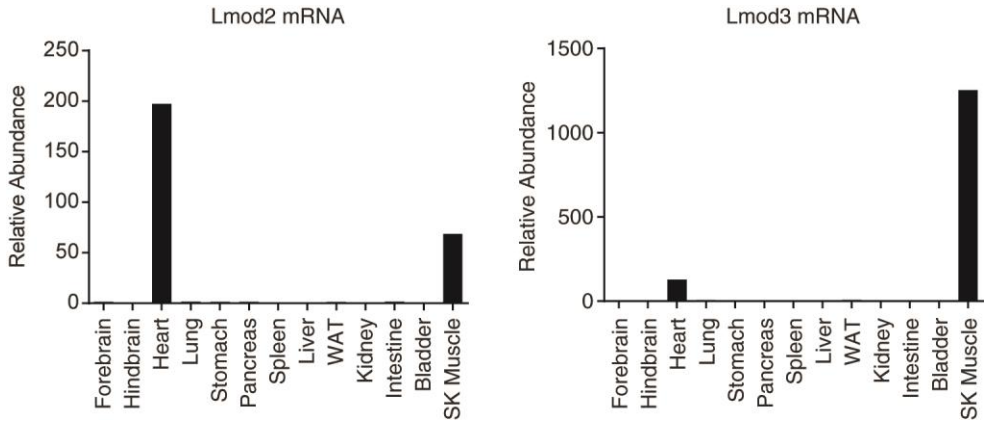

Figure 2.35. Striated muscle specificity of *Lmod2* and *Lmod3*. qPCR analysis was performed using primers specific for *Lmod2* and *Lmod3* transcripts on the indicated adult mouse tissues. Signal only appears in striated muscle for both transcripts, but in a reciprocal manner. All values are normalized to 18S rRNA. SK mscle, skeletal muscle; WAT, white adipose tissue.

Some patients with severe nemaline myopathy and KLHL40 deficiency have decreased LMOD3 and NEB.

We analyzed LMOD3 and NEB in three different patients with three different sets of mutations in the *Klhl40* locus (Figure 2.36A). Patient 1 was a compound heterozygote for two missense mutations: R311L and T506P. Patient 2 was homozygous for a W90* nonsense mutation while Patient 3 was homozygous for an E528K missense mutation. Patients with the same mutation as Patient 3 have a less clinically severe outcome than observed with other mutations of KLHL40 (17). Accordingly, the skeletal muscle biopsies showed that muscle pathology was more severe in Patients 1 and 2 than in Patient 3 (Figure 2.36B). Patients 1, 2, and 3 all had profoundly reduced KLHL40, however Patient 3 showed residual KLHL40. LMOD3 and NEB were dramatically reduced in Patients 1 and 2 while LMOD3 protein remained relatively unchanged in Patient 3 when compared to age-appropriate controls (Control 1 for Patients 1 and 2 and Control 2 for Patient 3) (Figure 2.36, C and D). NEB

reduction in Patient 3 was inconclusive due to issues with GAPDH signal for Patient 3 and Control 2. Given that Patient 3 had some residual KLHL40 and less severe muscle pathology, our findings in mice that Klhl40 serves to stabilize Neb and Lmod3 are largely consistent in KLHL40 deficient patients, although there may be some mechanistic differences based on the type of *KLHL40* mutation.

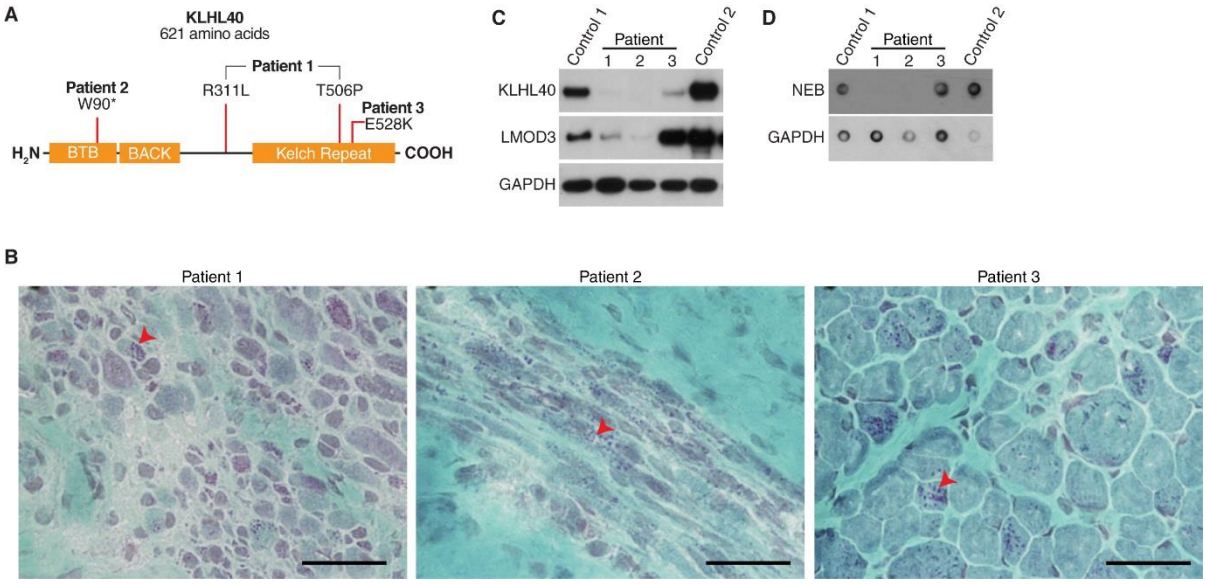

Figure 2.36 Analyzing LMOD3 and NEB expression in KLHL40 deficient patients. (**A**) Relative location of KLHL40 mutations in patients analyzed in (**B-D**). Note that Patient 1 is a compound heterozygote for the indicated mutations. (**B**) Gomori trichrome stain of skeletal muscle from Patient 1, Patient 2, and Patient 3. Sections for Patient 1 and Patient 3 show transverse fibers while the section for Patient 2 shows longitudinal fibers. Red arrowheads denote the presence of nemaline bodies which appear as punctate basophilic structures. Compared to Patient 3, Patient 1 and Patient 2 display increased collagen deposition and Patient 1 shows substantial fiber size heterogeneity. Scale bars: 25µm. (**C**) Detection of LMOD3 and KLHL40 by Western blot analysis and (**D**) NEB by dot blot analysis, in control and KLHL40 deficient patient skeletal muscle biopsies. Patients 1 and 2 have a clear decrease in LMOD3 and NEB compared to age-matched control, Control 1. Patient 3 compared to age-matched control, Control 2, does not have decreased LMOD3, but changes in NEB are inconclusive due to issues with GAPDH signal. Control 1 and Control 2 are 11 day and 6 month old neonate controls, respectively. Patient 1 was biopsied at 2 days, Patient 2 was biopsied at 25 days, and Patient 3 was biopsied at 3 months of age. GAPDH is shown for loading control.

DISCUSSION

KLHL40 mutations have recently been shown to cause nemaline myopathy in humans but the underlying pathogenic mechanisms have not been defined. The results of this study demonstrate that Klhl40 is essential for the maintenance of sarcomere structure and muscle contractility. Loss of Klhl40 in mice leads to a nemaline myopathy-like phenotype comparable to that of nemaline myopathy patients lacking KLHL40 (17). We find that Klhl40 localizes to the I-band and A-band of sarcomeres, and binds to two proteins located in these bands, Neb and Lmod3. Unlike previously described BBK proteins, we show that Klhl40 promotes the stability of Neb and Lmod3, providing a possible molecular explanation for nemaline myopathy in KLHL40 deficient patients. Consistent with these findings, Neb and Lmod3 protein levels are specifically diminished in Klhl40 deficient mice and KLHL40 deficient patients, suggesting the involvement of KLHL40 in nemaline myopathy and regulation of sarcomere structure. We propose that Klhl40 promotes Neb and Lmod3 levels and that loss of Klhl40 primarily reduces Neb and Lmod3. This results in thin filament disruption with subsequent irregularities of sarcomere Z-discs and, in extreme cases, sarcomere dissolution with the formation of ovoid Z-discs, culminating in a fatal loss of muscle function (Figure 2.37).

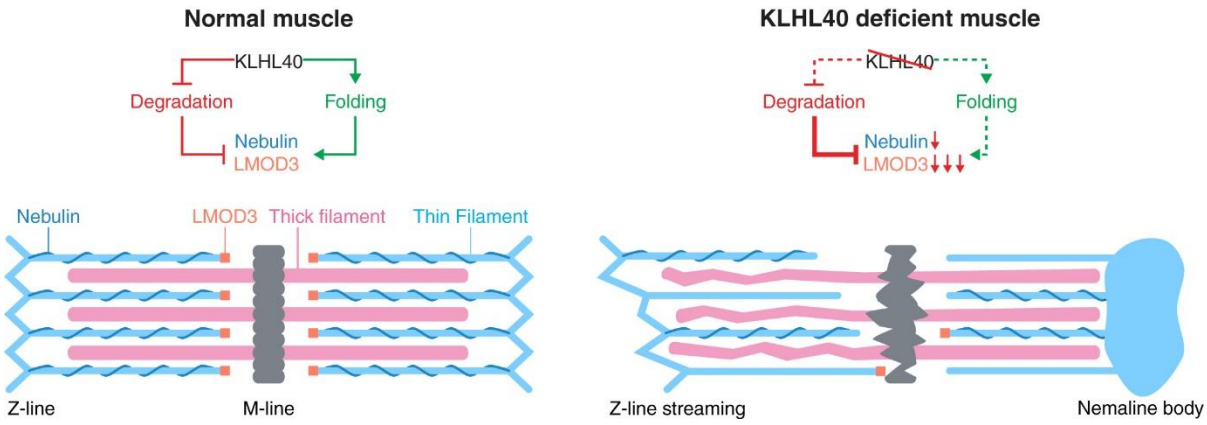

Figure 2.37 Proposed mechanism of nemaline myopathy KLHL40 deficient patients. Under normal conditions (left) KLHL40 either blocks the degradation or promotes successful folding of NEB and LMOD3 which function to stabilize the thin filament allowing normal sarcomere function. In muscles lacking KLHL40 (right) NEB and LMOD3 protein levels are reduced, resulting in destabilization of thin filaments, sarcomere dysfunction, and subsequent nemaline myopathy.

Nemaline myopathy-like disease due to loss of Klhl40.

Similar to human patients that lack KLHL40, Klhl40 KO mice display neonatal lethality with defects in sarcomere structure and significant muscle weakness (17). Cardiac defects are not a typical feature of nemaline myopathy, and, although *Klhl40* has some expression in the heart, we observed no cardiac hypertrophy, dilation, nor any loss in cardiac contractility in Klhl40 KO mice (31, 42).

Unlike patient biopsies, classic nemaline bodies are not readily apparent in the Klhl40 KO mice except in highly disorganized fibers where they present as widened Z-discs. The more prevalent defect seen in mice is the presence of Z-line streaming which is indicative of sarcomere damage and is often seen in combination with nemaline bodies in patient biopsies (7, 49). The lack of *bona fide* nemaline bodies in other KO mouse models of nemaline myopathy is not uncommon. Deletion of Acta1 and Neb in mice, the two most frequently

implicated proteins in nemaline myopathy (31), results in neonatal lethality and muscle dysfunction, but classical nemaline bodies are not reported (41, 47, 48, 50). Currently, nemaline bodies are only reproduced in mouse models of nemaline myopathy overexpressing mutant protein, suggesting that mutant proteins are required for protein aggregation to form rods (51-53). A previous study noted that the presence of nemaline bodies does not correlate with the severity of the disease (19). Instead, it is believed that decreased contractility due to primary defects in the sarcomere thin filament is the underlying cause for symptoms in nemaline myopathy (20). This hypothesis is supported by studies with P1 Neb deficient mice which have a dramatic loss in muscle contractility with no visible sarcomere defects (41, 54). Accordingly, we too find that sarcomeres in P1 Klhl40 WT and KO mice appear comparable, but there is still a greater than 50% loss of maximum tetanic force in KO muscle. Our data, combined with previous studies, corroborate the hypothesis that nemaline myopathy is likely due to sarcomere dysfunction and instability, causing a primary loss in muscle contractility (19, 41, 47, 48, 50). We believe that sarcomere instability results in the visible Z-line streaming and nemaline bodies in Klhl40 deficient mice at later ages due to increased muscle use following birth.

Klhl40 binding and regulation of thin filament proteins, Neb and Lmod3.

We demonstrate that Klhl40 localizes to the I-band and the A-band in possibly a dynamic manner in relaxed and contracted muscles, respectively. Neb is known to span the I-band and the A-band and we show that Lmod3 occupies the A-band (45). Thus, Klhl40 occupies the same subcellular compartments as Neb and Lmod3.

In contrast to all other described BBK proteins, we demonstrate that Klhl40 actually stabilizes, rather than degrades, its substrates (22-29). Neb_{frag} and Lmod3 are increased in

cell culture with Klhl40 expression, and loss of Klhl40 in mice results in reduced Neb and Lmod3 independent of any transcriptional changes. In addition, Klhl40 appears to block Lmod3 ubiquitination whereas Klhl40 regulates Neb_{frag} in a proteasome-independent manner. These findings provide the first example of a BBK protein that can mediate protein stabilization rather than degradation. However, the exact mechanism by which this stabilization occurs remains unclear. With regard to Lmod3, preventing ubiquitination of a protein can occur due to more indirect reasons. For example, if Klhl40 serves as an anchor for Lmod3 to actin thin filaments and prevents it from mislocalizing, this in itself could prevent Lmod3's ubiquitination. A more direct experiment to test if Klhl40 directly prevents ubiquitination of Lmod3 would be to identify the E3 ligase that ubiquitinates Lmod3, and then perform an *in vitro* ubiquitination assay in the presence and absence of Klhl40.

Another point of contention is why Neb_{frag} is not regulated by the proteasome like Lmod3. The two major protein degradation pathways are the ubiquitin proteasome system and the lysosome (55). It is possible that, in the absence of Klhl40, Neb_{frag} accumulates and is shuttled to the lysosome for degradation. To test this possibility, it would be worthwhile to use lysosomal inhibitors to see if Neb_{frag} protein levels can be increased in the absence of Klhl40. Additionally, these experiments were done with a fragment of Neb in the non-muscle COS7 cell line (43, 44). An informative proteasome inhibition experiment would be to generate a C2C12 knockout cell line and treat those cells with proteasome inhibitor to test if Neb and Lmod3 protein can be rescued in the absence of Klhl40.

Previous studies showed that the KR domain in BBK proteins is required for binding of substrate to its respective BBK protein (27-29). Accordingly, deletion of the Klhl40 KR domain abrogates stabilization of Lmod3 and Neb_{frag} in cell culture. Deletion of the BTB or

BACK domains of Klhl40 has no effect on Lmod3 stabilization, but Neb_{frag} levels are reduced, again, implying alternative mechanisms for Klhl40 regulation of Neb_{frag}.

BBK proteins typically bind the Cul3-E3 ligase complex to mediate substrate recognition for ubiquitination, and a recent report suggests that Klhl40 may bind Cul3 based on overexpression of epitope tagged Klhl40 and Cul3 in 293T cells (22-29, 56). It is possible that Klhl40 directly prevents Cul3-mediated degradation of Lmod3 perhaps by preventing recognition of Lmod3 by the Cul3-E3 complex. However, the BTB domain has been shown to be important for Cul3 binding, but the deletion of the BTB domain does not affect Lmod3 stabilization (27-29, 57). On the other hand, stabilization of Neb is influenced by the presence of the BTB domain, but Neb protein is not influenced by the proteasome, at least in cell culture. Lastly, endogenous Cul3 was not identified as a binding partner by either our Klhl40 TAP from C2C12 cells, which brings into question whether the reported binding of Klhl40 to Cul3 is functional.

An alternative mechanism, based on Klhl40's putative dynamic localization in relaxed and contracted muscles, Klhl40 may have a more chaperone-like function to maintain proper Lmod3 and Neb folding throughout muscle contraction which secondarily prevents their degradation. Further studies will be needed to understand this novel pro-stability function of Klhl40 and to determine whether other BBK proteins may have a similar function.

Effect of decreased Neb and Lmod3 in nemaline myopathy phenotype.

Whole-proteome analysis of Klhl40 KO muscle revealed that Neb and Lmod3 were among the most down-regulated proteins and were the only identified binding partners to show such dramatic regulation. Lmod3 was the most reduced protein in the entire muscle proteome. In fact, even 50% reduction of *Klhl40* transcript in mice lacking a single copy of the Klhl40

gene was sufficient to reduce Lmod3, suggesting a tight dose-dependence of Lmod3 on Klhl40 protein levels.

Previous work has definitively shown that mutations in *NEB* in patients and loss of *Neb* in mice results in nemaline myopathy, suggesting that decreased Neb in Klhl40 KO mice could contribute to the nemaline myopathy phenotype (11, 31, 41, 47, 48). A pervading belief is that Neb regulates thin filament lengths based on shortened thin filament lengths seen in *Neb* deficient mice (41, 47, 58). However, more recent studies argue that Neb deficiency directly contributes to a loss in muscle contractility due to dysregulation of actin-myosin cross-bridge formation (54, 58, 59). Accordingly, we see over a 50% loss in hind limb strength of P1 Klhl40 KO mice, which have a ~50% reduction in Neb, without any evidence of sarcomere defects. It is possible that loss of Klhl40 functionally impairs the actin-myosin cross-bridge activity of Neb.

Lmod3 function has hitherto not been defined nor has it been implicated in any disease. Our study presents the first evidence of a possible role of Lmod3 in nemaline myopathy. Lmod3 is highly homologous to Lmod2, which was previously shown to be vital for sarcomere structure in cardiomyocytes by regulating actin assembly at the pointed end of thin filaments (near the sarcomere M-line) (32). Indeed, we find that Lmod3 localizes to the edges of the A-band similar to Lmod2, likely indicating that Lmod3 also binds the pointed end of actin filaments. Thus, loss of Lmod3, secondary to Klhl40 deficiency, may lead to thin filament actin dysregulation. In the following chapter, we will describe the degenerative muscle phenotype of Lmod3 knockout mice.

Role of BBK proteins in human nemaline myopathy.

Thus far, three BBK proteins have been implicated in nemaline myopathy: KBTBD13, KLHL40, and KLHL41 (16-18). Our study is the first to define a possible molecular mechanism for any of these proteins. Consistent with the phenotype of Klhl40 mutant mice, the two nemaline myopathy patients (Patients 1 [heterozygous for R311 and T506P] and 2 [homozygous for W90*]) completely deficient for KLHL40 had marked reduction in LMOD3 and NEB, while a third patient (Patient 3 [homozygous for E528K]) with some residual KLHL40 had relatively normal LMOD3. Patients with the same mutation as Patient 3 present with less severe clinical symptoms compared to all other KLHL40 mutations (17). Thus, our finding that Klhl40 serves to stabilize Lmod3 in mice is largely consistent in KLHL40 deficient patients, although there may be some mechanistic differences based on the type of KLHL40 mutation. Regardless, these findings may have important therapeutic implications for KLHL40 deficient patients (see below).

A recent report described *KLHL41* mutations causing nemaline myopathy in humans (18). KLHL41 is the most closely related protein to KLHL40 (71% by BLASTP alignment) (18, 57, 60, 61). Interestingly, we found that Klhl41 was the most enriched Klhl40 binding partner from C2C12 myotubes. As determined by quantitative proteomics, Klhl41 levels in Klhl40 deficient mice were not changed, suggesting that Klhl40 does not regulate protein levels of Klhl41. We hypothesize that KLHL40 and KLHL41 may form a heterodimer to regulate thin filament proteins with both KLHL40 and KLHL41 performing unique, non-redundant functions, possibly explaining why a disruption in either protein results in nemaline myopathy. It is also tempting to speculate that KLHL41, like KLHL40, promotes the stability of its substrates based on their close homology. On the other hand, KBTBD13 is much more distantly related to KLHL40 and KLHL41, and *KBTBD13* mutations resulting in nemaline myopathy are

autosomal dominant in contrast to the autosomal recessive transmission of *KLHL40* and *KLHL41*-related nemaline myopathy (57). Thus, the molecular mechanism underlying KBTBD13 nemaline myopathy is likely different than that of KLHL40 and KLHL41.

Therapeutic implications.

There are currently no therapies available to treat nemaline myopathy. However, our data suggest that KLHL40 deficiency results in nemaline myopathy by secondary loss of Neb and Lmod3 protein, and that proteasome inhibition may be sufficient to restore Lmod3. Should Lmod3 be determined to be a major contributor to the nemaline myopathy phenotype seen with Klhl40 deficiency, it would be worthwhile to explore whether proteasome inhibition can alleviate muscle dysfunction in KLHL40 deficient patients. Proteasome inhibitors have already been used in cancer therapy and are thus available for clinical use (30). We attempted delivery of the proteasome inhibitor, MG132 into WT and Klhl40 KO neonates, but we could not find any evidence that MG132 inhibitor was active in Klhl40 KO muscles. For both genotypes, we injected MG132 and then harvested muscles following about a week of daily injections. To test for proteasome inhibition in muscles, we looked at global levels of ubiquitinated proteins. In WT mice, we saw an increase in ubiquitinated proteins indicating proteasome inhibition (data not shown), but we saw no such result in Klhl40 KO mice. Clearly, the emaciation of Klhl40 KO mice causes a change in the pharmacodynamics and/or pharmacokinetic handling of MG132. A more in-depth drug study will be required to find a working proteasome inhibitor for Klhl40 KO mice. Regardless, further delineation of the molecular mechanism by which KLHL40 promotes Neb and Lmod3 stability may allow for the development of an effective therapy for nemaline myopathy.

METHODS

Generation of Klhl40$^{+/-}$ *and* MCK-Klhl40 *mice*

To generate Klhl40 deficient mice, two embryonic stem cell targeting *Klhl40*, 14780A-A4 and 14780A-B6, were obtained from the KOMP Repository (http://www.KOMP.org) which were generated by Regeneron Pharmaceuticals clones on a C57BL6/N background (62). The targeting strategy is shown in Figure 2.4. Both clones were injected into albino 3.5-day-old C57BL/6 blastocysts by the Transgenic Core Facility at University of Texas Southwestern Medical Center and subsequently implanted into albino C57BL/6 mothers. Chimerism of each obtained founder was determined based on the estimated percent contribution of black coat color. High percentage chimeras were bred to albino C57BL/6 females and germline transmission was initially determined by black coat color and then confirmed by PCR amplification of a portion of the β-galactosidase cassette using the following primers: F – ttatcgatgagcgtggtggttatgc, R – gcgcgtacatcgggcaaataatatc. *Klhl40*$^{+/-}$ mice were intercrossed to generate *Klhl40*$^{-/-}$ mice and maintained in a pure C57BL/6 background. *Klhl40* genotypes were determined based on the presence or absence of the targeted allele by amplifying the β-galactosidase cassette using the aforementioned primers and based on the presence or absence of the wild type allele using the following primer set: F – aggggttgggggcagagaca, R – agctgcccctctcctcctcc. Thus, a mouse that lacked the targeted allele, but had the WT allele was considered to be *Klhl40*$^{+/+}$ (WT); a mouse that had both the targeted allele and the WT allele was considered to be *Klhl40*$^{+/-}$ (HET); a mouse that had the targeted allele, but lacked the WT allele was considered to be *Klhl40*$^{-/-}$ (KO).

MCK-Klhl40 mice were generated as previously described (63). Briefly, the *Klhl40* containing its endogenous Kozak sequence and stop codon (NCBI reference sequence

NM_028202.3, nucleotides 150-2036) cloned into a previously generated MCK vector (64) downstream from the 4.8-kb muscle creatine kinase (MCK) promoter and upstream of a human growth hormone poly(A) signal (HGH). Then, the MCK vector containing *Klhl40* (MCK-Klhl40) was digested and the fragment containing the promoter, *Klhl40* cDNA, and HGH, was purified and eluted into oocyte injection buffer (5 mM Tris-HCl [pH 7.4] and 0.2 mM EDTA). The purified DNA was subsequently injected into fertilized oocytes derived from B6C3F1 mice and then transferred to the oviducts of pseudopregnant ICR mice. Presence of the *MCK-Klhl40* transgene was determined by genotyping using the previously mentioned qPCR primers for *Klhl40* expression analysis. Only a single surviving founder with the transgene was obtained and subsequently crossed with *Klhl40*$^{+/-}$ creating a mixed C57BL6 and B6C3F1 line. *MCK-Klhl40; Klhl40*$^{+/-}$ mice were crossed with *Klhl40*$^{+/-}$ mice to generate WT (*Klhl40*$^{+/-}$), WT Tg (*MCK-Klhl40; Klhl40*$^{+/+}$), KO (*Klhl40*$^{-/-}$), and KO Tg (*MCK-Klhl40; Klhl40*$^{-/-}$) mice used for subsequent analysis. All analyses of masses were done within the same mixed line using littermates as controls.

Neonatal muscle contraction.

P1 pups were placed in a weigh boat on wet ice for 15 minutes followed by decapitation with scissors precleaned with 70% ethanol. After euthanasia, hind limbs were cleaned of skin. Non-absorbable braided silk suture (6-0) was tied proximal to the knee and the intact hind limb was severed at the hip. The preparations were placed in an incubated 30^0C oxygenated (95% O_2, 5% CO_2) physiological salt solution (PSS) (65). The foot was placed in a clamp at the base of the bath and the suture tied to arm of a dual-mode servomotor system (300B, Aurora Scientific, Inc). Resting tension was maintained by a stepper motor (65). Data were

obtained and analyzed with Dynamic Muscle Control (DMC v.4.1.6,), and Dynamic Muscle Analysis (DMA v.3.2) software, respectively (Aurora Scientific, Inc.)

Optimal conditions for activation of the hind limb muscles were determined on the first 4 preparations as follows: twitch responses were elicited to determine the optimal resting tension (i.e., optimal length) (0.25, 0.50, 0.75, and 1.0g); the optimal voltage (15, 20, 25, 30, 35, 40V) and the optimal pulse width (250, 500, 750ms). Optimal values used thereafter were 0.5g, 30V, and 500ms, respectively. Following initial twitch and tetanic contractions, a force-frequency relationship was determined at 1, 30, 50, 80, 100, and 150Hz. Data are reported only for 150Hz contractions as normalized stress (mN/mg limb mass). Experiments were done double-blinded with genotyping being performed following acquisition of data.

Protein localization by electroporation of FDB muscles and second harmonic generation.

Klhl40-EGFP, Lmod3-EGFP, Actn1a-EGFP, and Tmod4-EGFP were electroporated into the FDB muscles of adult ICR mice and localized to myosin by 2HG as previously described with some modifications (37, 66). See cloning section for additional details for creation of aforementioned constructs. Mice were sacrificed by CO_2 asphixyation and then skinned from their midsections to their feet. Care was taken when skinning on the plantar side of the foot to prevent damage to the flexor digitorum brevis. Skinned feet from mice immersed in either an ice-cold, calcium-free EDTA-Ringer's solution (100mM NaCl, 2mM KCl, 2mM $MgCl_2$, 6mM KH_2PO_4, 1mM EDTA, and 0.1% glucose) to relax muscle or in an ice-cold rigor buffer (100mM KCl, 2mM $MgCl_2$, 1mM EDTA, and 10mM KH_2PO_4) to cause a sustained muscle contraction (38). Feet were left in buffer for at least two hours, and then imaged as described previously with a Zeiss LSM 780 confocal/multiphoton microscope. If imaging was

done before allowing adequate time for feet to soak in rigor buffer, GFP signal appeared diffuse throughout the fiber. It should be noted that the limiting factor for this method is finding fibers with adequate myosin signal which also express acceptable levels of the GFP tagged construct. Line scan analyses were done using Fiji ImageJ software (67).

Echocardiography studies.

Echocardiography was performed on P5 neonates using the Vevo 2100 small animal echocardiography system (VisualSonics) and a 40-MHz transducer. Pups were kept on a heating pad before and after the procedure to avoid a vagal response. Conscious pups were gently restrained and the ultrasound probe positioned to obtain a parasternal short-axis view. The largest anteroposterior diameters in diastole and systole were assessed in at least three recorded M-mode tracings and LV fractional shortening calculated according to the formula FS(%) = [(LVIDd – LVIDs)/LVIDd] × 100. Heart rate was assessed to exclude a vagal response. Data were analyzed by a single observer.

Radioactive* in situ *hybridization.

Radioisotopic *in situ* hybridization on embryonic section was performed as previously described (68). The probe used to track *Klhl40* expression contained the full-length *Klhl40* CDS (NCBI reference sequence NM_028202.3, nucleotides 170-2036). ^{35}S-UTP labeled antisense and sense probes were generated by SP6 and T7-mediated *in vitro* transcription, respectively, using the Maxscript kit (Ambion).

Northern blot analysis.

A pre-made adult mouse multi-tissue Northern blot was purchased from Zyagen (MN-MT-1) and then was analyzed as previously described (69). Briefly, the blot was incubated in hybridization buffer (1% crystalline BSA (fraction V), 1 mM EDTA, 0.5 M $NaHPO_4$, 7% SDS) for at least 2 h at 68 °C. *Klhl40* probe was generated by labelling a 802nt fragment that spanned nt 400-1201 of *Klhl40* mRNA (NCBI reference sequence NM_028202.3) with [α-^{32}P]dCTP using the RadPrime DNA Labelling System (Invitrogen). Radioactive probe was hybridized to the blot overnight at 68C. After overnight incubation, the blot was washed with 1× SSC, 0.1% SDS for 10 min at room temperature followed by three washes at 68°C with 0.5× SSC, 0.1% SDS. The membrane was exposed to film at −80 °C overnight and developed with a SRX101A Tabletop X-Ray Film Processor (Konica Minolta). For *Gapdh* loading control, the blot was used without stripping and incubated with *Gapdh* probe generated from full-length *Gapdh* cDNA using the all the same steps as mentioned above. However, *Gapdh* blots were only exposed for 2 hours at -80C before processing.

qPCR analysis.

Total RNA was extracted from either mouse tissue or cultured cells with TRIZOL (Invitrogen) according to manufacturer instructions. cDNA was synthesized using Superscript III reverse transcriptase with random hexamer primers (Invitrogen). Gene expression was analyzed by qPCR using either Power SYBR Green or Taqman Master Mix (Life Tecnologies) or KAPA SYBR FAST (Kapa Biosystems). The following primers (in order of appearance) were used for SYBR analysis:

Klhl40 – F: cccaagaaccatgtcagtctggtgac, R: tcagagtccaagtggtcaaactgcag;

Lmod2 – F: ttggagaaggaacggctggg R: cctcagagacttcgctgttgctctc,

Lmod3 (used to analyzed *Lmod3-myc* as well) – F: ccgctggtggaaatcactccc, R: actccagctcctttggcagttgc;

Neb$_{frag}$*-myc* – F: ggttgctatgcctatgataccctg, R: tgcctgttaattggacagtcagcaac.

Neb was analyzed using a Taqman probe (ID: Mm01546298_1) purchased from Life Technologies. All analyses were performed on a 7900HT Fast Real-Time PCR machine (Life Technologies).

Microarray analysis.

RNA was submitted to the UT Southwestern Genomic and Microarray Core Facility for further processing and microarray analysis using a MouseWG-6 V2 BeadChip (Illumina) as previously described (70). Significant ($P<0.05$) changes in sarcomere genes are reported in Supplementary Table 1. Significance was determined by student T-test without correcting for multiple comparisons. Array data is available at NCBI's Gene Expression Omnibus (GSE56570).

C-terminal EGFP fusion of Actn1a, Tmod4, Klhl40, and Lmod3 for FDB electroporation.

To generate C-terminally fused constructs for electroporation into mouse FDB muscles, we utilized the pcDNA3-EGFP plasmid generated by Doug Gloenbock (Addgene plasmid 13031). Full coding sequences of each protein were used without stop codons. Actn1a was cloned into pcDNA3-EGFP using the KpnI/XhoI restriction enzymes, and Tmod4 and Klhl40 were cloned with EcoRI/XhoI. Lmod3 was cloned by cutting the 5' end with BamHI followed by blunting with the Klenow large fragment (NEB) according to manufacturer's

direcitons and then cut with XhoI. To ligate to Lmod3, pcDNA3-EGFP was cut with EcoRI, blunted, and then cut with XhoI.

Generating the* Klhl40 *conditional targeting vector and conditionally targeted* Klhl40 *mice.

A recombineering approach was utilized to generate the *Klhl40* conditional targeting vector to avoid the need for PCR amplification of large genomic pieces of DNA that would be prone to mutations. In this section, I will detail both the failed and successful approaches to using recombineering to generate the construct. Note that Klhl40 is sometimes referred to as "Kbtbd5", which is the original name for this protein.

Recombineering was performed according to the protocol published by Sharan *et. al.* (71), but electrocompetent bacteria were generated as described in the protocol by Carreira-Rosario *et. al.* (72). The first method attempted to generate the *Klhl40* conditional targeting vector was to retrieve a 12.6kb genomic fragment containing the *Klhl40* gene and then to insert a modified knockout first cassette generated by the Knockout Mouse Project (KOMP) which is compatible with recombineering. This method failed due to inherent toxicity of the 12.6kb DNA sequence to bacteria. It is described in detail below.

To generate the *Klhl40* conditional targeting vector by a pure recombineering approach, we chose to retrieve a 12.6kb fragment of the *Klhl40* locus in chromosome 9 (nucleotides 121773534 to 121786153 in NCBI Reference Sequence: NC_000075.6). First, to construct the retrieval vector, DTA with its PGK promoter (pgk-DTA) was cloned from the C1qtnf3 KOMP targeting vector using the following primer pair: <u>forward</u> – ctaccgggtaggggaggcgc (with added 5' KpnI site, not shown), <u>reverse</u> – gcccttaggttctttccgcctc (with added 5' XhoI site, not shown). The PCR product was ligated into the KpnI and XhoI site

of the pBluescript II SK(+) vector (pB2SKP-pgk-DTA). Next, 5' and 3' mini-arms of homology flanking the 12.6kb region to be retrieved were cloned from the bMQ302p07 BAC clone (Source Bioscience) using the following primers:

5' arm – forward: gtgtgtttgtgtcacagtgtacctgaggtggcc (with added 5' HindIII site, not shown), reverse: gcctctgcctcccaagtgctgggattaaag (with added 5' ClaI site, not shown);

3' arm – forward: tccaaggcacaagttctatcagctctgctggg (with added 5' HindIII site, not shown), reverse: tgaggggaggaatgtagggtacgaagtcaggg (with added 5' ClaI site, not shown).

The arms were then ligated into their respective sites in the pBluescript II SK(+) vector. Note that this 3' arm will also be used for generating the HhatI retrieval vector, but in the opposite orientation.

To assemble the retrieval vector, pB2SKP-pgk-DTA was cut with SalI, blunted, and then cut with ClaI. The 5' arm of homology for Klhl40 was cut with HindIII, blunted, cut with ClaI, then ligated into the cut pB2SKP-pgk-DTA vector (pB2SKP-pgk-DTA-5Kb5). Next, pB2SKP-pgk-DTA-5Kb5 was cut with HindIII and EcoRV. The 3' arm of homology was cut with ClaI, blunted, cut with HindIII, and then ligated into the cut pB2SKP-pgk-DTA-5Kb5 vector (pB2SKP-pgk-DTA-5Kb5-3Kb5). Finally, a PacI site was added into pB2SKP-pgk-DTA-5Kb5-3Kb5 in the NotI and XbaI sites by ligating in annealed oligos using the following primers (containing NotI and XbaI overhangs for ligation): forward – ctagattaattaagc, reverse – ggccgcttaattaat. This generated the final retrieval vector referred to as Kbtbd5retPacI.

To perform retrieval of the genomic fragment, Kbtbd5retPacI was linearized with HindIII and electroporated into DY380 cells containing the bMQ302P07 BAC. Bacteria were grown on LB + ampicillin plates to select for positive recombinants which were initially found by a PCR screening strategy (not shown). PCR screen positive colonies were mini-prepped, and diagnostic restriction digest with HindIII was performed on extracted DNA. HindIII

digested DNA was run on a TAE agarose gel to confirm presence of whole insert. DNA from successful recombinants were stored for later use. KbtbdretPacI with the 12.6kb fragment is referred to as Kbtbbd5ret-12.6kb-PacI.

Next, we needed to construct a knockout cassette that would add loxP sites flanking exon 2. Conditional deletion of exon 2 was predicted to result in a frameshift mutation with a subsequent premature stop codon. To accomplish this, we borrowed the knockout first strategy created by KOMP (73) (Figure 2.38A). The advantage of this strategy is that the initial targeted allele is null for the targeted gene due to insertion of a transcriptional halting poly-adenylation sequence. Before we could utilize this knockout first cassette by KOMP, we had to make it compatible with recombineering by adding a selectable antibiotic resistance marker. The KOMP knockout cassette already contained a neomycin resistance gene driven by a human β-actin promoter. By adding a bacterial promoter, we could use this resistance gene to screen for recombinants using kanamycin selection (Figure 2.38B).

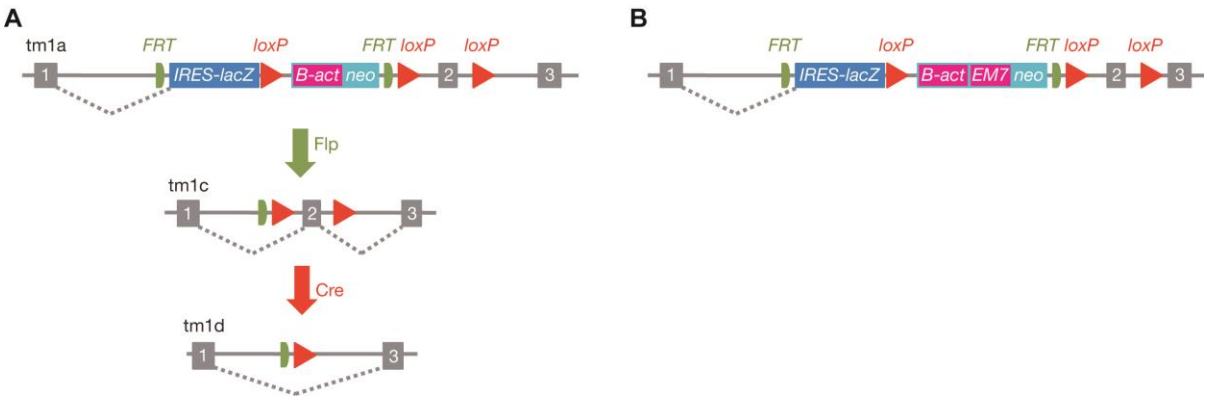

Figure 2.38. Modified KOMP knockout first strategy. (**A**) Original KOMP knockout first strategy showing targeting of a generic gene. The "knockout first allele" (tm1a) contains an *IRES-lacZ* gene that is driven by the endogenous promoter and also a transcriptional stop site. Splicing into the *IRES-lacZ* gene disrupts expression of the targeted gene. Upon FLP-mediated recombination, a conditionally targeted gene is created (tm1c). Finally, Cre-mediated recombination generates the null allele (tm1d). (**B**) Modified knock-out first allele that adds the bacterial EM7 promoter between the β-actin (*B-act*) and neomycin resistance gene (*neo*) allowing for compatibility with the recombineering strategy described. (**A**, **B**) Figures modified from (73).

To add the EM7 bacterial promoter immediately 3' to the human β-actin promoter and 5' to the neomycin resistance gene, we constructed an EM7 insert that could be recombined precisely into the aforementioned locus. The EM7 bacterial promoter was created by annealing two sets of oligos, 5' EM7 and 3' EM7 respectively. The forward and reverse oligos for **5' EM7** were:

forward–

cgatccgagaccgcgtccgccccgcgagcacagagcctcgcctttgccgatcctgttgacaattaatcatcggcatagtatatcg gcata,

reverse–

cgatatactatgccgatgattaattgtcaacaggatcggcaaaggcgaggctctgtgctcgcggggcggacgcggtctcggat.

When 5' EM7 is annealed together, it generates a ClaI overhang on its 5' end and an arbitrary "GCATA" 3' overhang on its forward strand for ligation to the 3' EM7 annealed oligo set. 5'

EM7 contained 49 nucletodies of homology to the 3' end of the human β-actin promoter and the 5' fragment of the EM7 promoter. The forward and reverse oligos for **3' EM7** were:

forward –

gtataatacgacaaggtgaggaactaaaccatgattgaacaagatggattgcacgcaggttctccggccgcttgggtggagat,

reverse –

cgatctccacccaagcggccggagaacctgcgtgcaatccatcttgttcaatcatggtttagttcctcaccttgtcgtattatactatg
c.

When annealed together, 3' EM7 has an arbitrary "CGTAT" 5' overhang on its reverse strand which allows it to anneal to the 3' end of the 5' EM7 strand. In addition, the 3' end of the reverse strand forms a ClaI overhang. Lastly, the 3' EM7 annealed oligo set contains the 3' fragment of the EM7 promoter as well as 51bp of homology to the neomycin resistance gene. The annealed 5' EM7 and 3' EM7 oligo sets were inserted into the ClaI site of pBluescript II SK(+) (pB2SKP-EM7) in a single, double-ligation step.

The assembled EM7 promoter was digested with ClaI from pB2SKP-EM7. DY380 cells containing the C1qTNF3 targeting vector were electroporated with the assembled EM7 promoter and positive recombinants were selected by plating on LB + kanamycin plates.

Next, we needed to generate the Klhl40 knockout arm which is the sequence of DNA that would be recombined following Cre-mediated recombination in our future targeted mice. The Klhl40 knockout arm containing exon 2 and fragments of intron 1 and 2, was cloned using the following primers: forward – agaagtgccaggtcaggggtgggagacagattattac (with added 5' EcoRI and BsrGI sites, not shown), reverse – tttttatctgcctaaccgagtggttataggcacaaagagcc (with added 5' XmaI site and loxP site, not shown). Next, we cloned the 5' and 3' mini homology arms for the KO cassette and inserted them into the vector containing the Klhl40 knockout arm. To clone the 5' mini homology arm we used the following primer pair:

forward – agaagtgccaggtcaggggtgggagacagattattac (with added 5' ClaI site, not shown),

reverse – tttttatctgcctaaccgagtggttataggcacaaagagcc (with added 5' EcoRI site, not shown).

To clone the 3' mini homology arm we used the following primer pair:

forward – tgggctggctcaaaggcaggagagctcag (with added 5' XmaI site, not shown),

reverse – cacctctgaagagctggtaagtcctgtgtctgtcacc (with added 5' SpeI site, not shown).

We subcloned the 5' and 3' mini homology arms into the vector containing the *Klhl40* knockout arm using ClaI/EcoRI and XmaI/SpeI, respectively. Then, we removed the KOMP knockout cassette containing the added EM7 primer by digestion with BsrGI which was subsequently ligated into the BsrGI site of the Klhl40 knockout arm. This final product is referred to as the Klhl40 KO cassette.

To insert the Klhl40 knockout cassette into Kbtbbd5ret-12.6kb-PacI, we linearized the Klhl40 KO cassette with SpeI and attempted to electroporate this DNA into DY380 cells containing Kbtbbd5ret-12.6kb-PacI. However, we found that DY380 bacteria with Kbtbbd5ret-12.6kb-PacI grew very slowly and inevitably died before we could electroporate them. Since we could not modify the retrieved fragment further, we inserted Klhl40 KO cassette directly into the bMQ302P07 BAC and then retrieve that modified fragment. However, this too failed. Lastly, we tried to electroporate SW102 cells, which are similar to DY380 cells except they are compatible with the *galK* positive/negative selection system, but these bacteria also failed to grow properly. We simply concluded that the 12.6kb fragment was toxic to bacterial strains used for recombineering.

We decided to use a hybrid recombineering approach by retrieving the homology arms of our Klhl40 conditional targeting vector, and then subcloning those arms into the PGKneoF2L2DTA conditional knockout vector generated previously (74). The 5' homology arm retrieval vector was generated by PCR SOEing together a 5' mini-arm (nucleotides

121773534 – 121774037 NCBI Reference Sequence: NC_000075.6) and a 3’ mini-arm (nucleotides 121779212 – 121779711 NCBI Reference Sequence: NC_000075.6) with an intervening ClaI site to allow for linearization between the mini-arms and 5’ and 3’ EcoRV and SalI sites, respectively, to allow for subsequent subcloning into the PGKneoF2L2DTA. The 3’ homology arm retrieval vector was generated by PCR SOEing together a 5’ mini-arm (nucleotides 121780237 – 121780682 NCBI Reference Sequence: NC_000075.6) and a 3’ mini-arm (nucleotides 121786827 – 121787244 NCBI Reference Sequence: NC_000075.6) with an intervening endogenous EagI site to allow for linearization between the mini-arms and 5’ and 3’ NotI and SacII sites. In addition, a PacI site was added adjacent to the SacII site to allow for future linearization of the targeting vector. However, retrieval of the individual 5’ and 3’ homology arms failed despite being able to retrieve the entire 12.6kb fragment.

Because we had the purified 12.6kb fragment of Klhl40, we reasoned that we should be able to PCR amplify the 5’ and 3’ homology arms with a high-fidelity polymerase, Phusion (NEB), with relative ease. We were able to PCR amplify both the 5’ and 3’ arms, but the 3’ arm contained mutations and deletions. In addition, there were some regions of the 5’ arm that could not be fully sequenced and so it was not entirely clear whether the 5’ arm was mutation-free. Instead, we decided to “repair” the 3’ arm by replacing the mutated region with the correct sequence from Kbtbbd5ret-12.6kb-PacI. In addition, we also decided to subclone the 5’ arm from Kbtbbd5ret-12.6kb-PacI, and insert it into the 5’ homology arm retrieval vector made in the previous paragraph.

First, for the 5’ homology arm, we searched for endogenous restriction sites within the 5’ retrieval vector generated previously and tried to find compatible restriction sites in the 12.6kb fragment. For the 5’ homology arm, we cut the Kbtbd5ret-12.6kb-PacI vector with HpaI and NcoI to obtain our desired band as well as PvuI to digest interfering bands. We ligated

this fragment into the previously generated 5' homology arm retrieval vector that was also cut with HpaI and NcoI.

Next, For the 3' homology arm, we had initially attempted to PCR the entire arm using Phusion polymerase (NEB) and the following primers:

forward – atgggctggctcaaaggcagg (with added SacII site followed by a PacI site, not shown),

reverse – ccaggttcgccctccagtttgg (with added NotI site, not shown).

The 3' homology arm PCR product was ligated into pBluescript II SK(+) into the respective restriction sites (referred to as Kbtbd5-3'-PCR). However, we found that the PCR product was missing a large fragment near its 5' end. Thus, we decided to "repair" this PCR product by subcloning the correct fragment from the Kbtbd5ret-12.6kb-PacI vector. We took the mutated Kbtbd5-3'-PCR vector and cut it with NheI and SphI to remove the mutated sequence and also cut with NcoI to digest interfering bands. Then, we cut Kbtbd5ret-12.6kb-PacI with NheI and SphI to cut out the unmutated sequence and cut with DraI as well to eliminate interfering bands. The NheI/SphI fragment from Kbtbd5ret-12.6kb-PacI was ligated into the NheI and SphI sites of the Kbtbd5-3'-PCR vector. This generated our final plasmid with the intact 3' homology arm.

To construct the targeting vector, we ligated in the Klhl40 knockout arm (discussed earlier) into the XmaI site of the PGKneoF2L2DTA vector (PGKneoF2L2DTA-Kb5KO). The knockout arm also contained an added NdeI site to allow for Southern screening. Then, we ligated the 5' arm into the EcoRV and SalI site of PGKneoF2L2DTA-Kb5KO by cutting out the 5' homology arm from its respective vector with EcoRV and SalI as well as PvuI to digest interfering bands (PGKneoF2L2DTA-5Kb5KO). Finally, we subcloned the 3' homology arm into the NotI and SacII site of PGKneoF2L2DTA-5kb5KO by cutting out the 3' homology arm

from its respective vector with NotI-HF and SacII as well as DraI to digest interfering bands. This generated our final PGKneoF2L2DTA-Kbtbd5 targeting vector (see Figure 2.21).

After generating our targeting vector, we attempted to linearize it for electroporation by digesting 100µg of the vector with PacI. DNA was phenol-chloroform extracted to remove restriction enzyme, precipitated in ethanol, and then resuspended in sterile TE buffer. 1µg of cut DNA was run on a 0.5% TAE gel to visualize cutting. However, instead of getting a single band as expected, we obtained a lower molecular weight band above 10kb. Initially, it was thought that this band was uncut DNA, but longer digestions with great amounts of enzyme did not eliminate this band. We re-transformed the PGKneoF2L2DTA-Kbtbd5 vector in limiting concentrations into bacteria and grew them at 32°C instead of 37°C. Minipreps were generated from colonies grown at 32°C which were subsequently digested with XhoI (another enzyme that makes a single cut in the targeting vector) and run on a 0.5% TAE gel. Compared to DNA from bacteria grown at 37°C, bacteria grown at 32°C contained only a single band. We believe that the bacteria grown at 37°C underwent some degree of homologous recombination which deleted out a fragment of the targeting vector thus generating a lower band on the 0.5% TAE gel.

Linearized PGKneoF2L2DTA-Kbtbd5 was given for electroporation into 129SvEvAB2.2 ES cells which were subsequently screened by Southern blot analysis. Approximately 10% recombination was observed. 1A2 and 1C1 targeted ES cell clones were electroporated with Cre recombinase to check for proper functioning of loxP sites. Finally, 1A2 and 1C1 were submitted for injection into 3.5 day old C57BL/6 blastocysts by the UTSW Transgenic Core. High percentage male chimeras were bred to C57BL/6 females. Mice with brown coat color were genotyped to check for the presence of the lone loxP site at the 3’ end of exon 2. However, after approximately a hundred neonates, only two mice tested positive

for the presence of this loxP site. Subsequent Southern analysis of tails from these mice showed that the locus was not targeted. It is unclear why coat color transmitted, but the transgenic allele did not.

Southern blot and genotyping of conditionally targeted mice.

Southern blot analysis was performed by using standard methods (75). Genomic DNA was digested with NdeI, ran on a 0.7% TAE agarose gel, and then transferred to a Hybond-N membrane (GE Healthcare and Life Sciences). Subsequent steps were done according to the standard protocol. The 5' probe was amplified from genomic DNA using the following primers: forward – ccaaagatgtgtttggaggcgg, reverse – gcctctgcctcccaagtgctgggattaaag. The 3' probe was amplified with the following primers: forward – agtgctagccttcctcggcatg, reverse – ccccagacagtgatgtcacctgtc. Probes were cloned into pBluescript SK II(+), cut from the vector, and labled with [α-^{32}P]dCTP using the RadPrime DNA Labelling System (Invitrogen) according to kit directions.

To genotype conditionally targeted mice, the presence of the loxP site 3' to the knockout arm was checked using the following primers: forward – CAC AGC CAT TGG GTG AAG ACC TG and reverse – GAC TGC ATT CAA TAC ACT CCT GGA ACC. In the absence of the loxP site, the size of the band is 112bp (wild type), and in the presence of the targeted allele, the size of the band is 220bp. To check for Cre-mediated take out following FLP recombination to remove the neomycin resistance cassette, the following primers were used: forward – GGC TCT TTG TGC CTA TAA CCA CTC G and reverse – GAC TGC ATT CAA TAC ACT CCT GGA ACC (same reverse primer as above). The wild type locus gives a band size of 629bp, the targeted locus following FLP-mediated recombination gives a band size of

889bp, and the targeted locus following FLP-mediated recombination and Cre-mediated recombination gives a band size of 225bp.

Y2H screen using skeletal muscle cDNA library.

Klhl40 yeast two-hybrid analysis was performed using the Clontech Matchmaker Gold Yeast Two-Hybrid System with a Mate & Plate – Human Skeletal Muscle cDNA library as previously described (76). Klhl40 was N-terminally fused with a GAL4-DNA binding domain by cloning the full-length Klhl40 coding sequence into the provided pGBKT7 vector (pGBKT7-Klhl40) using the EcoRI and EcoRV restriction sites at the 5' and 3' end, respectively. The pGBKT7-Klhl40 vector was transformed into a yeast library containing skeletal muscle cDNA fragment fused to a GAL4 activation domain, and then were subjected to several rounds of selection according to kit instructions. 20 colonies remained which were sequenced to identify the encoding cDNA fragment. Clones producing frameshifted proteins were discarded. The remaining 13 clones are reported.

Cloning of epitope tagged constructs for protein stability and immunoprecipitation experiments.

The *Klhl40* CDS was subcloned into the HindIII and XbaI sites of a p3XFLAG-CMV-10 vector modified with a tandem HA tag (p3XFLAG-CMV-10-NHA) and also subcloned into the HindIII and AgeI sites of a custom pcDNA3.1-Hygro vector with a HA-3XFLAG (pcDNA3.1/Hygro(+)-C-HA-3XFLAG) tandem tag for N-terminal 3XFLAG-HA and C-terminal HA-3XFLAG fusion, respectively. N-terminal fused Klhl40 is referred to as 3XFLAG-HA-Klhl40 or FLAG-Klhl40 while C-terminally fused Klhl40 is referred to as Klhl40-HA-3XFLAG. Both N- and C-terminally fused Klhl40 constructs were subcloned into the pBabe-X retroviral vector

(referred to as pBX-3XFLAG-HA-Klh40 and pBX-Klhl40-3XFLAG-HA, respectively) by adding PmeI sites by PCR and (77). Full length EGFP was also N-terminally fused with 3XFLAG-HA (3XFLAG-HA-EGFP) and subcloned into pBabe-X (pBX-3XFLAG-HA-EGFP).

To clone Neb_{frag}-myc, the cDNA sequence corresponding to the protein fragment of Neb identified from the Klhl40 yeast two-hybrid analysis (NCBI reference sequence NM_010889.1, nucleotides 17627-18221) was cloned from adult mouse skeletal muscle cDNA with a 5' primer containing the sequence: CGC CAC CAT G, which adds a Kozak sequence and a translational start site. The clone was directly ligated into the EcoRI and XhoI sites of pcDNA3.1(+)/myc-His A (Invitrogen) to allow for fusion with a C-terminal myc tag. Similarly, full length Lmod3 was cloned with primers that retained the endogenous Kozak sequence, and cloned into the BamHI and XhoI sites of pcDNA3.1(+)/myc-His A.

C2C12 infection and protein extraction for tandem affinity purification (TAP).

26μg of the pBX-3XFLAG-HA-EGFP, pBX-3XFLAG-HA-Klhl40, and pBX-Klhl40-HA-3XFLAG retroviral constructs were transfected into 80% confluent Platinum E cells (Cell Biolabs) on 15cm plates using Fugene 6 (Promega) at a 3:1 DNA to Fugene 6 ratio according to manufacturer's directions. Viral media was collected at 24 and 48 hours post-transfection by drawing off media and filtering through a 0.45μm syringe filter (Corning). Polybrene was added to viral media to a final concentration of 10μg/mL. Following filtration, viral media was added immediately to 100% confluent C2C12 myoblasts (from American Type Culture Collection) in growth media (DMEM with 10% fetal bovine serum [FBS; Life Technologies] and 1% antibiotic-antimycotic [Life Technologies]) on 15cm plates coated with 0.1% agar at 24 and 48 hours after transfection. After allowing the second infection to occur overnight,

C2C12 cells were washed with PBS and then differentiated for 5 days with differentiation media (DMEM with 2% horse serum [Life Technologies] and 1% antibiotic-antimycotic).

Protein was collected from C2C12 myotubes by washing cells and then collecting them into 5mL PBS by scraping cells with a sterile cell lifter. Collected cells were placed into 15mL conicals, pelleted at 2,000xg for 3 min 4°C, and then lysed in 500µL of FLAG lysis buffer (50mM Tris pH 8.0, 137mM NaCl, 1mM EDTA, 10% glycerol, and 10mM NaF) with 1% Triton X-100, cOmplete mini EDTA protease inhibitor cocktail (Roche), and PhosSTOP phosphatase inhibitor cocktail (Roche). Cells were pipetted several times and left on ice for at least 30 minutes to maximize lysis. Lysate was centrifuged at 20,817xg for 15 min at 4°C. The insoluble pellet was discarded while the supernatant was retained.

TAP of protein purified from C2C12 myotubes.

To immunoprecipitate proteins, each reaction was first immunoprecipitated with ANTI-FLAG M2 Affinity Gel (Sigma). For each reaction, 100µL of FLAG affinity gel was washed three times with FLAG lysis buffer, diluted to 200µL with FLAG lysis buffer with 1% TX-100, and then added to 2.4mg of C2C12 protein diluted in 1mL FLAG lysis buffer. Protein was incubated with FLAG affinity gel overnight at 4°C. The following day, the FLAG affinity gel was pelleted and washed three times with FLAG lysis buffer with 1% TX-100. Next, protein was eluted from the FLAG affinity gel with 200µL of 0.5mg/mL 3X FLAG peptide (Sigma) in FLAG lysis buffer overnight at 4°C. After elution, the affinity gel was pelleted and discarded while supernatant was retained. To each supernatant, 40µL of EZview Red Anti-HA Affinity Gel (Sigma) were washed three times and resuspended with FLAG lysis buffer in its original volume, added to eluted FLAG protein, and incubated overnight at 4°C. On the next day, the HA affinity gel was washed as before and then eluted with 80µL of 1µg/µL HA peptide (Sigma)

in FLAG lysis solution overnight at 4°C and then for an additional 2 hours at room temperature. HA affinity gel was pelleted and discarded, and the final HA eluate was retained. To each final HA eluate, 40µL of 2X Laemmli buffer (Bio-Rad) with 5% β-mercaptoethanol was added. Samples were placed on a 100C heat block and boiled down to 80µL. Protein was stored at -80°C until ready for use.

TAP protein electrophoresis and mass spectrometric analysis.

40µL of each boiled TAP protein sample was loaded into an Any kD Mini-PROTEAN TGX Gel (Bio-Rad) and ran according to standard SDS-PAGE procedures. Silver staining of gel was performed with SilverQuest staining kit (Invitrogen) according to manufacturer's instruction with staining reaction halted at 8 minutes.

Protein bands on the stained SDS-PAGE gel were cut, destained provided SilverQuest reagents, and then in-gel digested using sequencing-grade trypsin (10 ng/µL trypsin, and 50 mM ammonium bicarbonate, pH 8.0) overnight at 37°C. Peptides were sequentially extracted with 5% formic acid/50% acetonitrile and 0.1% formic acid/75% acetonitrile, sequentially, and then concentrated to about 20µL. The extracted peptides were separated using an analytical capillary column (100µm x 12cm) packed with 3 µm of spherical C18 reversed phase material with 100A pore size and 2.7u particle size (Magic C18 100Å 3u PM3/66100/00 from Michrom). An UltiMate 3000 binary pump (Thermo Scientific) was used to generate the HPLC gradient as follows: 0-5% B in 15 min, 5-40% B in 35 min, 40-100% B in 20 min (A: 0.1% formic acid in water; B: 0.1% formic acid in acetonitrile). The eluted proteins were sprayed into a Q Exactive mass spectrometer (Thermo Scientific) equipped with a nano-ESI ion source. The mass spectrometer was operated in the information-dependent mode one MS scan followed by 15 MS/MS scans for each cycle. Database searches were performed using an in-house

Mascot server (Matrix Science) and performed against the IPI mouse database. Carbamidomethyl was set as a fixed modification while methionine oxidation and diglycine-modified lysine were set as variable modifications.

Klhl40 co-immunoprecipitation (co-IP) with Neb$_{frag}$ and Lmod3.

A total of 2µg containing a combination of FLAG-Klhl40, pcDNA3.1(+)/myc/His A ("EMPTY"), Lmod3-myc, and/or Neb$_{frag}$-myc was combined with Fugene 6 at a 3:1 DNA ratio to Fugene 6 and then added to 80-90% confluent COS7 cells in 6-well plates. 48 hours post-transfection, cells were washed with PBS and then scraped into 1mL of PBS and transferred to 1.5mL microcentrifuge tubes. Collected cells were pelleted at 2,000xg for 3 minutes at 4°C. The supernatant was discarded and cells were resuspended and left on ice for at least 10 minutes in 100µL FLAG lysis buffer with 1% Triton X-100, cOmplete mini EDTA protease inhibitor cocktail, and PhosSTOP phosphatase inhibitor cocktail. Lysate was centrifuged at 20,817xg for 15 min at 4°C. The insoluble pellet was discarded while the supernatant was retained.

To immunoprecipitate protein, 1µL of c-Myc antibody (Life Technologies) was added to 1mg of protein diluted to 1mL in FLAG lysis buffer with 1% TX-100 which was incubated overnight at 4°C. The following day, 50µL of Dynabeads Protein G (Life Technologies), which were washed three times with five volumes of FLAG lysis buffer with 1% TX-100 using a magnetic stand (Millipore), were added to each immunoprecipitation reaction and incubated at 4°C for at least 2 hours. Following incubation, the beads were washed five times with one volume of FLAG lysis buffer with 1% TX-100 as before. After the final wash, the beads were moved to a new centrifuge tube and pelleted with a magnetic stand. The supernatant was discarded and 15µL 2X Laemmli buffer with 5% β-mercaptoethanol diluted with 15µL of FLAG

lysis buffer with 1% TX-100 was added to the beads followed by boiling for 5 minutes. Following boiling, beads were pelleted by centrifugation at max speed for 1 minute at room temperature. 15µL of supernatant was loaded onto a 4-20% Mini-PROTEAN TGX gel (Bio-Rad). For input lanes, 25µg of the original COS7 cell lysate was mixed with one volume of 2X Laemmli buffer with 5% β-mercaptoethanol, boiled for five minutes, and then loaded onto the aforementioned SDS-PAGE gel. Following electrophoresis, standard Western blot analysis was performed (see below).

Klhl40 stabilization of Neb_{frag} and Lmod3 and proteasomal analysis.

A total of 2µg containing a combination of FLAG-Klhl40, p3XFLAG-CMV-10-NHA ("EMPTY"), Lmod3-myc, and/or Neb_{frag}-myc was combined with Fugene 6 at a 3:1 DNA ratio to Fugene 6 and then added to 80-90% confluent COS7 cells in 6-well plates. 24 hours following transfection, growth media containing either 0.1% DMSO (vehicle) or 10µM MG132 (APExBIO) in 0.1% DMSO was added to cells. After a total of 48 hours following transfection, cells were washed with PBS and then scraped into 1mL of PBS and transferred to 1.5mL microcentrifuge tubes. Collected cells were pelleted at 2,000xg for 3 minutes at 4°C, and then resuspended in 1mL of PBS. Each tube was then split into two 500µL volumes and then pelleted again as before. One set of cells was resuspended in 1mL TRIZOL for RNA and subsequent qPCR analysis. Protein was extracted from the remaining set of cells in the same manner as the co-immunoprecipitation experiment except that only 50µL of lysis buffer was used. 25µg of protein was mixed with one volume of 2X Laemmli buffer with 5% β-mercaptoethanol, boiled for five minutes, and then loaded onto a 4-20% Criterion TGX gel (Bio-RAD). Following electrophoresis, standard Western blot analysis was performed (see below).

Ubiquitination analysis of Neb_{frag} and Lmod3.

A total of 12µg containing a combination of Lmod3-myc and p3XFLAG-CMV-10-NHA ("EMPTY") or FLAG-Klhl40 was combined with Fugene 6 at a 3:1 DNA ratio to Fugene 6 and then added to 80-90% confluent COS7 cells in 10cm dishes. Proteasome inhibitor was added in the same manner as was stated before for the proteasomal analysis. Protein was collected from by washing cells and then collecting them into 5mL PBS by scraping cells with a sterile cell lifter. Collected cells were placed into 15mL conicals, pelleted at 2,000xg for 3 min 4°C, resuspended in 1mL PBS, transferred to a microcentrifuge tube, and pelleted again. The supernatant was discarded and cells were lysed with 50µL FLAG lysis buffer with 1% Triton X-100 and 6M urea. 6M urea was used to disrupt protein-protein interactions to prevent co-immunoprecipitation of Lmod3-myc with FLAG-Klhl40 which was confounding analysis of ubiquitinated Lmod3-myc. Cells were left on ice for at least 5 minutes, and then diluted with 950µL FLAG lysis buffer with 1% Triton X-100 bringing the final concentration of urea to 0.3M. Lysate was centrifuged at 20,817xg for 15 min at 4°C. The insoluble pellet was discarded while the supernatant was retained.

To immunoprecipitate ubiquinated protein, 5µL of K48 anti-ubiquitin antibody (Apu2; EMD Millipore) was added to 1.5mg of protein diluted to 500µL with FLAG lysis buffer with 1% Triton X-100 and 0.3M urea, and then diluted again with 500uL of FLAG lysis buffer with 1% Triton X-100 bringing the total urea concentration to 0.15M. Subsequent immunoprecipitation steps were performed in the same manner as the co-immunoprecipitation experiment except for the protein elution. To elute protein from beads, only 7.5µL 2X Laemmli buffer with 5% β-mercaptoethanol diluted with 7.5µL of FLAG lysis buffer with 1% TX-100 was added to the

beads followed by boiling for 5 minutes. Subsequent electrophoresis and Western analysis of eluate and input protein is the same as the co-immunoprecipitation experiment.

Neb$_{frag}$ and Lmod3 stabilization with Klhl40 domain deleted protein.

To generate domain deletions of Klhl40, PCR gene splicing by overlap extension (PCR SOEing) was utilized (78). Two separate PCR SOEing reactions were performed. In the first reaction, Klhl40 –BTB, Klhl40 –BACK, and Klhl40 –KR were generated by splicing the following regions (numbers correspond to NCBI reference sequence NM_028202.3): –BTB: nucleotides 170-235 with 545-2035; –BACK: nucleotides 170-565 with 881-2035; –KR: nucleotides 170-1246 with 2009-2035. After cloning the first set of deletions, a second PCR SOEing reaction was performed to generate Klhl40 –BTB –KR, Klhl40 –BACK –KR, Klhl40 –BTB –BACK, and Klhl40 –BTB –BACK, –KR using the original three deletions to splice together the following regions (numbers correspond to original NCBI reference sequence): –BTB –KR: 170-235 with 545-1246 and 2009-2035; –BACK –KR: 170-565 with 881-1246 and 2009-2035; –BTB –BACK: 170-235 with 545-565 and 881-2035; –BTB –BACK –KR: 170-235 with 545-565, 881-1246, and 2009-2035. All deletions were cloned into the p3XFLAG-CMV-10-NHA vector with the same endogenous Kozak sequence and translational stop site as 3XFLAG-HA-Klhl40.

To test the ability of each Klhl40 variant in stabilizing Neb$_{frag}$ or Lmod3, cells were co-transfected with a total of 2µg containing a combination of Neb$_{frag}$-myc or Lmod3-myc with p3XFLAG-CMV-10-NHA (“EMPTY”), 3X-FLAG-HA-Klhl40 (“FL”), or one of the seven domain deletion variants of Klhl40 in the same manner as the co-immunoprecipitation experiment. RNA and protein were simultaneously extracted and analyzed in the same manner as the first experiment to test the stabilization of Neb$_{frag}$ and Lmod3 with Klhl40.

Western blot analysis.

For all cell culture experiments, 25µg of protein was analyzed except for immunoprecipitated proteins whose final concentrations were not measured. For all Western analysis of tissue protein, 50µg of protein was used except for P1 mice where only 25ug of protein was used. To extract protein from tissues, tissues were disassociated in FLAG lysis buffer with 1% Triton X-100, cOmplete mini EDTA protease inhibitor cocktail, PhosSTOP phosphatase inhibitor cocktail, and 6M urea using a mini pestle followed by sonication. Tissue lysate was centrifuged at 20,817xg for 15 minutes at 4°C and the insoluble pellet was discarded. Protein was mixed with one volume of 2X Laemmli buffer with 5% β-mercaptoethanol as described before for cell culture protein lysates, and standard SDS-PAGE electrophoresis was performed. All protein was transferred to Immobilon-P PVDF membrane (EMD Millipore) using a Trans-Blot SD Semi-Dry Transfer Cell (Bio-Rad).

To probe for FLAG-Klhl40, 1:20,000 dilution of mouse monoclonal anti-FLAG M2 (Sigma) was used with a 1:20,000 dilution of goat anti-mouse HRP conjugated secondary antibody (Bio-Rad). To probe for Neb_{frag}-myc or Lmod3-myc, a 1:5000 dilution of mouse monoclonal c-Myc antibody (Life Technologies) was used with a 1:10,000 dilution of conjugated anti-mouse secondary antibody. GAPDH was analyzed with a 1:10,000 dilution of mouse anti-GAPDH antibody (EMD Millipore) followed by a 1:20,000 dilution of conjugated anti-mouse secondary antibody. To analyze Lmod3, a 1:10,000 dilution of rabbit anti-Lmod3 (ProteinTech) was used with a 1:10,000 dilution of goat anti-rabbit HRP conjugated secondary antibody (Bio-Rad). For cell culture and animal tissue protein analysis, all primary antibodies were incubated with blots for 1 hour at room temperature and overnight at 4°C, respectively,

while secondary antibodies for both were incubated for 30 minutes at room temperature. All antibodies were diluted in 5% non-fat milk in TBS with 0.1% Tween-20 (5% milk/TBST).

Dot blot analysis of Neb and Gapdh.

A Bio-Dot microfiltration apparatus (Bio-Rad) was used according to manufacturer instructions with a few exceptions. 50μg and 25μg of P8 and P1 quadriceps protein, respectively, in 15μL 1X Laemmli buffer with 2.5% β-mercaptoethanol (originally prepared for SDS-PAGE gel analysis) was diluted with 285μL FLAG lysis buffer (no Triton) and loaded onto the dot blot apparatus that contained a 0.45μm nitrocellulose membrane (Bio-Rad). After allowing the protein to pass by gravity through the apparatus, 500μL of TBS was added to each well and also allow to pass by gravity to dilute out all detergents and maximize binding of protein to the membrane. All subsequent steps involving the use of the apparatus were done based on manufacturer directions. The membrane was blocked with 5% milk/TBST for 30 minutes at room temperature and then analyzed like a standard Western blot. Neb and Gapdh were analyzed separately using equal amounts of protein. Neb was analyzed with a 1:1,000 dilution of rabbit anti-Neb antibody (ProteinTech) while Gapdh was analyzed with a 1:1,000 dilution of mouse anti-GAPDH antibody. Secondary antibodies were also used at a 1:1,000 dilution. Primary antibodies were incubated overnight at 4°C while secondary antibodies were incubated for 30 minutes at room temperature.

Quantitative proteomic analysis of skeletal muscle.

Protein from quadriceps of P6 mice (3 WT and 3 KO) was extracted using Chemicon lysis buffer (50mM Tris-HCl [pH 6.8], 1mM EDTA, and 2% SDS) with cOmplete mini EDTA protease inhibitor cocktail and PhosSTOP phosphatase inhibitor cocktail. Tissue was

disassociated in the same manner as described for Western blot analysis except everything was performed at room temperature to prevent SDS precipitation. To remove SDS, 500µg of protein was diluted in 100µL of the previous lysis buffer (including all additives) and then precipitated overnight at -20°C with six volumes of acetone pre-chilled to -20°C. Precipitated protein was pelleted by centrifugation at 8,000xg for 1 minute at 4°C and then washed three times with pre-chilled acetone. After washing, acetone was decanted, aspirated, and allowed to air dry for 10 minutes. Protein was resuspended in 100µL FLAG lysis buffer with 1% Triton X-100, cOmplete mini EDTA protease inhibitor cocktail, PhosSTOP phosphatase inhibitor cocktail, and 6M urea. 100µg of resuspended protein was then denatured, reduced, alkylated, and digested according to TMT Mass Tagging Kit (Thermo Scientific) directions. All six protein samples were labeled with the six available isobaric tags (WT: 126, 127 and 128; KO: 129, 130, and 131) also according to kit directions except the reaction was quenched with 5µL 50% hydroxylamine. 30µL of labeled sample was combined into a single tube and then concentrated to approximately 20µL with a SpeedVac centrifuge (Thermo Scientific).

Approximately 50µg of TMT labeled peptides were loaded onto a 250µm (inner diameter) two-phase column containing a 5cm C18 reverse phase (RP) section packed with 3µm, 100Å, Luna C18 resin (Phenomenex) and upstream of a 2cm strong cation exchange (SCX) section, packed with 5µm, 100 Å Luna SCX resin (Phenomenex). Protein was desalted with Buffer A (0.1% formic acid) and then peptides were eluted from RP to SCX resin with Buffer B (80% acetonitrile in 0.1% formic acid). Then, peptides were separated with a 75µm (ID) SCX 10cm column packed with 5µm, 100 Å Luna SCX resin using an Agilent 1200 HPLC system to generate the following gradient:

Time (min)	SCX Buffer A (%)	SCX Buffer B (%)	SCX Buffer C (%)
0	100	0	0
5	95	5	0
65	50	50	0
95	0	100	0
95.5	0	0	100
105	0	0	100
105.5	100	0	0
120	100	0	0

The SCX buffers used were: SCX Buffer A (7mM KH_2PO_4, 10% acetonitrile, pH 2.65), SCX Buffer B (7mM KH_2PO_4, 350mM KCl, pH 2.65), and SCX Buffer C (50 mM K_2HPO_4, pH 7.5). Each 5 min interval was treated as a single fraction. Each fraction of peptides was separated by an analytical capillary column (50µm X 17cm) packed with 5µm spherical C18 reversed phase material (YMC). A nanoAcquity UPLC system (Waters) was used to generate the following HPLC gradient: 0-30% B in 75 min, 30-70% B in 15 min, 70-90% B in 5 min (A = 0.1% formic acid in water, B = 0.1% formic acid in acetonitrile). The eluted peptides were sprayed into a LTQ ORBITRAP Velos mass spectrometer (ThermoFisher Scientific, San Jose, CA, USA) equipped with a nano-ESI ion source. The mass spectrometer was run in the same mode and searched the same database as stated for the TAP experiment. The search parameters were: 7 ppm mass tolerance for precursor ions, 0.02 Da mass tolerance for product ions, with three missed cleavage sites allowed for trypsin digestion. Three variable modifications were included: protein N-Terminal acetylation, methionine oxidation, and cysteine carbamidomethylation. Two fixed modification were include: protein N-Terminal TMT6plex and lysine TMT6plex. The search results were filtered with both peptide significance threshold and expectation value to be below 0.05. The Mascot Percolator scores were used for all peptides. The quantitation method used was Proteome Sciences 6-plex

Tandem Mass Tags(R) in Mascot 2.3.2 (Matrix Science). Relative abundance of each protein was reported relative to 126 reporter ion signal. Only statistically significant protein changes are reported. Any protein that was not reliably detected in all six groups was excluded from analysis.

KLHL40 deficient patients sample analysis.

Dot blots for human samples were performed in the same manner as mouse samples. Western blotting was performed on patient and healthy human control muscle biopsies as previously described (17). Briefly, 8 µm thick sections were cut on a cryostat from frozen biopsies and lysed in Lysis Buffer (8 M urea, 40% glycerol, 4% SDS, 125 mM Tris, pH 8.8) supplemented with protease inhibitor cocktail (Sigma) and 50 mM DTT and heated to 94 °C for 5 minutes. An equal volume of Laemmli Sample Buffer (Biorad) was added, the samples were sonicated and centrifuged at 15,000 g for 5 minutes. The supernatants were removed and stored at -80 °C.

Supernatants were run on NuPAGE® Bis-Tris 4-12% gels (Life Technologies) and transferred to PVDF membrane. Membranes were blocked for at least 1 hour at room temperature (RT) in 5% skim milk powder in Wash Buffer (0.1% Tween-20 in PBS), and then incubated with primary antibodies overnight at 4 °C. Membranes were then washed three times for at least 15 minutes in Wash Buffer, incubated with secondary antibody for at least 1 hour at RT and washed again. Detection was performed with the ECL Plus substrate (Pierce).

For Western analysis, a mouse monoclonal antibody to GAPDH (G8795, Sigma; 1:80.000) and rabbit polyclonal antibodies to KLHL40 (HPA024463, Sigma; 1:5,000) and Lmod3 (14948-1-AP, Proteintech; 1:10,000) were used. Anti-mouse HRP and anti-rabbit HRP

secondary antibodies were both used at a 1:10,000 dilution. For dot blot analysis, mouse anti-GAPDH antibody (HPA024463, Sigma; 1:5,000) and rabbit anti-Neb antibody (19706-1-AP, ProteinTech; 1:1000), were used on separate blots and analyzed like before with a 1:1000 dilution of their respective HRP secondary antibodies.

CHAPTER THREE

LOSS OF LMOD3 CAUSES A DEGENERATIVE MYOPATHY

INTRODUCTION

In the previous chapter, we showed that Lmod3 was the most down-regulated protein in the muscle proteome of Klhl40 deficient mice and that this protein was also dramatically decreased in KLHL40 deficient patients. However, the function of Lmod3 and whether this protein contributed to the Klhl40 KO phenotype remained unclear.

A previously published report shows the importance of Lmod2, a protein highly homologous to Lmod3, in the organization of sarcomere thin filaments in cultured cardiomyocytes (32). The authors found that knockdown or overexpression of Lmod2 results in cardiomyocytes with disarrayed sarcomeres. To better understand the molecular mechanism underlying this phenotype, the authors used an *in vitro* actin polymerization assay and show that Lmod2 dramatically increases the rate of actin polymerization. Based on these findings, the authors proposed that Lmod2 plays a role in the initial polymerization of sarcomere thin filaments.

In Chapter Two, we show that Lmod3, like Lmod2, localizes to the A-band of the sarcomere as would be expected of a protein binding the pointed end of thin filaments. However, the loss of Lmod2 or Lmod3 had not been studied in an animal model, and it was not clear whether either truly affected initial assembly of sarcomere thin filaments. Because we are interested in studying the role of Lmod3 in muscle biology and especially within the

context of our Klhl40 deficient animals, we generate Lmod3 knockout mice using transcription activator-like effector nuclease (TALEN) mutagenesis.

TALEN technology is a genomic editing technique that allows precise targeting of a variety of loci in any genome (reviewed in (79)). Originally, transcription activator-like effectors were products found to be secreted by the plant-based bacterial pathogen, *Xanthomonas*, which specifically bound to sequences within the DNA of the host plant to act as transcriptional activators that favored the bacteria's pathogenesis. The sequence specificity of the TALE proteins was deciphered and found to be a simple modular construct of repetitive sequences with small regions of variability that established binding to either A, T, G, or C bases (80, 81). Not long after, it was shown that fusing the FokI catalytic domain to custom TALEs could direct these proteins to induce double strand breaks at targeted sites (82). Finally, TALENs were applied to model organisms and were shown to be incredibly efficacious for targeted genomic deletions (83).

Here, we report preliminary data showing that loss of Lmod3 results in a degenerative myopathy. Future studies of these Lmod3 deficient mice will be important for understanding the molecular function of Lmod proteins in thin actin filament regulation and whether they play a role in muscle diseases like nemaline myopathy.

RESULTS

Lmod3 overexpression does not rescue Klhl40 KO phenotype.

In the previous chapter we show that expressing *MCK-Klhl40* in the Klhl40 KO background was sufficient to rescue the KO phenotype. Because Lmod3 is the most down-regulated protein in the entire muscle proteome of Klhl40 KO mice, we wondered if over-expressing Lmod3 may ameliorate or rescue the phenotype. Using the *MCK* promoter, we over-expressed *Lmod3* in the Klhl40 KO background. Despite confirmed over-expression of the protein, Lmod3 alone does not rescue the Klhl40 KO phenotype (Figure 3.1, A and B).

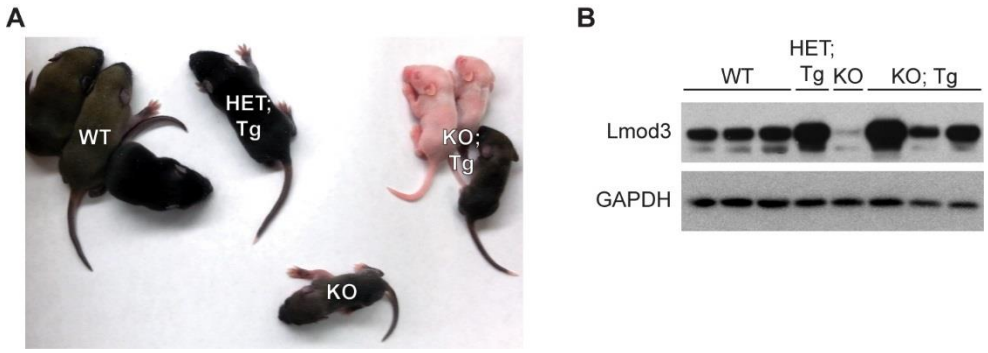

Figure 3.1. *MCK-Lmod3* does not rescue Klhl40 KO phenotype. (**A**) Representative image of P9 WT (*Klhl40*$^{+/+}$), HET; Tg (*Klhl40*$^{+/-}$*;MCK-Lmod3*), KO (*Klhl40*$^{-/-}$), and KO; Tg (*Klhl40*$^{-/-}$*; MCK-Lmod3*) mice showing that presence of the Tg (*MCK-Lmod3*) cannot rescue the Klhl40 KO phenotype. (**B**) Western blot analysis of Lmod3 in quadricep protein isolated from mice pictured in (**A**) GAPDH was used as a loading control

Targeting the Lmod3 *locus for TALEN mutagenesis.*

Despite a lack of rescue of the Klhl40 KO phenotype by overexpression of Lmod3 in muscle,, it did not rule out the potential importance of Lmod3 in the Klhl40 KO phenotype and in muscle biology in general. We decided to take a loss-of-function approach to study Lmod3 by generating Lmod3 knockout mice using TALEN mutagenesis.

We used the Golden Gate TALEN kit 2.0 to assemble two different TALEN pairs to target the *Lmod3* locus which were designed using the TAL Effector Nucleotide Targeter 2.0 (84, 85) (Figure 3.2).

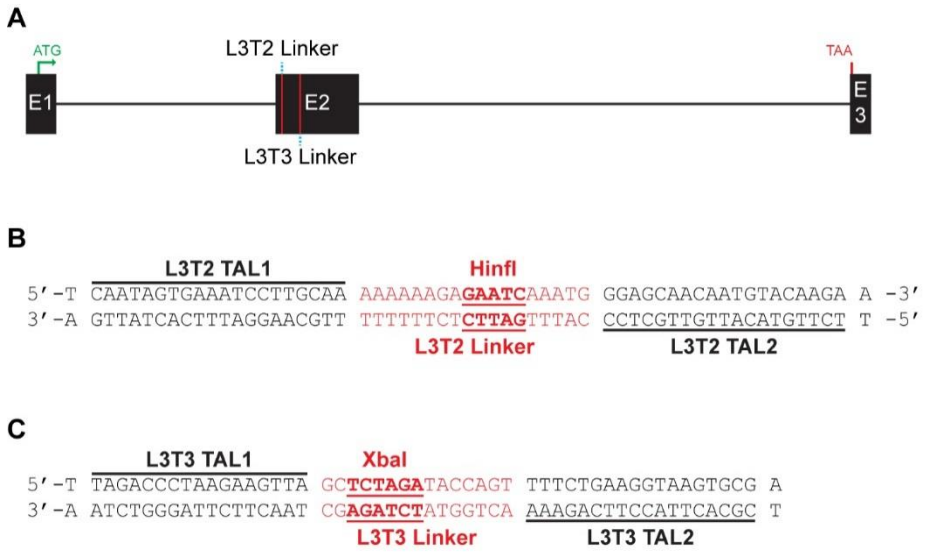

Figure 3.2. Targeting the *Lmod3* locus with TALENs. (**A**) *Lmod3* genomic locus showing linker regions targeted by L3T2 and L3T3 TALEN pair constructs. Black boxes represent exons. Start (ATG) and stop codons (TAA) are also shown. (**B**, **C**) Base pair view of (**B**) L3T2 and (**C**) L3T3 linker regions (red). Potential restriction sites that would be disrupted by mutagenesis are highlighted in red with the restriction enzyme written above. The actual sequences targeted by each TALEN are written above their respective sequences.

Using these two TALEN pairs, we generated several lines of mice with confirmed mutations, but only a single mutant line will be discussed in this text. With the L3T2 TALEN pair, we obtained one line of mice containing a two nucleotide deletion that results in a frame shift mutation with a premature stop codon, and we confirmed that this mutation eliminates Lmod3 protein (Figure 3.3, A-C).

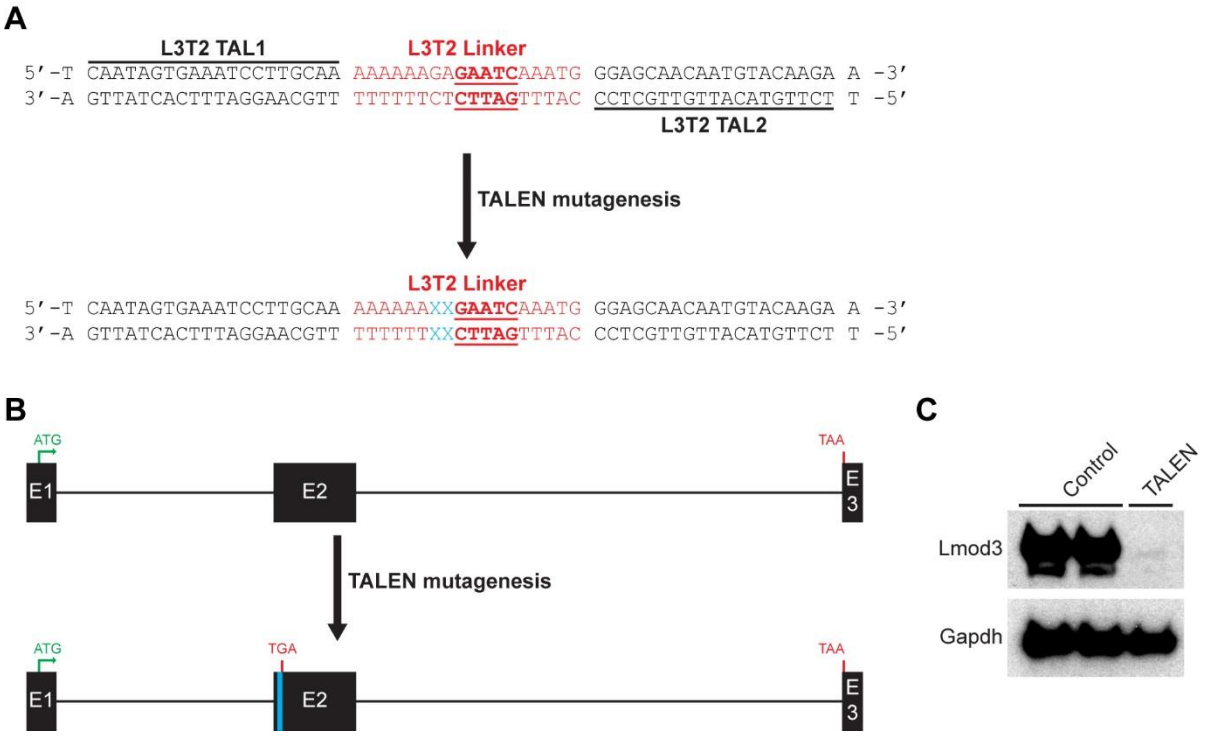

Figure 3.3. TALEN-induced frameshift mutation in *Lmod3* locus. (**A**) Base pair view of L3T2 linker region showing 2nt deletion (blue "X"s) following TALEN mutagenesis. (**B**) Location of 2nt deletion (blue line) resulting in a frame shift mutation with a premature stop codon ("TGA" near blue line). Note that this mutation does not disrupt the restriction enzyme site. (**C**) Western blot analysis of skeletal muscle from P9 littermates shows a complete loss of Lmod3 for mice homozygous for the described TALEN mutation. Control littermates are mice lacking deleterious *Lmod3* mutations.

Loss of Lmod3 results in reduced muscle mass and a degenerative myopathy.

We found that mice lacking Lmod3 displayed an approximately 25% reduction in mass which is less severe than the Klhl40 deficient mice (Figure 3.4, A and B). Additionally, mice survived to at least 3 weeks of age. However, upon gross dissection, we noticed that muscle mass was dramatically decreased in Lmod3 deficient mice (Figure 3.4, C and D). Histological analysis of these muscles revealed fibers with disorganized sarcomeres, similar to what was observed in Klhl40 KO muscles (Figure 3.4E). In addition, there was evidence of fiber size

heterogeneity and muscle degeneration and regeneration, but more analysis is needed to verify these observations (data not shown).

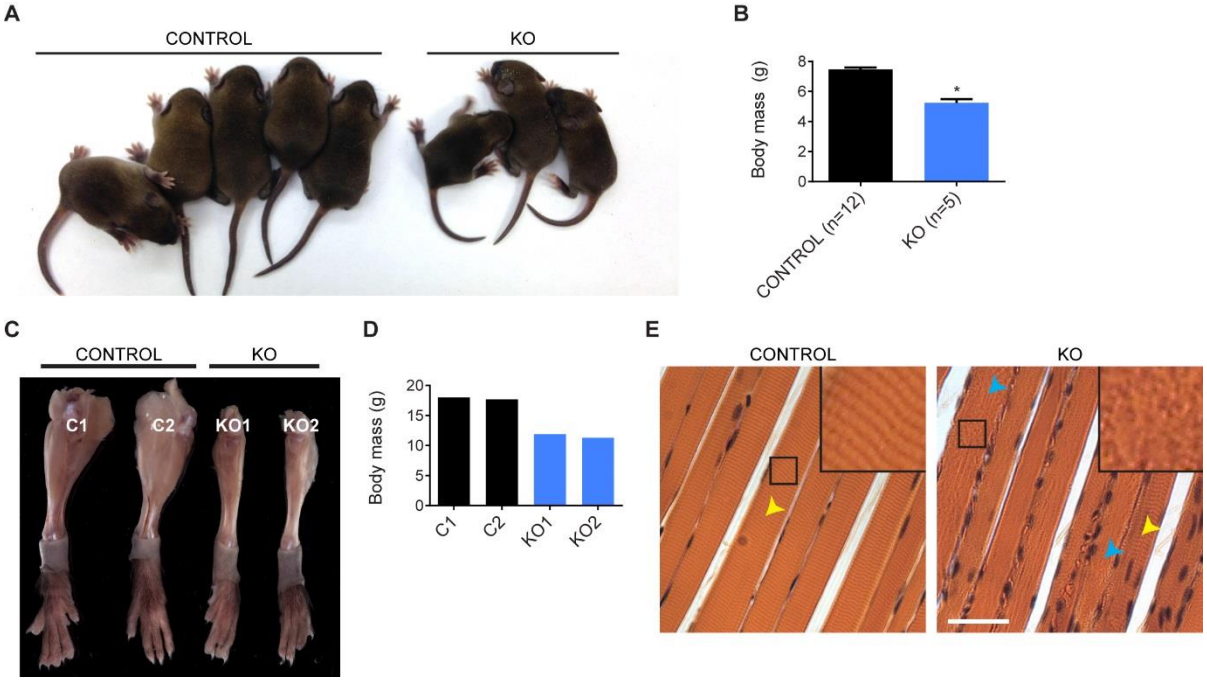

Figure 3.4. Loss of Lmod3 causes a muscle myopathy. (**A**) Representative image of P9 Lmod3 KO pups. (**B**) Mass of P9 KO mice is reduced by approximately 25%. (**C**) Limbs from 3 week old Lmod3 control mice (mice without any deleterious Lmod3 mutations) and Lmod3 KO mice shows a dramatic reduction in muscle mass. (**D**) Body mass of mice with the corresponding labeled limbs in (**C**). (**E**) Representative hematoxylin and eosin stained paraffin sections of stretched TA muscles from 3 week old Lmod3 KO mice. Yellow arrowheads point to representative fibers with normal striations. Blue arrowheads point to representative fibers with disrupted sarcomere structure. Insets show magnified view of WT fiber with normal striations compared to the inset in the KO fiber with completely disorganized sarcomeres. Scale bar: 40μm.

DISCUSSION AND FUTURE DIRECTIONS

Lmod3 was the most down-regulated protein in the Klhl40 deficient mouse skeletal muscle proteome, strongly implicating the protein as a downstream effector of the severe Klhl40 knockout phenotype. Preliminary data show that loss of Lmod3 is sufficient to result in a skeletal muscle myopathy. However, the severity of the Lmod3 phenotype, in terms of lethality and failure to grow, is substantially less compared to Klhl40 knockout phenotype. The implications of these observations as well as future directions are discussed.

First, the use of TALENs to generate an Lmod3 deficient mouse is subject to contention. Although TALENs have been shown to have minimal off-targeting effects, the technology is still in its infancy and more rigorous experiments must be performed to rule out the possibility of an off-target effect (86). We plan to cross our *MCK-Lmod3* mouse line into the Lmod3 deficient background and show that restoration of Lmod3 reverses the phenotype. Since we will be specifically over-express this transcript in striated muscle, we will also determine whether restoration of this transcript in muscle is sufficient to rescue the phenotype. Despite not having performed these experiments, we anticipate that the observed Lmod3 knockout phenotype is due to loss of Lmod3 in skeletal muscle

The presence of a degenerative myopathy in Lmod3 deficient mice suggests that the loss of Lmod3 likely contributes to the nemaline-myopathy like phenotype in Klhl40 deficient mice. Interestingly, myopathy is obvious by light microscopy in Lmod3 deficient mice at three weeks of age. Degenerative fibers are not observed in Klhl40 deficient mice, but these mice rarely live to three weeks of age so it is possible that Lmod3 deficient muscle has a similar appearance to Klhl40 deficient muscle at earlier ages. Further histology analysis is required to determine this possibility. Lastly, it would be interesting to use electron microscopy to

examine the Lmod3 muscle fibers to determine whether they also possess nemaline-like bodies.

Lmod3 is expressed in both heart and skeletal muscle. We show a definitive skeletal muscle phenotype, but it is possible that loss of Lmod3 in the heart may cause a cardiomyopathy. *Lmod2* transcript is more enriched in the heart than *Lmod3*, and so Lmod2 may compensate for any loss of Lmod3 in the heart. To directly test the role of Lmod3 in the heart, a conditional deletion of *Lmod3* is needed. Conditionally targeted ES cells for the *Lmod3* locus are available at KOMP, although derivation of these mice would take greater than a year.

Perhaps the most interesting future direction for this project is to find whether *LMOD3* mutations exist in any myopathic patient population. Thus far, the mouse model would suggest that patients with *LMOD3* mutations would exhibit atrophic muscle fibers, but not necessarily neonatal lethality like *KLHL40* deficient patients. It will be instructive to identify the exact myopathy occurring in the Lmod3 deficient mouse model to limit the scope of myopathic patients to be screened.

Lastly, in terms of expounding the molecular functions of Lmod3, two interesting directions should be analyzed. The first is to identify the function of Lmod3 in actin dynamics. Lmod3 is highly homologous to Lmod2 and both belong to the tropomodulin (Tmod) protein family. Tmod proteins are highly conserved across all metazoans and function as capping proteins to inhibit actin polymerization and depolymerization (reviewed in (87)). Some Tmod proteins have actin nucleation activity and a popular belief in the field is that Tmod1, the earliest expressing Tmod protein, plays a role in myofibrillogenesis (reviewed in (88)). In support of this hypothesis, Tmod1 deletion in mice results in early embryonic lethality at E9.5 with evidence of defects in actin organization (89). On the other hand, Tmod1 deletion in

cultured ES cells that are induced into embryoid body formation do show evidence of actin organization into striated filaments, although there are evident defects in muscle formation (90). Thus, the role of Tmods in myofibrillogenesis remains controversial.

A similar actin nucleation and myofibrillogenesis function was suggested for Lmod2 by Chereau, *et. al.* (32). This hypothesis was based on the actin nucleation activity of Lmod2 *in vitro* as well as the disarrayed sarcomeres in primary cardiomyocytes due to Lmod2 overexpression or knockdown. However, no experimental study directly tested the putative myofibrillogenesis function of Lmod2. Lmod3 is highly homologous to Lmod2, suggesting that it may have a similar function (32), but mice lacking Lmod3 have functional sarcomere. Our results suggest, at the very least, that Lmod3 is not absolutely critical for myofibrillogenesis. One possibility is that Lmod3 regulates the formation of new actin filaments postnatally. Muscle mass increases dramatically during postnatal development and if Lmod3 is responsible for actin assembly in these newer fibers, it could explain the lack of hypertrophy in postnatal mice. To confirm this hypothesis, it will be important to establish the expression of *Lmod3* during development and compare normalized muscle mass of embryonic mice versus various postnatal ages. In addition, it will be important to purify recombinant Lmod3 protein and show directly in an *in vitro* actin polymerization assay, that Lmod3 regulates actin polymerization activity. If this polymerization activity exists, it would be interesting to see whether Klhl40 protein influences Lmod3's functions directly.

Finally, because Lmod3 plays a likely role in actin dynamics, it will be interesting to see if it belongs to the actin-MRTF-SRF regulatory circuit (91, 92). Briefly, the actin-MRTF-SRF transcriptional network is an eloquent model for describing how the polymerization state of actin feeds back to regulate transcription. In the presence of unpolymerized actin monomers, G-actin, MRTF is bound and restricted from shuttling into the nucleus where it

would serve as a transcriptional cofactor for SRF to transcribe specific genes involved with actin. Once G-actin levels drop, presumably due to increased assembly of F-actin filaments, MRTF is free to shuttle to the nucleus, bind SRF, and activate transcription of genes involved in actin assembly (reviewed in (93)). Loss of Lmod3 should perturb actin dynamics causing alterations to the MRTF/SRF genes. In addition, if Lmod3 belongs to the actin-MRTF-SRF circuit, *Lmod3* promoter should contain a conserved CArG-box sequence that is bound by SRF. Future work will be needed to address this model.

METHODS

Generating MCK-Lmod3 mice.

MCK-Lmod3 mice were generated in the same manner as *MCK-Klhl40* mice described in the previous chapter except using the *Lmod3* CDS.

Designing and cloning of TALEN constructs.

Exon 2 of the *Lmod3* locus was inputted into the TAL Effector Nucleotide Targeter 2.0 (https://tale-nt.cac.cornell.edu/) using Cermak preset architecture, Streubel guidelines, and "NN" G substitute (84, 85). We looked through all the recommended sequences and chose two sequences that had reasonably small linker regions (<19nt) and did not contain an excess of "A" and "T" nucleotides. Also, we chose the sequences based on whether the linker region contained a restriction site that could be used in a PCR genotyping strategy. The two chosen regions are shown in Figure 3.2, B and C.

Once we had determined the loci to be targeted, we constructed our TALENs based on the recommendations of the TAL Effector Nucleotide Targeter 2.0 using the Golden Gate TALEN kit 2.0 (84). The RVD sequences for each of the TALEN pairs are as follows: **L3T2 TAL1** - HD NI NI NG NI NN NG NN NI NI NI NG HD HD NG NG NN HD NI NI, **L3T2 TAL2** - NG HD NG NG NN NG NI HD NI NG NG NN NG NG NN HD NG HD HD; **L3T3 TAL1** - NG NI NN NI HD HD HD NG NI NI NN NI NI NN NG NG NI, **L3T3 TAL2** - HD NN HD NI HD NG NG NI HD HD NG NG HD NI NN NI NI NI. At the final step of the Golden Gate reaction, each TAL construct was ligated into the RCIscript-GoldyTALEN vector to enable *in vitro* transcription (94).

Testing TALEN mRNA for nuclease activity.

To test our TALEN constructs, we first designed a PCR genotyping strategy to clone out the region of interest that would be cleaved by each TALEN pair. The primer pair for L3T2 is: forward – cgcatgcatgtgcattcctttgtg, reverse – ttgctggtaggtgcccggat. For L3T3: forward – atccgggcacctaccagcaa, reverse – gctgctgctgctgttcctcc (Figure 3.5A). We optimized this PCR reaction to give only a single band with our standard genotyping reaction. Then, we performed PCR amplification on wild type DNA from standard mouse tail lysates for L3T2 and L3T3 followed by digestion with HinfI and XbaI, respectively (Figure 3.5, B and C). This step confirmed that these enzymes could completely digest the PCR product in the standard PCR genotyping buffer without leaving any undigested DNA.

Next, we took our L3T2 and L3T3 TALEN pair constructs in RCIscript-GoldyTALEN and linearized the plasmid with SacI. We used 1μg of each linearized template for *in vitro* transcription using the mMessage mMachine T3 transcription kit (Life Technologies) per manufacturer's instructions. Transcribed mRNA was purified using the MEGAclear transcription clean-up kit (Life Technologies) per manufacturer's instructions. RNA was eluted with two 50uL volumes of nuclease-free water (Life Technologies) that was heated to 95C before use. To check for RNA quality, 1μg of RNA was run on a 1% agarose formaldehyde gel. Finally, RNA was aliquoted into 10uL and stored at -80°C until further use.

Finally, we tested the activity of our TALEN mRNAs by using a previously described cell-free *in vitro* cutting assay (95). Briefly, 2μg of L3T2 or L3T3 PCR product was combined with 3μg of L3T2 TAL1 and L3T2 TAL2 or L3T3 TAL1 and L3T3 TAL1 mRNA respectively, 60μL of the TNT T7 Quick Master Mix (Promega), and 1.5μL of 1mM methionine to a total reaction volume of approximately 75μL. For our negative control, nuclease-free water was used instead of TALEN mRNA. The reaction was incubated at 30°C for two hours and then

overnight at 30°C with 5X volume of TALEN cutting buffer (20mM Tris-HCl pH7.5, 5mM $MgCl_2$, 50mM KCl, 5% glycerol, and 0.5 mg/mL BSA) added. The following day, DNA was purified using QIAquick gel extraction columns (QIAGEN) according to manufacturer's directions. Cleaved DNA was eluted in 30µL and then ran on a standard 2% TAE agarose gel. Note that 10µL of 10X loading dye was necessary to prevent the purified DNA cleavage reaction from floating out the well. TALEN cutting was confirmed by observing the lower ~200bp and ~120bp bands cleaved from the L3T2 and L3T3 PCR reactions, respectively (Figure 3.5C). It should be noted that the cleaved products were much lower in abundance than the uncleaved products.

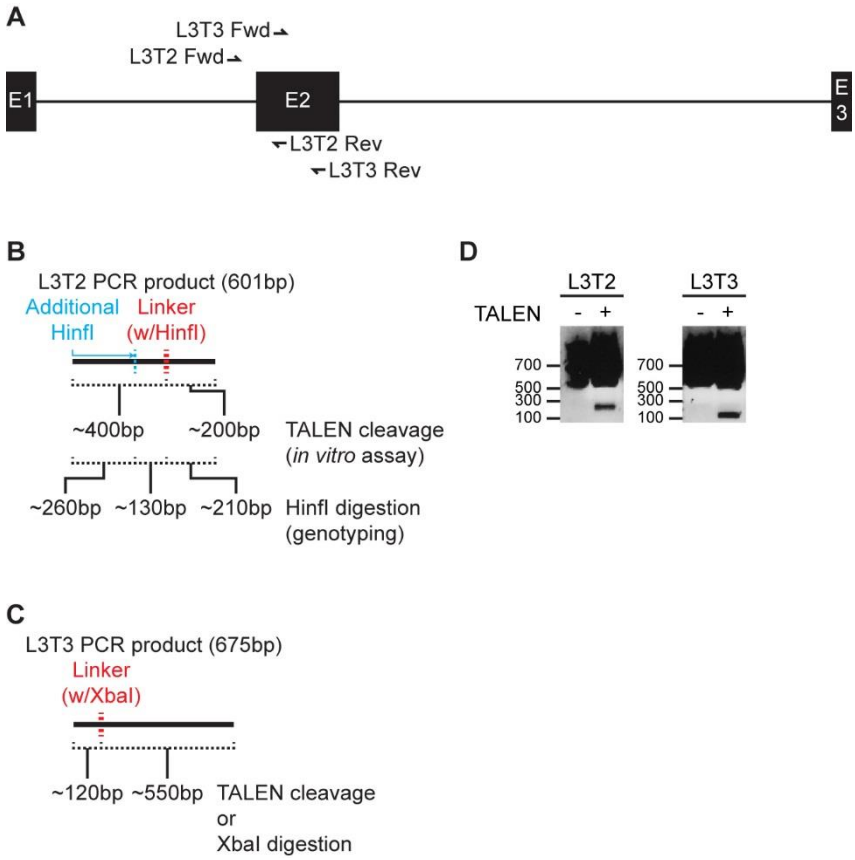

Figure 3.5. Lmod3 TALEN screening strategy. (**A**) *Lmod3* locus showing the L3T2 and L3T3 primer pairs used to PCR amplify the products seen in (**B**, **C**). (**B**) PCR product of the L3T2 PCR reaction showing the linker region that would be cleaved by the TALEN enzyme yielding 400bp and 200bp bands. Shown below the TALEN cleavage are the predicted HinfI digestion products. If the HinfI site is mutated in the linker region, a combined 340bp band should appear (130bp band + 210bp band). (**C**) PCR product of the L3T3 PCR reaction showing the linker region that would be cleaved by the TALEN enzyme yielding a 120bp and 550bp product. The same products would occur upon XbaI digesion, but if the site is mutated, the PCR product will retain its original 675bp size. (**D**) TALEN cleavage assay of the L3T2 and L3T3 PCR products using the *in vitro* cutting assay described. Shown is a TAE agarose gel. Only the lower cleaved bands are visible for L3T2 (~210bp) and L3T3 (~120bp) because of the presence of background DNA bands in the reticulolysate used originally for protein translation. Negative control is PCR DNA without any TALEN mRNA added.

Generating Lmod3 *deficient mice by TALEN mutagenesis.*

TALEN mutagenic mice were derived using L3T2 and L3T3 TALEN pair mRNAs at a concentration of 5ng/μL and 20ng/μL in oocyte injection buffer using the same technique

described in the previous chapter for *MCK-Klhl40* mice. L3T2 and L3T3 PCR reactions were performed on tail lysates of F_0 mice and then PCR amplified DNA was digested with either HinfI (L3T2) or XbaI (L3T3) to screen for mutations that disrupted the endogenous restriction sites. Mice were considered to have a mutation if a band appeared uncut.

It is possible for mutations to occur in the linker region without disrupting the restriction site. To detect these mutations, we also simultaneously performed a T7 endonuclease I, described previously (96). In this experiment, mutated DNA forms a mismatched duplex DNA complex with wild type DNA which is then cleaved by T7 endonuclease I at the site of the mismatch (which is in the linker region). To perform this experiment we took completed L3T2 and L3T3 PCR reactions and allowed them to form mismatched duplex DNA by denaturing DNA at 95°C for 5 minutes followed by renaturing DNA by cooling from 95°C to 85°C at a rate of -2°C/s, then from 85°C to 25°C at a rate of 0.1°C/s, then held at 4°C until ready to use. Each 25μL PCR reaction was split into two 12.5μL reactions. To one reaction, 2μL of NEB buffer 2 with 0.1μL of T7 endonuclease (NEB) and the total reaction volume was brought up to 30μL with H_2O. For the negative control, water was used in place of T7 endonuclease. The reaction was incubated for one hour and then ran on a 2% TAE agarose gel. If a mutation was present, cleavage products could be seen below, though at much lower abundance than the uncut bands, even if the mutant DNA was present in equal concentration as wild type DNA.

For the data reported, two F_0 mice from an L3T2 TALEN injection were intercrossed to try to generate null mice. Initially, one mouse was found to have disruption of the HinfI site while the other mouse only had a mutation detectable by the T7 endonuclease assay. Upon intercrossing, Lmod3 null mice were generated based on the runted appearance of the progeny and confirmation of loss of Lmod3 by Western blot. However, null mice were negative for TALEN mutagenesis based on both the HinfI restriction digest and T7 endonuclease I

assay. The T7 endonuclease I assay cannot detect mutant bands if the mouse is homozygous for the same mutation. Thus, we reasoned that our Lmod3 null progeny were actually homozygous for a mutation that did not disrupt the HinfI site. To test this possibility, we mixed in a known wild type L3T2 PCR reaction with our putative Lmod3 null mouse's L3T2 PCR reaction, performed the denaturation/renaturation step, and then treated these DNA with T7 endonuclease I. We saw clear cleavage of these DNA indicating the presence of a mismatch in the putative Lmod3 null mouse's DNA. Therefore, we took our L3T2 PCR reaction from our putative Lmod3 null mouse and sent it for sequencing which revealed a 2 nucleotide deletion in the L3T2 linker region that retained the HinfI restriction site. We refer to this line of mice as "L3T2-2".

To genotype L3T2-2 mice, we generated a primer pair that specifically recognizes the mutant allele: forward – cgcatgcatgtgcattcctttgtg, reverse – gcttcttgtacattgttgctcccatttgattctt. In addition, we generated a second primer pair that specifically recognizes the wild type allele: forward – cgcatgcatgtgcattcctttgtg, reverse – gcttcttgtacattgttgctcccatttgattctc. Both these primer pairs must be used with an annealing temperature of 65°C with the standard GoTaq (Promega) to prevent either the mutant or wild type primer pair from recognizing a wild type or mutant allele, respectively. An *Lmod3*$^{+/+}$ mouse was one that was positive for the L3T2-2 wild type reaction, but negative for the L3T2-2 mutant reaction. An *Lmod3*$^{+/L3T2\text{-}2}$ mouse was one that was positive for both reaction. An *Lmod3*$^{L3T2\text{-}2/L3T2\text{-}2}$ mouse was one that was only positive for the L3T2-2 mutant reaction.

Histologic analysis of Lmod3 KO muscles.

Hindlimbs of mice were severed at the distal femur and then tied onto wooden dowels with the feet of mice in full plantar flexion to stretch the tibialis anterior muscle. Muscles were

routinely fixed with 4%PFA/PBS and processed by the UTSW Molecular Pathology Core for paraffin embedding, sectioning, and hematoxylin and eosin staining.

Western blot analysis of Lmod3.

Analysis of muscle protein was done as previously described in Chapter Two.

CHAPTER FOUR

ANALYZING THE FUNCTION OF *HHATL*: *KLHL40'S* FUSSY NEIGHBOR

INTRODUCTION

Whilst analyzing the *Klhl40* locus, we noticed that there was another gene, *Hhatl*, juxtaposed to *Klhl40* with only 200nt of separation (Figure 4.1). The targeting strategy used to delete *Klhl40*, removed a 5.6kb portion of the gene. We were concerned that such a deletion might also disrupt *Hhatl* transcription given its proximity to the deleted region. Much to our dismay, we found that *Hhatl* was indeed disrupted by the deletion of *Klh40.* Initially, this caused issues with the interpretation of our *Klhl40* knockout phenotype since we could not be certain which gene was responsible for the observed phenotype. However, we resolved this issue by rescuing the Klhl40 knockout/Hhatl hypomorph mice with *MCK-Klhl40* (see Chapter Two).

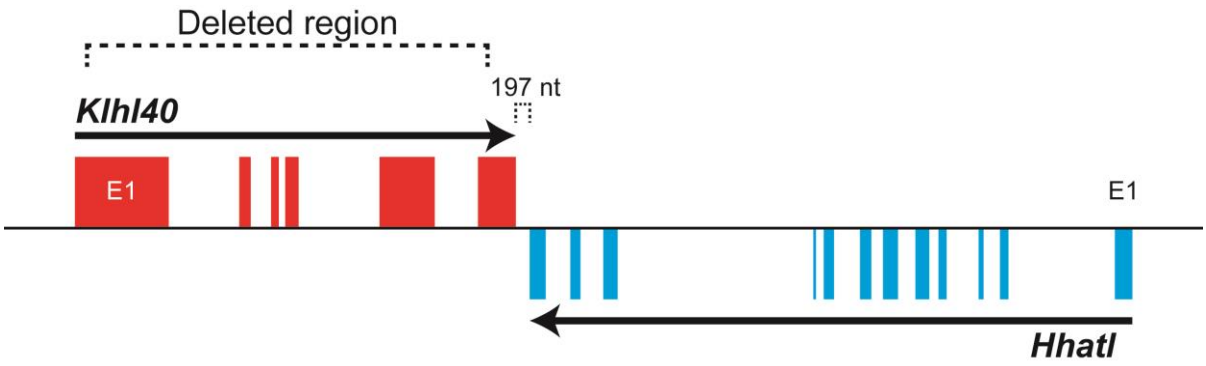

Figure 4.1. Chromosome 9 locus containing *Klhl40* and *Hhatl*. Schematic representation of the locus in the *Mus musculus* chromosome 9 containing both the *Klhl40* and *Hhatl* genes Colored boxes represent exons. *Klhl40* (red) resides on the plus strand and its tail is separated from the tail of *Hhatl* (cyan), which resides on the minus strand, by only 197nt. The 5.6kb region removed with the KOMP *Klhl40* targeting strategy is labeled as "Deleted region".

Despite not contributing to the *Klhl40* phenotype, *Hhatl* was of potential interest in of itself. The *Hhatl* locus encodes for a protein designated as hedgehog acyltransferase-like (Hhatl), belonging to the membrane-bound *O*-acyltransferase (MBOAT) family (reviewed in (97)) (Figure 4.2A). MBOAT proteins are known to participate in the acylation of lipids as well as proteins (Figure 4.2B). However, Hhatl is most closely related to MBOAT proteins involved in protein acylation, particularly hedgehog acyltransferase (Hhat). Hhat is essential for hedgehog (Hh) function, and deletion of Hhat results in severe developmental defects, phenocopying Hh deletion (98). Thus we were interested in the potential function of Hhatl, especially in skeletal muscle biology.

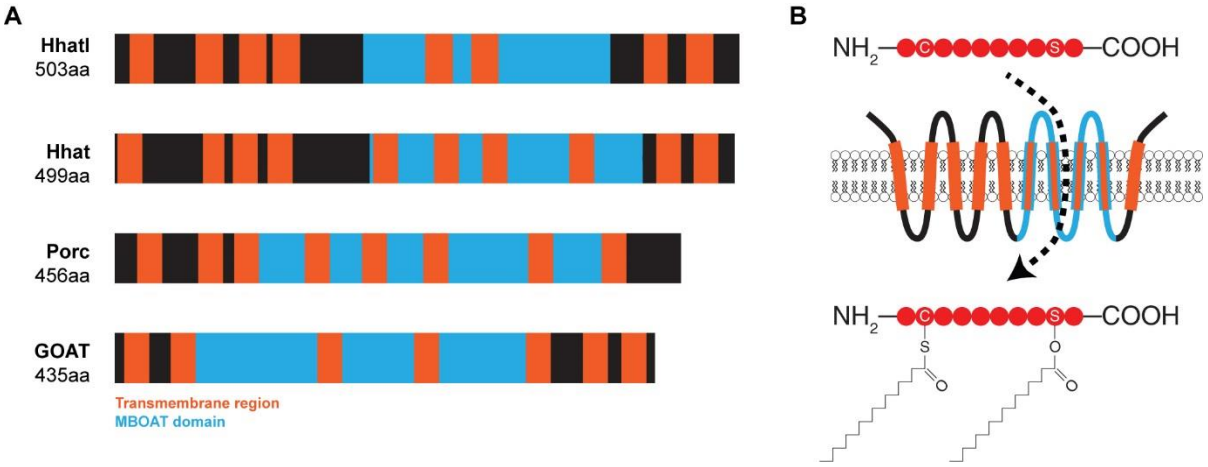

Figure 4.2. Hhatl belongs to the MBOAT family which acylates proteins. (**A**) Schematic view of Hhatl and related family members, Hhat, Porc, and GOAT. Orange boxes are transmembrane regions while the blue box represents the MBOAT domain. Black boxes are unannotated regions. (**B**) Generic depiction of a MBOAT protein, embedded in a membrane, acylating a peptide.

Previously it was reported that the *Hhatl* transcript was enriched in heart and skeletal muscles, although it was not followed upon further (99). A later paper described a potential function of Hhatl as a negative regulator of Hhat function by blocking palmitoylation of Hh, but whether this function has any pertinence to biology in a whole organism remains to be shown (100).

Before rescuing the Klhl40 phenotype, we generated a targeted *Hhatl* knockout to verify whether the Klhl40 phenotype was due to the loss of Hhatl. Here, we show preliminary results that deletion of Hhatl is lethal, but this phenotype is not recapitulated by conditional deletion of Hhatl from skeletal muscle or the heart. Following results is a discussion of the interpretation of the data and potential future directions.

RESULTS

Loss of Hhatl *does not contribute to the Klhl40 KO phenotype.*

Targeted deletion of *Klhl40* resulted in disrupted expression in *Hhatl,* making it necessary to determine whether reduced expression of *Hhatl* contributed to the Klhl40 KO phenotype (Figure 4.3A). As stated in Chapter Two, the Klhl40 KO phenotype was rescued by specifically restoring *Klhl40* using the transgenic mouse line *MCK-Klhl40* (Figure 4.3B). Interestingly, even after rescuing the phenotype, *Hhatl* expression was still disrupted in Klhl40 KO mice with the *MCK-Klhl40* transgene (KO; Tg) (Figure 4.3A). This suggests that the decreased *Hhatl* expression is not secondary to the Klhl40 KO phenotype, but rather a primary effect of disrupting the *Klhl40* genomic locus.

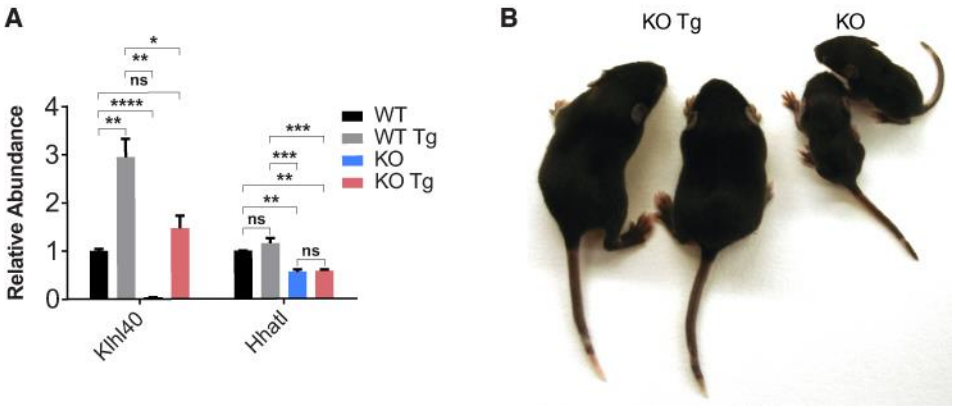

Figure 4.3. Loss of *Hhatl* does not contribute to the Klhl40 KO phenotype. (Data partially reproduced from Figure 2.8) (**A**) qPCR analysis of Klhl40 mRNA in P10 quadriceps of *Klhl40*$^{+/+}$ (WT), *Klhl40*$^{+/+}$*;MCK-Klhl40* (WT Tg), *Klhl40*$^{-/-}$ (KO), and *Klhl40*$^{-/-}$*;MCK-Klhl40* (KO Tg) mice shows approximately 3-fold overexpression of Klhl40 in WT Tg mice. *Klhl40* transcript is restored to near-normal levels in KO Tg mice. *Hhatl* transcript is decreased by 50% in KO mice and restoration of *Klhl40* in KO Tg mice does not restore *Hhatl* expression. N=3 for all genotypes. (**B**) Representative image of KO Tg and KO mice shows complete rescue of Klhl40 KO phenotype with overexpression of *Klhl40*. Values are normalized to 18S and set relative to WT quadriceps. Data are presented as mean ± SEM. *p<0.05, **p<0.01, ***p<0.001, ****p<0.0001.

Hhatl *expression is enriched in heart and skeletal muscle.*

Given the close proximity of *Hhatl* to *Klhl40*, we hypothesized that *Hhatl* expression would be very similar to *Klhl40* expression. Expression analysis of adult tissues showed that *Hhatl* was highly enriched in heart and skeletal muscle (Figure 4.4, A and B). However, unlike *Klhl40*, *Hhatl* showed substantial expression in neural tissues as well as several other tissues.

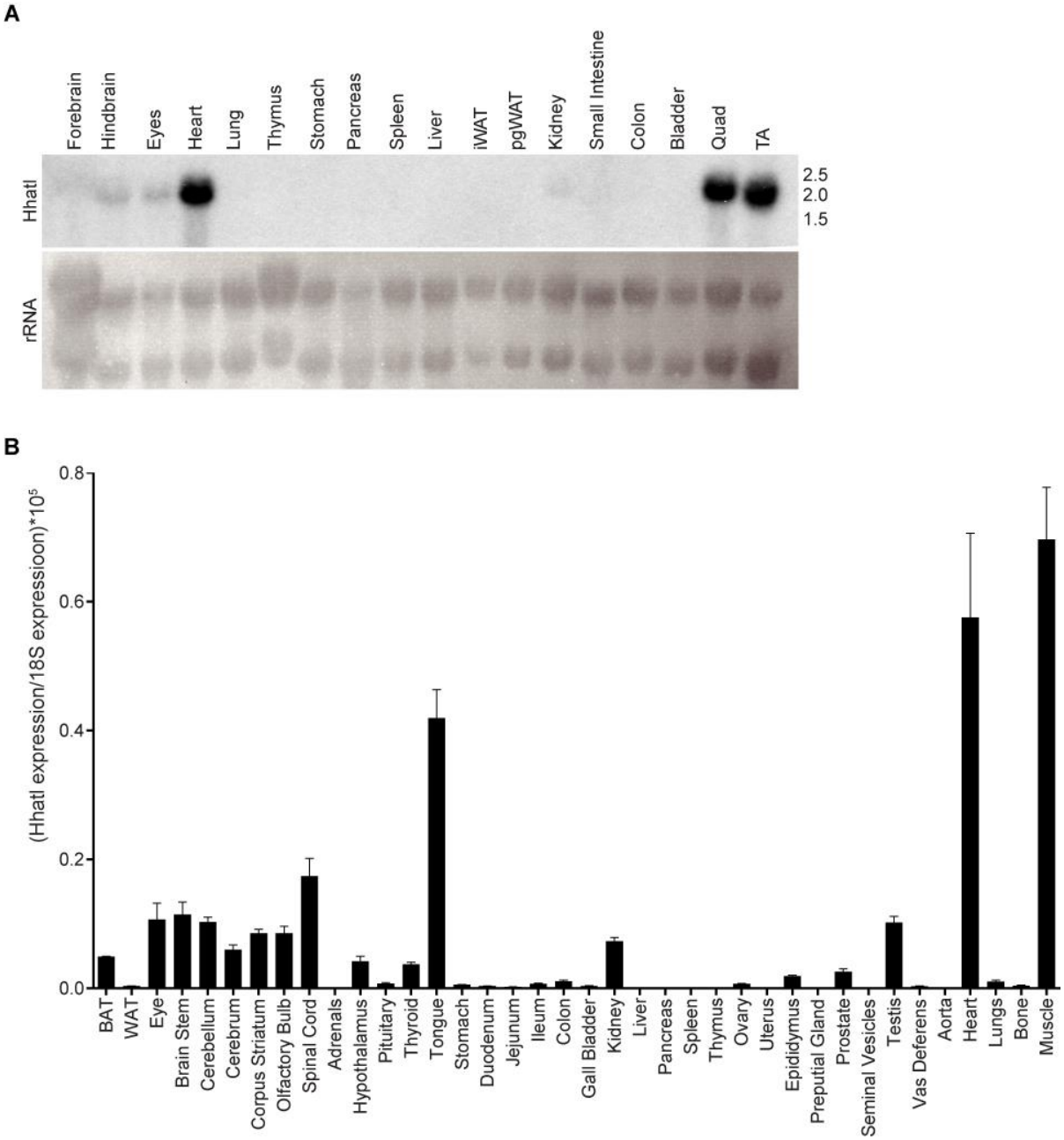

Figure 4.4. *Hhatl* expression is enriched in heart and skeletal muscle. (**A)** Northern blot on adult mouse tissues for *Hhatl* and ribosomal RNA (rRNA) shows expression in heart and skeletal muscles (quadriceps and TA [tibialis anterior]). iWAT ang pgWAT are inguinal and perigonadal white adipose tissues, respectively. There is also some expression in the hindbrain, eyes, and kidney. (**B**) qPCR analysis of *Hhatl* expression in multiple C57BL/6 adult tissues shows high enrichment for tongue (largely composed of skeletal muscle), skeletal muscle, and heart. There is also substantial expression in neural tissues. “BAT” and “WAT” are brown adipose tissue and white adipose tissue, respectively. Values are normalized to 18S ribosomal RNA. Data are presented as mean ± SEM.

Generating* Hhatl *conditionally targeted mice.

To disrupt expression of *Hhatl*, we decided to target the locus using the conventional knockout-approach described in Chapter Two. The targeting vector and Southern blot strategy are shown in Figure 4.5. Mice heterozygous and homozygous for the targeted allele are written as *Hhatl*$^{+/lacZ}$ and *Hhatl*$^{lacZ/lacZ}$, respectively. This particular allele is referred to as the "knockout first allele" because the presence of IRES-lacZ disrupts endogenous expression of *Hhatl*. See Figure 2.38 for the knockout first strategy originally described by KOMP.

Global deletion of* Hhatl *results in growth defects and lethality.

To generate mice globally deficient in *Hhatl*, we intercrossed *Hhatl*$^{+/lacZ}$ mice to generate *Hhatl*$^{lacZ/lacZ}$ mice. We confirmed take out of *Hhatl* transcript in both heart and skeletal muscle (Figure 4.6A). We did not observe any lacZ production in *Hhatl* expressing tissues (data not shown). We believe this is due to the instability of the *Hhatl* transcript following knock-in of the *lacZ* reporter that forces exon 2 of *Hhatl* to splice with *IRES-lacZ* (see Figure 4.5). Without the *IRES-lacZ* containing transcript, no lacZ is produced and hence, our negative lacZ staining result.

Globally deleted *Hhatl* mice displayed growth defects, although the severity in growth defects was variable (Figure 4.6, B and C). Some mice died before 27 days of age, but a more thorough analysis of lethality is required (data not shown).

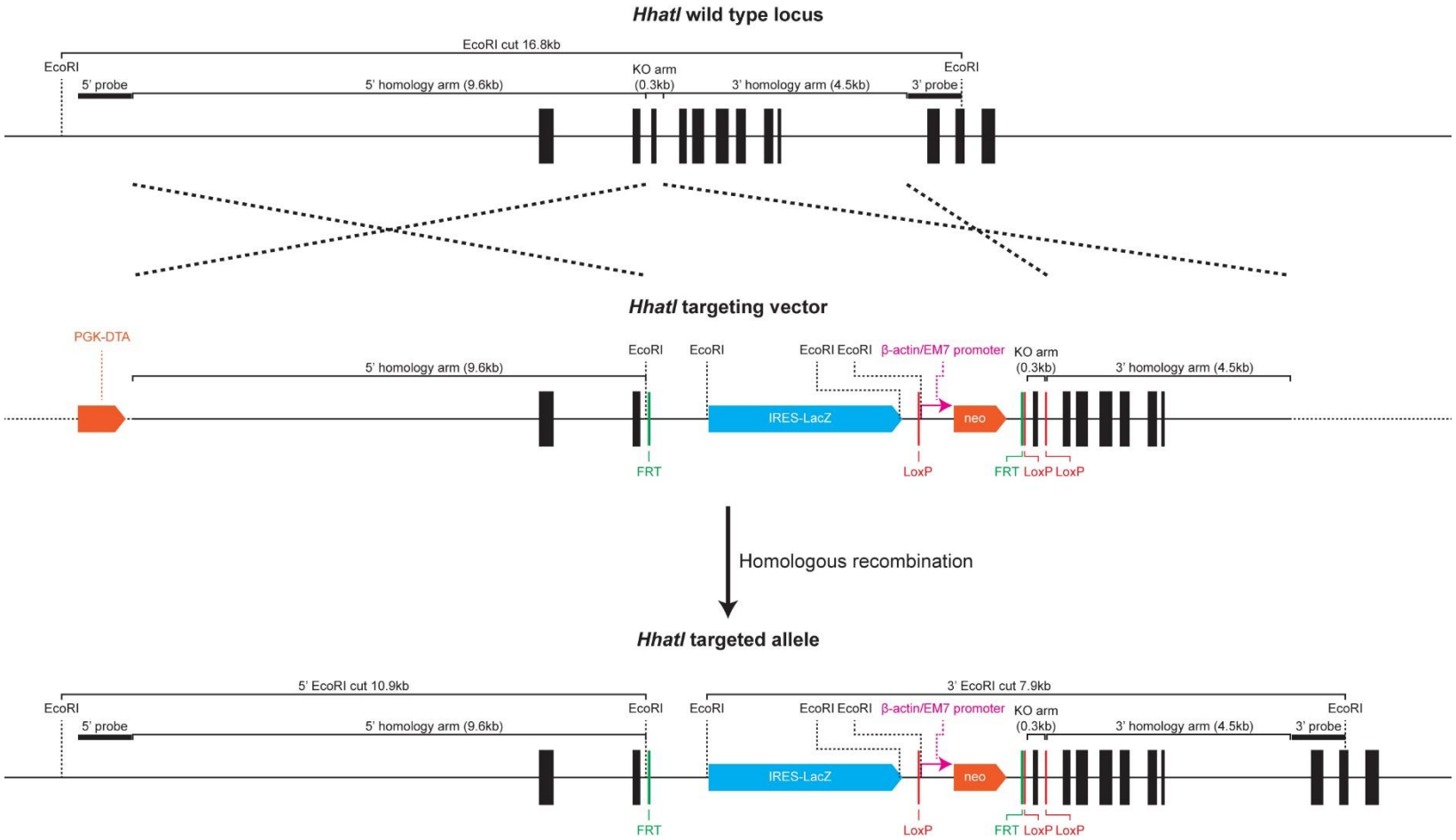

Figure 4.5. Knockout-first conditional targeting strategy. Targeting strategy used to generate knockout-first *Hhatl* mice. Black boxes represent exons. Smaller rectangles with tapered triangle ends represent coding sequences for DTA (orange, left), neo (orange, right), and lacZ (cyan). DTA is driven by the PGK promoter, neo by a hybrid β-actin/EM7 promoter, and lacZ by the endogenous *Hhatl* promoter. EcoRI restriction site was used for Southern screening strategy and the expected cut sizes are shown following targeting.

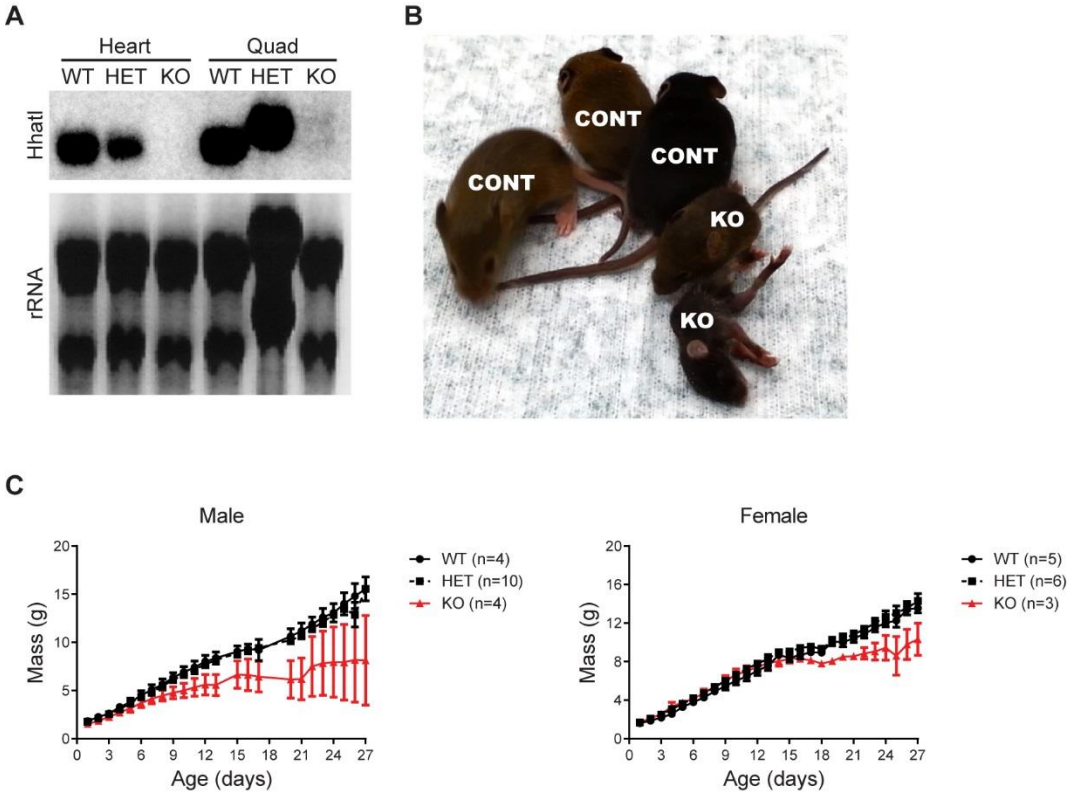

Figure 4.6. Global loss of *Hhatl* causes growth defects. (**A**) Northern blot analysis of heart and quadriceps (Quad) tissues from *Hhatl*$^{+/+}$ (WT), *Hhatl*$^{+/lacZ}$ (HET), and *Hhatl*$^{lacZ/lacZ}$ (KO) mice for *Hhatl* expression. KO mice show complete loss of *Hhatl* transcript. Ribosomal RNA (rRNA) is shown as a loading control. (**B**) Image of 2 to 3 week old KO mice shows that they are smaller and more emaciated in appearance compared to control mice (CONT; either WT or HET mice). (**C**) Growth curves of male and female WT, HET, and KO mice up to 27 days of age shows that KO mice are smaller than control littermates at later ages.

Conditional deletion of Hhatl *from heart or skeletal muscle does not result in growth defects or lethality at base line.*

Given the high level of enrichment of *Hhatl* in heart and skeletal muscle, we questioned whether conditional deletion of *Hhatl* from either tissue would be sufficient to recapitulate the phenotype we observed in globally deleted *Hhatl* mice. We generated a conditional *Hhatl* allele by crossing a *Hhatl*$^{+/lacZ}$ mouse with a transgenic mouse line containing FLP recombinase (101). This excised the lacZ cassette while retaining the conditional loxP sites

flanking exon 3 (Figure 4.7A). Mice heterozygous and homozygous for the conditional allele are referred to as *Hhatl*$^{+/fl}$ and *Hhatl*$^{fl/fl}$, respectively. We deleted *Hhatl* specifically in heart and skeletal muscle using αMHC-Cre and myogenin-Cre, generated previously, and we verified tissue specific deletion in both of these tissues (Figure 4.7B) (102, 103). However, we did not observe any growth defects or lethality in heart or skeletal muscle specific loss of *Hhatl* (data not shown).

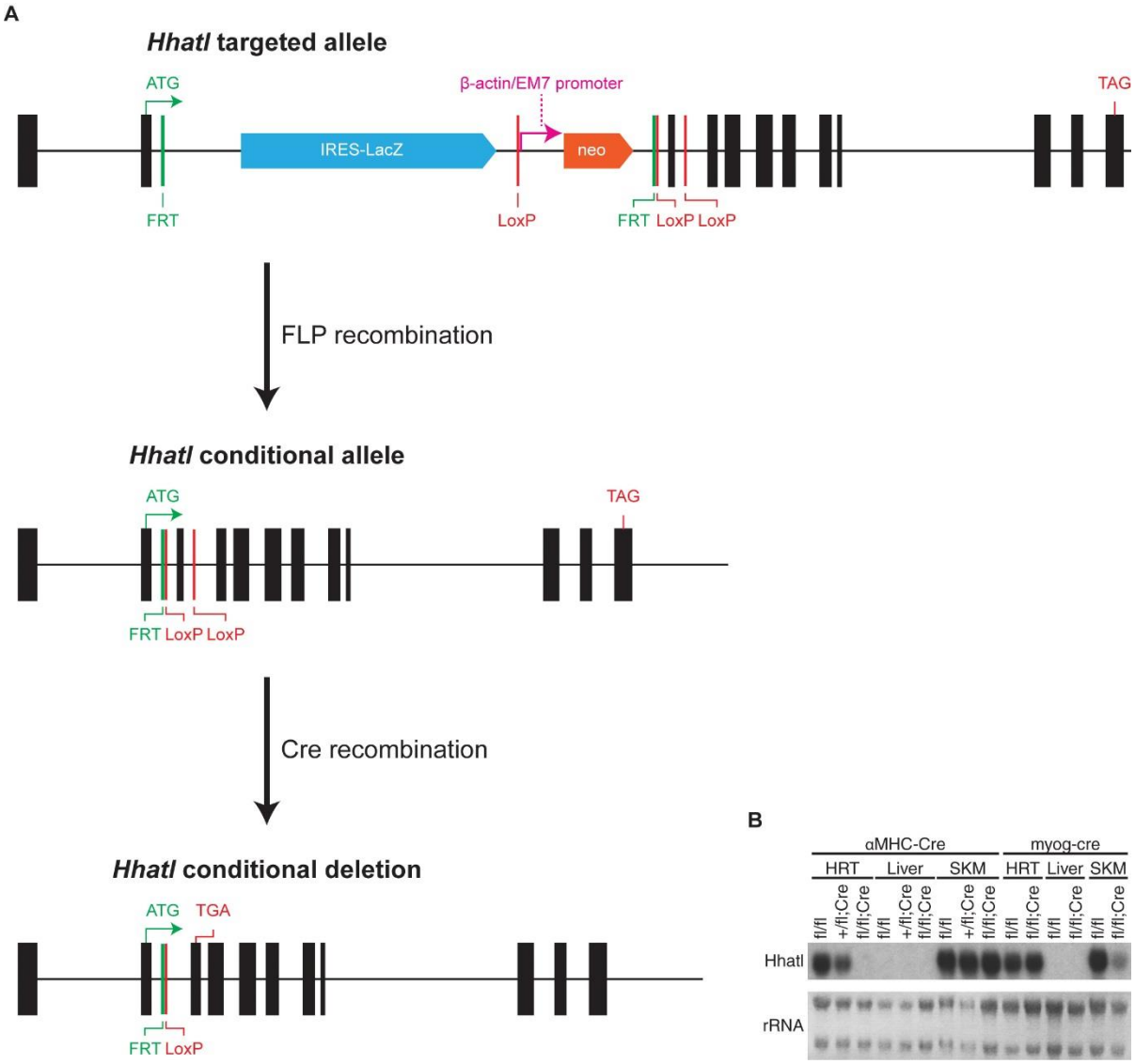

Figure 4.7. Heart and skeletal muscle specific deletion of *Hhatl*. (**A**) Generating the conditional allele and conditional deletion. Shown is a schematic view of the *Lmod3* locus with the knockout-first targeted allele as well as the endogenous start (green "ATG" with arrow) and stop codons (red "TAG"). Following FLP recombination, a conditional allele is generated with loxP sites flanking exon 3. Cre recombination results in deletion of exon 3 which causes a frame shift mutation with a premature stop codon in exon 4 (red "TGA"). (**B**) Northern blot analysis of heart (HRT), liver (negative control), and skeletal muscle (SKM) for *Hhatl* expression. *Hhatl* expression is specifically deleted in the heart and skeletal muscle for αMHC-Cre and myog-cre, resptively. Ribosomal RNA (rRNA) is shown as a loading control.

DISCUSSION AND FUTURE DIRECTIONS

Loss of *Hhatl* results in growth defects and lethality. It remains unclear what is the cause of the phenotype, but deletion from heart and/or muscle is not sufficient to recapitulate the phenotype of globally deleted *Hhatl*. Given the widespread expression of *Hhatl* in neural tissues, we believe that the phenotype is likely due to some effect on the central nervous system. To test this hypothesis, we are selectively deleting *Hhatl* from neural tissues using the pan-neuronal Syn1-Cre (104). If our phenotype repeats with this neuronal deletion, it would be interesting to test whether specific deletion of *Hhatl* from motor neurons using Hb9-cre, also results in a phenotype (105).

Additional work needs to be done to characterize the expression of *Hhatl* during development as well as its expression in other tissues. For development, qPCR analysis of select tissues should be analyzed from embryonic to postnatal development. As for expression analysis in other tissues, it would be ideal to knock-in a reporter, such as tdTomato, which would allow us to visualize *Hhatl* expression in individual cell populations. Given the ease of gene targeting with TALEN technology, generation of a *Hhatl* reporter mouse line should be considered.

Finally, the molecular function of Hhatl should also be analyzed. How to do this will become clear once we establish the phenotype of the *Hhatl* knockout mice. Broadly speaking, we need to first ascertain whether Hhatl is involved with the acylation of proteins or lipids. Then, we need to identify the specific targets of Hhatl and identify the substrate Hhatl uses to modify its targets. Combined with the phenotype, we can place Hhatl into a biologically relevant molecular pathway that will elucidate its function.

METHODS

Generating the Hhatl *conditional targeting vector*.

To generate the *Hhatl* conditional targeting vector, we used the recombineering approach discussed previously in Chapter Two. Initially, we retrieved a 14.5kb fragment containing our *Hhatl* fragment of interest which we then attempted to modify with a knockout cassette. However, one problem that we did not anticipate was that when we retrieved our 14.5kb fragment, it was inserted into a high-copy vector. Thus, when we attempted to modify the retrieved vector, all the bacteria we obtained contained mixed constructs that were modified and unmodified. Despite trying to extract DNA and re-transforming them into bacteria at very limiting amounts, we were not able to eliminate this mixing. Thus, we took an alternative approach in which we first inserted the knockout cassette into a BAC, which is in a low-copy vector backbone, and then retrieved that modified sequence from the BAC. We were successful with this method and will discuss it in more detail below.

The first step to our recombineering approach to generate the *Hhatl* targeting vector was to generate the knockout cassette. Again, we chose the knockout-first strategy first discussed in Chapter Two. All sequences were amplified from the bMQ302P07 BAC clone, mentioned previously. First, we cloned out the *Hhatl* knockout arm which contained exon 3 and fragments of introns 2 and 3, using the following primers: forward – ggcacagtttcaaagacccctgcagcc (with added 5' EcoRI and BsrGI sites, not shown), reverse – acaaaatgagccggaaggtcttgaagttcaaggc (with added 5' XmaI and loxP sites, not shown) into the EcoRI and XmaI sites of pBluescript II SK(+). Next, we cloned the 5' and 3' mini homology arms for the KO cassette and inserted them into the vector containing the *Hhatl* knockout arm. To clone the 5' mini homology arm we used the following primer pair: forward –

tggtgtcccaaacttgtcagcccatcagagag (with added 5' ClaI site, not shown), reverse – caatccggggcctagaggatcctcaggg (with added 5' EcoRI site, not shown). To clone the 3' mini homology arm we used the following primer pair: forward – acaagctagaccgctggttcctgccttccag (with added 5' XmaI site, not shown), reverse – ctgggataggtgtcccatggcattcaggacag (with added 5' SpeI site, not shown). We subcloned the 5' and 3' mini arms to the vector containing the *Hhatl* knockout arm using ClaI/EcoRI and XmaI/SpeI, respectively. Then, we removed the KOMP knockout cassette containing the added EM7 primer by digestion with BsrGI which was subsequently ligated into the BsrGI site of the *Hhatl* knockout arm. This final product is referred to as the *Hhatl* KO cassette.

Next, we assembled the *Hhatl* retrieval vector. First, we cloned the 5' and 3' homology arms that flanked the 14.5kb region of interest (nucleotides 121785651 to 121800110 NCBI reference sequence NC_000075.6; on minus strand). For the 5' mini homology arm, we used the following primer pair: forward – ttctatcctgtggtccaagatgcctgaagggc (with added 5' HindIII site, not shown), reverse – tgagctaaaacggcctcaggaaacctccagc (with added 5' ClaI site, not shown). For the 3' mini homology arm, we used the following primer pair: forward – tgaggggaggaatgtagggtacgaagtcaggg (with added 5' ClaI site, not shown), reverse - tccaaggcacaagttctatcagctctgctggg (with added 5' HindIII site, not shown). Next, we subcloned the 5' mini homology arm into the vector containing the 3' mini homology arm by cutting the 5' mini homology arm with HindIII, blunting, and then cutting with ClaI which was ligated into the 3' homology arm vector cut with SalI, blunted, and then cut with ClaI. Then, we subcloned the pgk-DTA cassette mentioned previously in Chapter Two, into the KpnI and XhoI sites of the vector containing the 5' and 3' mini homology arms. Finally, we inserted a PacI restriction site using the same method described in Chapter Two. This final retrieval vector is referred to as HhatlRetPacI.

After assembling the necessary constructs, we linearized the *Hhatl* KO cassette with SpeI and electroporated it into electrocompetent DY380 cells containing the bMQ302P07 BAC, as described in Chapter Two. We selected for bacteria for kanamycin resistance and performed a PCR screen to find positive recombinants (strategy not shown). Ideally, one would perform a diagnostic restriction digest to ensure that there were not any random recombinations that occurred in the BAC. However, we decided to delay this diagnostic digestion until after we retrieved the 14.5+kb fragment ("+" because the modification increased the size of the retrieved fragment) to simplify the banding pattern we were looking for.

Next, we retrieved the 14.5+kb fragment by linearizing our HhatlRetPacI retrieval vector with ClaI and then electroporating it into electrocompetent DY380 cells containing our bMQ302P07 BAC plus the region modified by the *Hhatl* KO cassette. We selected for ampicillin resistance and initially screened bacteria by a PCR strategy. Then, we performed two individual diagnostic restriction digest screens on positive recombinants with HindIII and NdeI. Interestingly, many clones that were positive by PCR screening, were negative by the diagnostic restriction digests. In addition, of the 5 clones confirmed by restriction digest screen, only one clone did not have any additional fainter bands that indicated minor recombination products. Thus, it is important to screen clones by restriction digest and to screen many clones to find one that does not have contaminating random recombinations. This final assembled targeting vector is referred to as the *Hhatl* targeting vector.

***Deriving* Hhatl *conditionally targeted mice*.**

The *Hhatl* targeting vector was linearized, electroporated, and screened as described in Chapter Two. Four targeted clones were obtained from a single 96-well plate of ES cells, 1A6, 1A9, 1G5, and 1H6. Initially, 1A9 and 1G5 were used to generate chimeras, but 1A9

failed to transmit the chimeric coat color to the next generation. 1G5, on the other hand, transmitted the coat color, but not the targeted allele. Referring back to our Southern blot, we saw that there was a large discrepancy in the intensity of the wildtype and targeted bands. Thus, there was likely an issue with the 1G5 clone. We did a third, and final, injection with the 1A6 clone and were able to successfully derive targeted mice. Southern blots of each clone is shown in Figure 4.8, A and B.

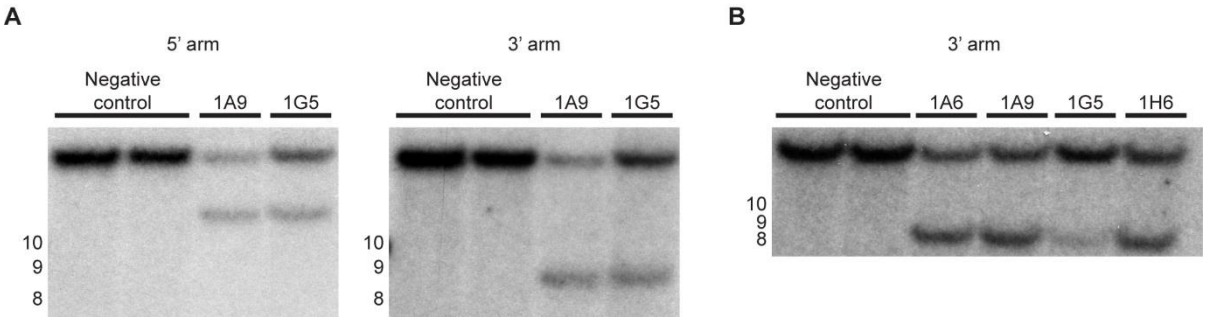

Figure 4.8. Validation of *Hhatl* targeted ES cell clones. (**A, B**) Southern blot analysis of (**A**) the 5' and 3' arm of 1A9 and 1G5 and (**B**) 3' arm of 1A6, 1A9, 1G5, and 1H6. Note the discrepancy in the relative intensity of the wild type (top) band compared to the targeted band for 1G5.

Southern blot analysis and genotyping of targeted mice.

Southern blots were performed as mentioned in Chapter Two except genomic DNA was digested with EcoRI. The 5' probe was amplified using the following primers: forward – ccgccttgtgtcagctcagcc and reverse – acacccaagagaggaacttgggc. The 3' probe was amplified using the following primers: forward – tgaggggaggaatgtagggtacgaagtcaggg and reverse – tccaaggcacaagttctatcagctctgctggg.

To genotype Hhatl targeted mice, the presence of the lone loxP site (3' of the knockout arm) was checked using the following primers: forward – CGT CCT TCC CTA CTC TAT TCT TGC TG and reverse – CTG GAA GGC AGG AAC CAG CG. In the absence of the loxP site (wild type allele) the size of the PCR product is 123bp while in the presence of the loxP site,

the size is 163bp. If mice were conditionally deleted with CAG-Cre, the following primers were used to check for deletion: forward – GGC CAG AAT CTT GGA GGC TGC and reverse – CTG GAA GGC AGG AAC CAG CG (same as above). The size of the wild type allele is 412bp, the flox'ed allele (loxP site present) is 608bp, and the size of the Cre recombined allele is 213bp.

Northern blot analysis.

Northern blot analysis of *Hhatl* was routinely performed as described in Chapter Two. The full length coding region of *Hhatl* was used as a probe.

CHAPTER FIVE

CONCLUDING REMARKS

The post-genomic era of science has generated vast databases full of annotated genes, but the majority of these have, as of yet, no known function. The classical hypothesis-driven approach to science that has been invaluable for studying specific and binary questions is too cumbersome for studying proteins of unknown function. To extricate ourselves from this quagmire, we took a discovery-based approach and simply asked, “What is the molecular function of Klhl40?” We did so without any presuppositions aside from assuming its role in muscle biology. However, without a clear question, it became exceedingly difficult to choose a direction for our studies which betrayed the brashness of our approach. We were fortunate to have the resources to generate a genetic deletion of *Klhl40* in mice and characterize the ensuing phenotype. In retrospect, the success of the Klhl40 study came largely from sheer luck of having a baseline phenotype in Klhl40 knockout mice. Without this phenotype, we would not have been able to describe the molecular function of Klhl40. But, perhaps, sometimes it takes such a cavalier attitude in order to break into new frontiers of scientific discovery that unlocks new avenues to explore. Were it not for the study of Klhl40, we would never had pursued Lmod3 nor Hhatl.

In this section, I will briefly discuss the broader and more speculative implications of our findings from the previous three chapters. I hope the reader will allow me to break from the usual disembodied and dispassionate analysis, which is typically demanded in a scientific work, and allow me, for once, to engage in some (meaningless) rhetoric. More concrete discussions of results can be found in the respective “Discussion” sections of each of the previous chapters.

Klhl40 and Lmod3 in nemaline myopathy

We found that loss of Klhl40 in mice results in a nemaline myopathy-like phenotype which correlates with findings in KLHL40 deficient human patients (17). Our molecular work reveals that Klhl40 serves as a stability factor for Neb, a protein frequently implicated in nemaline myopathy, as well as for Lmod3, a putative, muscle-specific actin nucleation factor (31-33). Incredibly, Lmod3 and Neb are the most down-regulated protein in the skeletal muscle proteome of Klhl40 deficient mice. We go on to show that specific deletion of Lmod3 is sufficient to result in a skeletal myopathy in of itself suggesting that loss of Lmod3 in the Klhl40 deficient background plays a major role in the nemaline myopathy-like phenotype.

Despite our findings, the exact molecular function of Klhl40 remains unclear. Certainly, we show that Klhl40 promotes Neb and Lmod3 protein levels, but the nature of this stabilization is unknown. A potentially interesting mechanism could be that Klhl40 forms a complex with actin, Lmod3, and Neb and enhances their respective functions. Klhl40 co-immunoprecipitates with all three aforementioned molecules, as shown by our tandem affinity purification experiment (see Chapter Two). Perhaps another mechanism could be that Klhl40 potentiates the actin polymerization function by increasing Lmod3's affinity for actin in an allosteric manner. Thus, a loss of Klhl40 would result in decreased Lmod3 binding of actin which could result in its degradation. It is possible that Klhl40 also imparts increased actin-binding affinity for Neb as well. Testing these hypotheses will require more rigorous biochemical approaches.

Ultimately, we wish to delineate the function of Klhl40 so we might somehow substitute for its loss in KLHL40 patients by pharmacologic treatment. The potential use of proteasome inhibitors has already been discussed in Chapter Two. However, we show in Chapter Three

that mere overexpression of Lmod3 does not mitigate the Klhl40 KO phenotype. Thus, a simple proteasome inhibitor treatment may not be sufficient.

Overall, aside from the success of characterizing the function of a novel muscle-specific protein, the Klhl40 study serves as a nidus for new directions to explore in striated muscle biology. In addition, the link between Klhl40, Lmod3, and actin dynamics has also allowed us to return to some of our more seminal work in describing the MRTF-SRF transcriptional network. Thus, our findings with Klhl40, and undoubtedly our future findings with Lmod3, bring us one step closer to a more comprehensive understanding of sarcomere function and regulation and muscle biology as a whole.

Hhatl

It was paranoid determination to find the true cause of the Klhl40 phenotype that led to the origin of the Hhatl project. The 50% loss of *Hhatl* in the skeletal muscle of Klhl40 knockout mice was highly unlikely to be the cause of Klhl40 knockout phenotype, but this hypothesis had to be directly tested. Thus, we not only rescued the Klhl40 knockout phenotype using *MCK-Klhl40*, but we also generated a completely separate targeted *Hhatl* knockout. Global deletion of *Hhatl* results in a lethal phenotype, but one that is not due to loss of *Hhatl* in skeletal muscle or heart, as shown by the lack of phenotype in skeletal muscle or heart-specific deletions of *Hhatl* in mice.

As discussed in Chapter Four, Hhatl is an MBOAT protein that likely has some role in protein acylation. Given its widespread expression in neural tissues and the lack of a lethal phenotype with heart or skeletal muscle deletion of *Hhatl*, we speculate that Hhatl likely has an important role in neurons or surrounding support cells. No work has been done to

characterize the neural tissues in Hhatl knockout mice, but it is possible that Hhatl may be involved in the post-translational modification of some factor vital for neural function. Loss of Hhatl secondarily affects this putative factor resulting in a generalized decrease of neural function. This manifests as a general failure to thrive due to metabolic as well as locomotor defects. However, much work remains to test this hypothesis, and it will be likely heavily modified in the future as we better characterize the Hhatl knockout phenotype.

Hhatl is most highly expressed in heart and skeletal muscle, but, incredibly, deletion of *Hhatl* from these tissues results in no obvious baseline phenotype. Based on our speculation that Hhatl control post-translational modification of a secreted factor, it may be necessary to stress cardiac and skeletal muscle tissues to elicit a phenotype in conditionally deleted Hhatl knockout mice. We will need to explore a battery of metabolic and mechanical stresses on cardiac and skeletal muscle to see whether we can glean any function for Hhatl in these tissues.

Conclusion

One of the most difficult aspects of a scientific project is to determine whether the potential outcome of the project justifies the time that must be invested to complete it. This difficulty was especially apparent for the discovery-based Klhl40 project which initially started without a hypothesis and broadly broached the function of Klhl40 in striated muscle. However, it was this open-ended approach that ultimately allowed us to branch out into exploring the novel muscle proteins Lmod3 and Hhatl, while also telling a meaningful story about Klhl40's function. In the future, it is advisable for anyone pursuing a discovery-based project to analyze a variety of genes, proteins, *et cetera* to increase the chances of uncovering a novel protein or transcript with an important and testable function. Generally speaking, we can never

guarantee success, but we can mitigate failure. And in some cases, like my own, luck and resilience paves the way to unexplored frontiers.

Bibliography

1. Hill, J.A., and Olson, E.N. 2012. Chapter 1 - An Introduction to Muscle. In *Muscle*. J.A. Hill, and E.N. Olson, editors. Boston/Waltham: Academic Press. 3-9.

2. Hall, C.E., Jakus, M.A., and Schmitt, F.O. 1946. An investigation of cross striations and myosin filaments in muscle. *Biol Bull* 90:32-50.

3. Huxley, H.E. 1953. Electron microscope studies of the organisation of the filaments in striated muscle. *Biochim Biophys Acta* 12:387-394.

4. Huxley, H., and Hanson, J. 1954. Changes in the cross-striations of muscle during contraction and stretch and their structural interpretation. *Nature* 173:973-976.

5. Craig, R., and Padrón, R. 2004. Molecular structure of the sarcomere. *Myology. 3rd ed. Myology. 3rd ed. New York: McGrawHill*.

6. Udd, B. 2008. Third Filament Diseases. In *The Sarcomere and Skeletal Muscle Disease*. N. Laing, editor: Springer New York. 99-115.

7. Franzini-Armstrong, C., and Lee Sweeney, H. 2012. Chapter 58 - The Contractile Machinery of Skeletal Muscle. In *Muscle*. J.A. Hill, and E.N. Olson, editors. Boston/Waltham: Academic Press. 823-840.

8. Greenfield, J.G., Cornman, T., and Shy, G.M. 1958. The prognostic value of the muscle biopsy in the floppy infant. *Brain* 81:461-484.

9. Shy, G.M., Engel, W.K., Somers, J.E., and Wanko, T. 1963. Nemaline Myopathy. A New Congenital Myopathy. *Brain* 86:793-810.

10. Laing, N.G., Wilton, S.D., Akkari, P.A., Dorosz, S., Boundy, K., Kneebone, C., Blumbergs, P., White, S., Watkins, H., Love, D.R., et al. 1995. A mutation in the alpha tropomyosin gene TPM3 associated with autosomal dominant nemaline myopathy NEM1. *Nat Genet* 10:249.

11. Lehtokari, V.L., Pelin, K., Sandbacka, M., Ranta, S., Donner, K., Muntoni, F., Sewry, C., Angelini, C., Bushby, K., Van den Bergh, P., et al. 2006. Identification of 45 novel mutations in the nebulin gene associated with autosomal recessive nemaline myopathy. *Hum Mutat* 27:946-956.

12. Nowak, K.J., Wattanasirichaigoon, D., Goebel, H.H., Wilce, M., Pelin, K., Donner, K., Jacob, R.L., Hubner, C., Oexle, K., Anderson, J.R., et al. 1999.

Mutations in the skeletal muscle alpha-actin gene in patients with actin myopathy and nemaline myopathy. *Nat Genet* 23:208-212.

13. Donner, K., Ollikainen, M., Ridanpaa, M., Christen, H.J., Goebel, H.H., de Visser, M., Pelin, K., and Wallgren-Pettersson, C. 2002. Mutations in the beta-tropomyosin (TPM2) gene--a rare cause of nemaline myopathy. *Neuromuscul Disord* 12:151-158.

14. Johnston, J.J., Kelley, R.I., Crawford, T.O., Morton, D.H., Agarwala, R., Koch, T., Schaffer, A.A., Francomano, C.A., and Biesecker, L.G. 2000. A novel nemaline myopathy in the Amish caused by a mutation in troponin T1. *Am J Hum Genet* 67:814-821.

15. Agrawal, P.B., Greenleaf, R.S., Tomczak, K.K., Lehtokari, V.L., Wallgren-Pettersson, C., Wallefeld, W., Laing, N.G., Darras, B.T., Maciver, S.K., Dormitzer, P.R., et al. 2007. Nemaline myopathy with minicores caused by mutation of the CFL2 gene encoding the skeletal muscle actin-binding protein, cofilin-2. *Am J Hum Genet* 80:162-167.

16. Sambuughin, N., Yau, K.S., Olive, M., Duff, R.M., Bayarsaikhan, M., Lu, S., Gonzalez-Mera, L., Sivadorai, P., Nowak, K.J., Ravenscroft, G., et al. 2010. Dominant mutations in KBTBD13, a member of the BTB/Kelch family, cause nemaline myopathy with cores. *Am J Hum Genet* 87:842-847.

17. Ravenscroft, G., Miyatake, S., Lehtokari, V.L., Todd, E.J., Vornanen, P., Yau, K.S., Hayashi, Y.K., Miyake, N., Tsurusaki, Y., Doi, H., et al. 2013. Mutations in KLHL40 are a frequent cause of severe autosomal-recessive nemaline myopathy. *Am J Hum Genet* 93:6-18.

18. Gupta, V.A., Ravenscroft, G., Shaheen, R., Todd, E.J., Swanson, L.C., Shiina, M., Ogata, K., Hsu, C., Clarke, N.F., Darras, B.T., et al. 2013. Identification of KLHL41 Mutations Implicates BTB-Kelch-Mediated Ubiquitination as an Alternate Pathway to Myofibrillar Disruption in Nemaline Myopathy. *Am J Hum Genet*.

19. Shimomura, C., and Nonaka, I. 1989. Nemaline myopathy: comparative muscle histochemistry in the severe neonatal, moderate congenital, and adult-onset forms. *Pediatr Neurol* 5:25-31.

20. Nance, J.R., Dowling, J.J., Gibbs, E.M., and Bonnemann, C.G. 2012. Congenital myopathies: an update. *Curr Neurol Neurosci Rep* 12:165-174.

21. Stogios, P.J., and Prive, G.G. 2004. The BACK domain in BTB-kelch proteins. *Trends Biochem Sci* 29:634-637.

22. Bennett, E.J., Rush, J., Gygi, S.P., and Harper, J.W. 2010. Dynamics of cullin-RING ubiquitin ligase network revealed by systematic quantitative proteomics. *Cell* 143:951-965.

23. Emanuele, M.J., Elia, A.E., Xu, Q., Thoma, C.R., Izhar, L., Leng, Y., Guo, A., Chen, Y.N., Rush, J., Hsu, P.W., et al. 2011. Global identification of modular cullin-RING ligase substrates. *Cell* 147:459-474.

24. Zhang, D.D., Lo, S.C., Sun, Z., Habib, G.M., Lieberman, M.W., and Hannink, M. 2005. Ubiquitination of Keap1, a BTB-Kelch substrate adaptor protein for Cul3, targets Keap1 for degradation by a proteasome-independent pathway. *J Biol Chem* 280:30091-30099.

25. Angers, S., Thorpe, C.J., Biechele, T.L., Goldenberg, S.J., Zheng, N., MacCoss, M.J., and Moon, R.T. 2006. The KLHL12-Cullin-3 ubiquitin ligase negatively regulates the Wnt-beta-catenin pathway by targeting Dishevelled for degradation. *Nat Cell Biol* 8:348-357.

26. Sumara, I., Quadroni, M., Frei, C., Olma, M.H., Sumara, G., Ricci, R., and Peter, M. 2007. A Cul3-based E3 ligase removes Aurora B from mitotic chromosomes, regulating mitotic progression and completion of cytokinesis in human cells. *Dev Cell* 12:887-900.

27. Lee, Y.R., Yuan, W.C., Ho, H.C., Chen, C.H., Shih, H.M., and Chen, R.H. 2010. The Cullin 3 substrate adaptor KLHL20 mediates DAPK ubiquitination to control interferon responses. *EMBO J* 29:1748-1761.

28. Jin, L., Pahuja, K.B., Wickliffe, K.E., Gorur, A., Baumgartel, C., Schekman, R., and Rape, M. 2012. Ubiquitin-dependent regulation of COPII coat size and function. *Nature* 482:495-500.

29. Shibata, S., Zhang, J., Puthumana, J., Stone, K.L., and Lifton, R.P. 2013. Kelch-like 3 and Cullin 3 regulate electrolyte homeostasis via ubiquitination and degradation of WNK4. *Proc Natl Acad Sci U S A* 110:7838-7843.

30. Rastogi, N., and Mishra, D.P. 2012. Therapeutic targeting of cancer cell cycle using proteasome inhibitors. *Cell Div* 7:26.

31. Wallgren-Pettersson, C., Sewry, C.A., Nowak, K.J., and Laing, N.G. 2011. Nemaline myopathies. *Semin Pediatr Neurol* 18:230-238.

32. Chereau, D., Boczkowska, M., Skwarek-Maruszewska, A., Fujiwara, I., Hayes, D.B., Rebowski, G., Lappalainen, P., Pollard, T.D., and Dominguez, R. 2008. Leiomodin is an actin filament nucleator in muscle cells. *Science* 320:239-243.

33. Nanda, V., and Miano, J.M. 2012. Leiomodin 1, a new serum response factor-dependent target gene expressed preferentially in differentiated smooth muscle cells. *J Biol Chem* 287:2459-2467.

34. Gray, P.A., Fu, H., Luo, P., Zhao, Q., Yu, J., Ferrari, A., Tenzen, T., Yuk, D.I., Tsung, E.F., Cai, Z.H., et al. 2004. Mouse brain organization revealed through direct genome-scale TF expression analysis. *Science* 306:2255-2257.

35. Sternberg, E.A., Spizz, G., Perry, W.M., Vizard, D., Weil, T., and Olson, E.N. 1988. Identification of upstream and intragenic regulatory elements that confer cell-type-restricted and differentiation-specific expression on the muscle creatine kinase gene. *Mol Cell Biol* 8:2896-2909.

36. Johnson, J.E., Wold, B.J., and Hauschka, S.D. 1989. Muscle creatine kinase sequence elements regulating skeletal and cardiac muscle expression in transgenic mice. *Mol Cell Biol* 9:3393-3399.

37. DiFranco, M., Quinonez, M., Capote, J., and Vergara, J. 2009. DNA transfection of mammalian skeletal muscles using in vivo electroporation. *J Vis Exp*.

38. Knight, P.J., and Trinick, J.A. 1982. Preparation of myofibrils. *Methods Enzymol* 85 Pt B:9-12.

39. Gokhin, D.S., Kim, N.E., Lewis, S.A., Hoenecke, H.R., D'Lima, D.D., and Fowler, V.M. 2012. Thin-filament length correlates with fiber type in human skeletal muscle. *Am J Physiol Cell Physiol* 302:C555-565.

40. Littlefield, R., and Fowler, V.M. 2002. Measurement of thin filament lengths by distributed deconvolution analysis of fluorescence images. *Biophys J* 82:2548-2564.

41. Bang, M.L., Li, X., Littlefield, R., Bremner, S., Thor, A., Knowlton, K.U., Lieber, R.L., and Chen, J. 2006. Nebulin-deficient mice exhibit shorter thin filament lengths and reduced contractile function in skeletal muscle. *J Cell Biol* 173:905-916.

42. Hill, J.A., and Olson, E.N. 2008. Cardiac plasticity. *N Engl J Med* 358:1370-1380.

43. Jensen, F.C., Girardi, A.J., Gilden, R.V., and Koprowski, H. 1964. Infection of Human and Simian Tissue Cultures with Rous Sarcoma Virus. *Proc Natl Acad Sci U S A* 52:53-59.

44. Gluzman, Y. 1981. SV40-transformed simian cells support the replication of early SV40 mutants. *Cell* 23:175-182.

45. Pappas, C.T., Bliss, K.T., Zieseniss, A., and Gregorio, C.C. 2011. The Nebulin family: an actin support group. *Trends Cell Biol* 21:29-37.

46. Johnson, E.S. 2002. Ubiquitin branches out. *Nat Cell Biol* 4:E295-298.

47. Witt, C.C., Burkart, C., Labeit, D., McNabb, M., Wu, Y., Granzier, H., and Labeit, S. 2006. Nebulin regulates thin filament length, contractility, and Z-disk structure in vivo. *EMBO J* 25:3843-3855.

48. Gokhin, D.S., Bang, M.L., Zhang, J., Chen, J., and Lieber, R.L. 2009. Reduced thin filament length in nebulin-knockout skeletal muscle alters isometric contractile properties. *Am J Physiol Cell Physiol* 296:C1123-1132.

49. Agrawal, P.B., Strickland, C.D., Midgett, C., Morales, A., Newburger, D.E., Poulos, M.A., Tomczak, K.K., Ryan, M.M., Iannaccone, S.T., Crawford, T.O., et al. 2004. Heterogeneity of nemaline myopathy cases with skeletal muscle alpha-actin gene mutations. *Ann Neurol* 56:86-96.

50. Crawford, K., Flick, R., Close, L., Shelly, D., Paul, R., Bove, K., Kumar, A., and Lessard, J. 2002. Mice lacking skeletal muscle actin show reduced muscle strength and growth deficits and die during the neonatal period. *Mol Cell Biol* 22:5887-5896.

51. Corbett, M.A., Robinson, C.S., Dunglison, G.F., Yang, N., Joya, J.E., Stewart, A.W., Schnell, C., Gunning, P.W., North, K.N., and Hardeman, E.C. 2001. A mutation in alpha-tropomyosin(slow) affects muscle strength, maturation and hypertrophy in a mouse model for nemaline myopathy. *Hum Mol Genet* 10:317-328.

52. Ravenscroft, G., Jackaman, C., Bringans, S., Papadimitriou, J.M., Griffiths, L.M., McNamara, E., Bakker, A.J., Davies, K.E., Laing, N.G., and Nowak, K.J. 2011. Mouse models of dominant ACTA1 disease recapitulate human disease and provide insight into therapies. *Brain* 134:1101-1115.

53. Nowak, K.J., Sewry, C.A., Navarro, C., Squier, W., Reina, C., Ricoy, J.R., Jayawant, S.S., Childs, A.M., Dobbie, J.A., Appleton, R.E., et al. 2007. Nemaline

myopathy caused by absence of alpha-skeletal muscle actin. *Ann Neurol* 61:175-184.

54. Bang, M.L., Caremani, M., Brunello, E., Littlefield, R., Lieber, R.L., Chen, J., Lombardi, V., and Linari, M. 2009. Nebulin plays a direct role in promoting strong actin-myosin interactions. *FASEB J* 23:4117-4125.

55. Chen, B., Retzlaff, M., Roos, T., and Frydman, J. 2011. Cellular strategies of protein quality control. *Cold Spring Harb Perspect Biol* 3:a004374.

56. Bowlin, K.M., Embree, L.J., Garry, M.G., Garry, D.J., and Shi, X. 2013. Kbtbd5 is regulated by MyoD and restricted to the myogenic lineage. *Differentiation*.

57. Canning, P., Cooper, C.D., Krojer, T., Murray, J.W., Pike, A.C., Chaikuad, A., Keates, T., Thangaratnarajah, C., Hojzan, V., Ayinampudi, V., et al. 2013. Structural basis for Cul3 protein assembly with the BTB-Kelch family of E3 ubiquitin ligases. *J Biol Chem* 288:7803-7814.

58. Ottenheijm, C.A., Buck, D., de Winter, J.M., Ferrara, C., Piroddi, N., Tesi, C., Jasper, J.R., Malik, F.I., Meng, H., Stienen, G.J., et al. 2013. Deleting exon 55 from the nebulin gene induces severe muscle weakness in a mouse model for nemaline myopathy. *Brain* 136:1718-1731.

59. Chandra, M., Mamidi, R., Ford, S., Hidalgo, C., Witt, C., Ottenheijm, C., Labeit, S., and Granzier, H. 2009. Nebulin alters cross-bridge cycling kinetics and increases thin filament activation: a novel mechanism for increasing tension and reducing tension cost. *J Biol Chem* 284:30889-30896.

60. Altschul, S.F., Madden, T.L., Schaffer, A.A., Zhang, J., Zhang, Z., Miller, W., and Lipman, D.J. 1997. Gapped BLAST and PSI-BLAST: a new generation of protein database search programs. *Nucleic Acids Res* 25:3389-3402.

61. Altschul, S.F., Wootton, J.C., Gertz, E.M., Agarwala, R., Morgulis, A., Schaffer, A.A., and Yu, Y.K. 2005. Protein database searches using compositionally adjusted substitution matrices. *Febs Journal* 272:5101-5109.

62. Valenzuela, D.M., Murphy, A.J., Frendewey, D., Gale, N.W., Economides, A.N., Auerbach, W., Poueymirou, W.T., Adams, N.C., Rojas, J., Yasenchak, J., et al. 2003. High-throughput engineering of the mouse genome coupled with high-resolution expression analysis. *Nat Biotechnol* 21:652-659.

63. Kim, M.S., Fielitz, J., McAnally, J., Shelton, J.M., Lemon, D.D., McKinsey, T.A., Richardson, J.A., Bassel-Duby, R., and Olson, E.N. 2008. Protein kinase D1

stimulates MEF2 activity in skeletal muscle and enhances muscle performance. *Mol Cell Biol* 28:3600-3609.

64. Naya, F.J., Mercer, B., Shelton, J., Richardson, J.A., Williams, R.S., and Olson, E.N. 2000. Stimulation of slow skeletal muscle fiber gene expression by calcineurin in vivo. *J Biol Chem* 275:4545-4548.

65. Wolff, A.V., Niday, A.K., Voelker, K.A., Call, J.A., Evans, N.P., Granata, K.P., and Grange, R.W. 2006. Passive mechanical properties of maturing extensor digitorum longus are not affected by lack of dystrophin. *Muscle Nerve* 34:304-312.

66. Nelson, B.R., Wu, F., Liu, Y., Anderson, D.M., McAnally, J., Lin, W., Cannon, S.C., Bassel-Duby, R., and Olson, E.N. 2013. Skeletal muscle-specific T-tubule protein STAC3 mediates voltage-induced Ca2+ release and contractility. *Proc Natl Acad Sci U S A* 110:11881-11886.

67. Schindelin, J., Arganda-Carreras, I., Frise, E., Kaynig, V., Longair, M., Pietzsch, T., Preibisch, S., Rueden, C., Saalfeld, S., Schmid, B., et al. 2012. Fiji: an open-source platform for biological-image analysis. *Nat Methods* 9:676-682.

68. Shelton, J.M., Lee, M.H., Richardson, J.A., and Patel, S.B. 2000. Microsomal triglyceride transfer protein expression during mouse development. *J Lipid Res* 41:532-537.

69. Millay, D.P., O'Rourke, J.R., Sutherland, L.B., Bezprozvannaya, S., Shelton, J.M., Bassel-Duby, R., and Olson, E.N. 2013. Myomaker is a membrane activator of myoblast fusion and muscle formation. *Nature* 499:301-305.

70. Simiczyjew, A., Malicka-Blaszkiewicz, M., and Nowak, D. 2013. [Functional diversification of cytoplasmic actin isoforms]. *Postepy Biochem* 59:285-294.

71. Sharan, S.K., Thomason, L.C., Kuznetsov, S.G., and Court, D.L. 2009. Recombineering: a homologous recombination-based method of genetic engineering. *Nat Protoc* 4:206-223.

72. Carreira-Rosario, A., Scoggin, S., Shalaby, N.A., Williams, N.D., Hiesinger, P.R., and Buszczak, M. 2013. Recombineering homologous recombination constructs in Drosophila. *J Vis Exp*:e50346.

73. Skarnes, W.C., Rosen, B., West, A.P., Koutsourakis, M., Bushell, W., Iyer, V., Mujica, A.O., Thomas, M., Harrow, J., Cox, T., et al. 2011. A conditional

knockout resource for the genome-wide study of mouse gene function. *Nature* 474:337-342.

74. Hoch, R.V., and Soriano, P. 2006. Context-specific requirements for Fgfr1 signaling through Frs2 and Frs3 during mouse development. *Development* 133:663-673.

75. Green, M.R., and Sambrook, J. 2012. *Molecular cloning: a laboratory manual*: Cold Spring Harbor Laboratory Press Cold Spring Harbor, New York:.

76. Molkentin, J.D., Lu, J.R., Antos, C.L., Markham, B., Richardson, J., Robbins, J., Grant, S.R., and Olson, E.N. 1998. A calcineurin-dependent transcriptional pathway for cardiac hypertrophy. *Cell* 93:215-228.

77. Kitamura, T., Onishi, M., Kinoshita, S., Shibuya, A., Miyajima, A., and Nolan, G.P. 1995. Efficient screening of retroviral cDNA expression libraries. *Proc Natl Acad Sci U S A* 92:9146-9150.

78. Horton, R.M. 1995. PCR-mediated recombination and mutagenesis. SOEing together tailor-made genes. *Mol Biotechnol* 3:93-99.

79. Gaj, T., Gersbach, C.A., and Barbas, C.F., 3rd. 2013. ZFN, TALEN, and CRISPR/Cas-based methods for genome engineering. *Trends Biotechnol* 31:397-405.

80. Boch, J., Scholze, H., Schornack, S., Landgraf, A., Hahn, S., Kay, S., Lahaye, T., Nickstadt, A., and Bonas, U. 2009. Breaking the code of DNA binding specificity of TAL-type III effectors. *Science* 326:1509-1512.

81. Moscou, M.J., and Bogdanove, A.J. 2009. A simple cipher governs DNA recognition by TAL effectors. *Science* 326:1501.

82. Christian, M., Cermak, T., Doyle, E.L., Schmidt, C., Zhang, F., Hummel, A., Bogdanove, A.J., and Voytas, D.F. 2010. Targeting DNA double-strand breaks with TAL effector nucleases. *Genetics* 186:757-761.

83. Zu, Y., Tong, X., Wang, Z., Liu, D., Pan, R., Li, Z., Hu, Y., Luo, Z., Huang, P., Wu, Q., et al. 2013. TALEN-mediated precise genome modification by homologous recombination in zebrafish. *Nat Methods* 10:329-331.

84. Cermak, T., Doyle, E.L., Christian, M., Wang, L., Zhang, Y., Schmidt, C., Baller, J.A., Somia, N.V., Bogdanove, A.J., and Voytas, D.F. 2011. Efficient design and

assembly of custom TALEN and other TAL effector-based constructs for DNA targeting. *Nucleic Acids Res* 39:e82.

85. Doyle, E.L., Booher, N.J., Standage, D.S., Voytas, D.F., Brendel, V.P., Vandyk, J.K., and Bogdanove, A.J. 2012. TAL Effector-Nucleotide Targeter (TALE-NT) 2.0: tools for TAL effector design and target prediction. *Nucleic Acids Res* 40:W117-122.

86. Ding, Q., Lee, Y.K., Schaefer, E.A., Peters, D.T., Veres, A., Kim, K., Kuperwasser, N., Motola, D.L., Meissner, T.B., Hendriks, W.T., et al. 2013. A TALEN genome-editing system for generating human stem cell-based disease models. *Cell Stem Cell* 12:238-251.

87. Fischer, R.S., and Fowler, V.M. 2003. Tropomodulins: life at the slow end. *Trends Cell Biol* 13:593-601.

88. Gokhin, D.S., and Fowler, V.M. 2011. Tropomodulin capping of actin filaments in striated muscle development and physiology. *J Biomed Biotechnol* 2011:103069.

89. Fritz-Six, K.L., Cox, P.R., Fischer, R.S., Xu, B., Gregorio, C.C., Zoghbi, H.Y., and Fowler, V.M. 2003. Aberrant myofibril assembly in tropomodulin1 null mice leads to aborted heart development and embryonic lethality. *J Cell Biol* 163:1033-1044.

90. Ono, Y., Schwach, C., Antin, P.B., and Gregorio, C.C. 2005. Disruption in the tropomodulin1 (Tmod1) gene compromises cardiomyocyte development in murine embryonic stem cells by arresting myofibril maturation. *Dev Biol* 282:336-348.

91. Kuwahara, K., Barrientos, T., Pipes, G.C., Li, S., and Olson, E.N. 2005. Muscle-specific signaling mechanism that links actin dynamics to serum response factor. *Mol Cell Biol* 25:3173-3181.

92. Kuwahara, K., Teg Pipes, G.C., McAnally, J., Richardson, J.A., Hill, J.A., Bassel-Duby, R., and Olson, E.N. 2007. Modulation of adverse cardiac remodeling by STARS, a mediator of MEF2 signaling and SRF activity. *J Clin Invest* 117:1324-1334.

93. Olson, E.N., and Nordheim, A. 2010. Linking actin dynamics and gene transcription to drive cellular motile functions. *Nat Rev Mol Cell Biol* 11:353-365.

94. Carlson, D.F., Tan, W., Lillico, S.G., Stverakova, D., Proudfoot, C., Christian, M., Voytas, D.F., Long, C.R., Whitelaw, C.B., and Fahrenkrug, S.C. 2012. Efficient TALEN-mediated gene knockout in livestock. *Proc Natl Acad Sci U S A* 109:17382-17387.

95. Bedell, V.M., Wang, Y., Campbell, J.M., Poshusta, T.L., Starker, C.G., Krug, R.G., 2nd, Tan, W., Penheiter, S.G., Ma, A.C., Leung, A.Y., et al. 2012. In vivo genome editing using a high-efficiency TALEN system. *Nature* 491:114-118.

96. Wefers, B., Panda, S.K., Ortiz, O., Brandl, C., Hensler, S., Hansen, J., Wurst, W., and Kuhn, R. 2013. Generation of targeted mouse mutants by embryo microinjection of TALEN mRNA. *Nat Protoc* 8:2355-2379.

97. Chang, S.C., and Magee, A.I. 2009. Acyltransferases for secreted signalling proteins (Review). *Mol Membr Biol* 26:104-113.

98. Chen, M.H., Li, Y.J., Kawakami, T., Xu, S.M., and Chuang, P.T. 2004. Palmitoylation is required for the production of a soluble multimeric Hedgehog protein complex and long-range signaling in vertebrates. *Genes Dev* 18:641-659.

99. Soejima, H., Kawamoto, S., Akai, J., Miyoshi, O., Arai, Y., Morohka, T., Matsuo, S., Niikawa, N., Kimura, A., Okubo, K., et al. 2001. Isolation of novel heart-specific genes using the BodyMap database. *Genomics* 74:115-120.

100. Abe, Y., Kita, Y., and Niikura, T. 2008. Mammalian Gup1, a homolog of Saccharomyces cerevisiae glycerol uptake/transporter 1, acts as a negative regulator for N-terminal palmitoylation of Sonic hedgehog. *FEBS J* 275:318-331.

101. Awatramani, R., Soriano, P., Mai, J.J., and Dymecki, S. 2001. An Flp indicator mouse expressing alkaline phosphatase from the ROSA26 locus. *Nat Genet* 29:257-259.

102. Agah, R., Frenkel, P.A., French, B.A., Michael, L.H., Overbeek, P.A., and Schneider, M.D. 1997. Gene recombination in postmitotic cells. Targeted expression of Cre recombinase provokes cardiac-restricted, site-specific rearrangement in adult ventricular muscle in vivo. *J Clin Invest* 100:169-179.

103. Li, S., Czubryt, M.P., McAnally, J., Bassel-Duby, R., Richardson, J.A., Wiebel, F.F., Nordheim, A., and Olson, E.N. 2005. Requirement for serum response factor for skeletal muscle growth and maturation revealed by tissue-specific gene deletion in mice. *Proc Natl Acad Sci U S A* 102:1082-1087.

104. Zhu, Y., Romero, M.I., Ghosh, P., Ye, Z., Charnay, P., Rushing, E.J., Marth, J.D., and Parada, L.F. 2001. Ablation of NF1 function in neurons induces abnormal development of cerebral cortex and reactive gliosis in the brain. *Genes Dev* 15:859-876.

105. Yang, X., Arber, S., William, C., Li, L., Tanabe, Y., Jessell, T.M., Birchmeier, C., and Burden, S.J. 2001. Patterning of muscle acetylcholine receptor gene expression in the absence of motor innervation. *Neuron* 30:399-410.